Computational Study and Design of Self-Assembling Block Polymers

A DISSERTATION
SUBMITTED TO THE FACULTY OF THE GRADUATE SCHOOL
OF THE UNIVERSITY OF MINNESOTA
BY

Logan J. Case

IN PARTIAL FULFILLMENT OF THE REQUIREMENTS
FOR THE DEGREE OF
DOCTOR OF PHILOSOPHY

Advisors: Kevin D. Dorfman & Frank S. Bates

January, 2023

Acknowledgements

First, I would like to thank my advisors, Prof. Kevin D. Dorfman and Prof. Frank S. Bates, for their invaluable support and guidance throughout my graduate school career. Their passion and enthusiasm for research is truly infectious; I left most meetings with a renewed excitement about my research efforts. I thank them also for their admirable commitment to help me grow both as a professional and as a scholar.

I am grateful to have had the opportunity to work and learn alongside fantastic colleagues in the Dorfman and Bates groups. Special thanks to my colleagues Dr. GK Cheong, Dr. Sojung Park, Dr. Aaron Lindsay, Dr. Andreas Mueller, Dr. Anshul Chawla, Ryan Collanton, Ben Magruder, Zach Gdowski, and Pengyu Chen for numerous engaging and enlightening polymer-related conversations. To my fellow basement-office dwellers in the Dorfman group: thank you for making our windowless working hours that much more enjoyable. To the remaining Dorfman group members and Bates group members: thank you for helping to make my time at the University of Minnesota such a wonderful experience. That I am unable, for brevity's sake, to provide an exhaustive list of colleagues who have positively impacted my graduate school experience truly speaks to the quality of the group environments.

I am thankful as well for the amazing friendships forged with my classmates in the crucible of first-year grad classes. Patrick, AJ, Justin, Matt, Christian, Nathan, Isaac, Kathleen, Ben, Paul, Joe, Erin, and Teli: Thank you all for being the amazing people and friends that you are.

My gratitude extends, as well, to those outside Amundson Hall. First and foremost, I thank my parents. Your tireless love and support made me who I am today and built the foundation that made all of this possible. You have, at every turn, encouraged me to pursue my passions and done your best to ensure that I had the resources and

opportunity to do so. I could not have done any of this without you. Next, I want to thank my brothers and the rest of my family for their constant love and support. Finally, I want to thank Sam for her companionship and unwavering support over these pandemic-disrupted years.

I would like to thank the National Science Foundation (NSF DMR-1725272 and NSF DMR-1719692) for finanically supporting this work. I also thank the Minnesota Supercomputing Institute for providing the computational resources that made this work possible.

Dedication

To the Case family

Abstract

Upon cooling below the order-disorder transition temperature, block polymers self-assemble into a wide variety of nanostructured morphologies. When paired with advances in synthetic chemistry that allow unprecedented control over the size and architecture of these block polymers, these self-assembly characteristics make block polymers excellent candidates for use in specialty materials with highly tunable properties. Potential applications of block polymers range from filtration membranes to photonic crystals. As it happens, however, the source of this exemplary potential is also one of the great barriers to its realization. The vast design spaces available for block polymers (through numbers and permutations of chemistries, and architectural features) make possible a potentially limitless variety of morphologies. At the same time, these design spaces combined with the subtlety of mechanisms driving morphology selection make finding systems which adopt those morphologies a daunting task.

In this dissertation, we take a computational approach to address the challenge of designing block polymer specialty materials through two broad approaches. First, we directly address the challenges posed by these vast design spaces by developing an open-source software to automate the exploration of polymer parameter space. This software uses a particle swarm optimization algorithm to guide a search through polymer parameter space for positions where self-consistent field theory predicts a targeted morphology will be most stable compared to a set of competing phases. Second, we use computational studies of two classes of diblock blends seeking to understand the mechanisms that stabilize the low-symmetry Frank-Kasper phases in block polymers with the goal of improving the intuition that guides future efforts to design block polymer materials. In the first of these studies, we use an AB/B′C diblock "alloy" with miscible corona and immiscible core blocks to probe the effect of conformational asymmetry on the stability of Frank-Kasper Laves phases when the conformational asymmetry is confined to only particular particle positions. This study finds that conformational asymmetry can be either stabilizing or destabilizing for the Laves phases, depending on which particles are impacted. In the second of these studies, we attempt to identify the balance of core and corona bidispersity in AB/A′B′ blends which can still enable formation of Frank-Kasper

phases. Unfortunately, this latter study was complicated by a series of methodological flaws limiting its utility in the furtherance of block polymer design. Regardless, the flawed study serves as a lesson in proper study design, and the importance of carefully considering complicating factors.

Contents

List of Tables

List of Figures

Chapter 1

Introduction

1.1 Block Polymers

Polymeric materials are ubiquitous in the world today with polymer-based materials found in virtually every facet of life. When the typical person thinks about the structure of polymers (if they do at all) they likely envision the homopolymer: a long chain consisting of identical monomeric links. Few people are likely to think about the wide array of different monomer chemistries that can be used in these structures; even fewer are likely to think of the variation possible when two or more monomer chemistries are combined in the same copolymer. In this dissertation, we focus on just one type of copolymer: the block polymer.

Block polymers consist of two or more homopolymer chains which are covalently bonded at their ends to form a single molecule. Interest in this class of polymer has grown considerably in recent decades as a result of their ability to spontaneously assemble into a wide range of ordered morphologies at low, but practically relevant, temperatures. This spontaneous ordering is ultimately driven by the thermodynamic drive for chemically dissimilar molecules to avoid contact with each other. At sufficiently low temperature, this contact-avoidance causes a blend of two or more homopolymers to separate into distinct macroscopic domains, much as oil and vinegar will separate in a salad dressing; this process is known as macrophase separation. In block polymers, the presence of covalent bonds between the blocks prevents this macrophase separation.

Instead, when cooled below the order-disorder transition temperature T_{ODT}, the polymer blocks segregate into microdomains on molecular length scales, a process called microphase separation. Arrangement of these polymers into these microdomains while uniformly filling space forces the polymers out of their normal random-coil configuration and into either stretched or compressed configurations, incurring an entropic penalty. The particular morphology adopted by the polymer is then determined by a delicate balance of this entropic stretching penalty against the enthalpic cost of contact between dissimilar chemistries.

The thermodynamic balancing act involved in this self-assembly process means that different polymers will adopt different self-assembled morphologies, as variations in polymer chemistry or structure impact the thermodynamic balance. Even the simplest block polymer, the AB diblock copolymer, can adopt at least eight distinct ordered morphologies as equilibrium structures, with other metastable morphologies accessible through processing techniques. Looking beyond diblock copolymers reveals an ever expanding realm of polymer structures (Fig. 1.1) and possible self-assembled morphologies.[1] As advances in polymer synthesis techniques have enabled more precise control of increasingly complex block polymer architectures, there exists a potential to use block polymers as tunable designer materials,[1–3] with applications ranging from semiconductors[4–6] to photonic crystals[7,8] to filtration materials.[9–11] One of the largest barriers to reaching this potential is the sheer size of design spaces available in block copolymers.[1] To this end, a synergistic approach combining experimental and computational efforts will be required because, although experimental work will remain the ultimate arbiter of how block polymers *actually* behave, computation has the potential to accelerate the discovery process by (1) offering predictive guidance in the quest for block polymer designer materials, and (2) improving design intuitions by more deeply probing the mechanisms driving observed block polymer behaviors.

In many cases, computational studies can be performed more rapidly than an analogous experimental study. When large design spaces are involved, as is often the case for block polymers, a promising dynamic would start with computational studies searching large regions of parameter space for a desired morphology. Those computational predictions would then guide experimental studies focused on narrower regions of the parameter space. Whether the prediction is verified or refuted at this point, there is

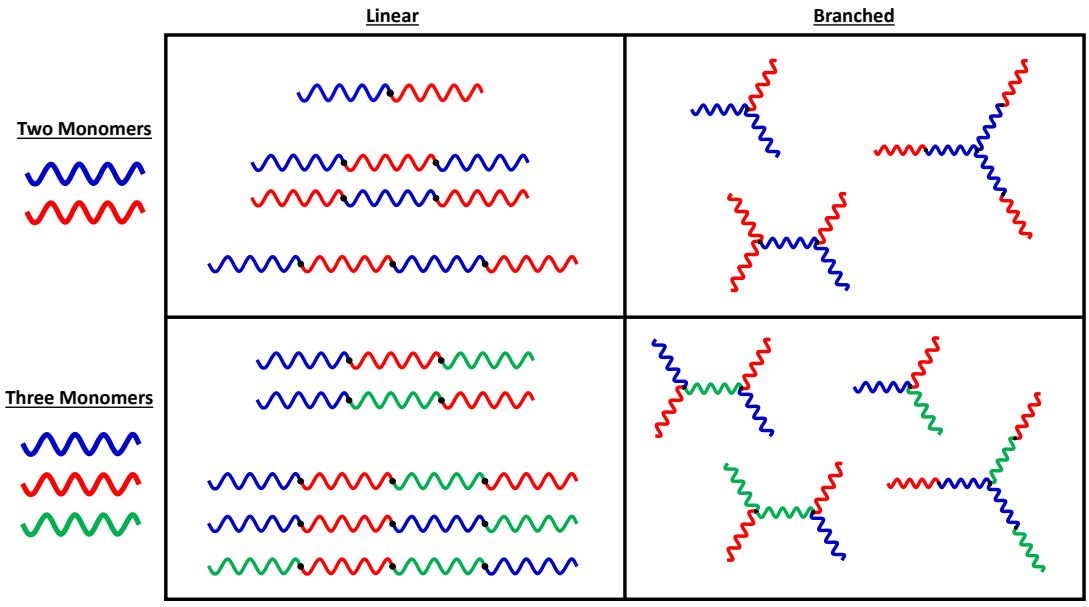

Figure 1.1: A small sample of possible block polymer structural varieties using only two or three chemistries (red, blue, or green) using either linear or branched architectures.

opportunity to gain more insight into the mechanisms of block polymer self-assembly and potentially improve future searches. This dynamic serves as the motivating factor behind the work presented in Chapter 4, in which we develop an inverse design software to automate the search of large polymer design spaces.

In addition to being faster (in many cases) than experimental studies, computational work also has the benefit of probing self-assembly mechanisms much more deeply through idealized parameter control and the ability to track more minute details. Experimental work is constrained to physically realizable polymer systems; changing the monomer used for the synthesis changes every characteristic of that block. Computation, meanwhile, allows researchers to change all properties of a block independently. Thus, a computational study can fully isolate the effects of individual properties to probe their impact on self-assembly. In this dissertation, Chapter 5 describes such a study in which we manipulate conformational asymmetries in a diblock polymer blend analogous to metal alloys.

Up to this point, we have largely been describing block polymers and their microphase separation behaviors in the abstract. More concretely, we focus throughout

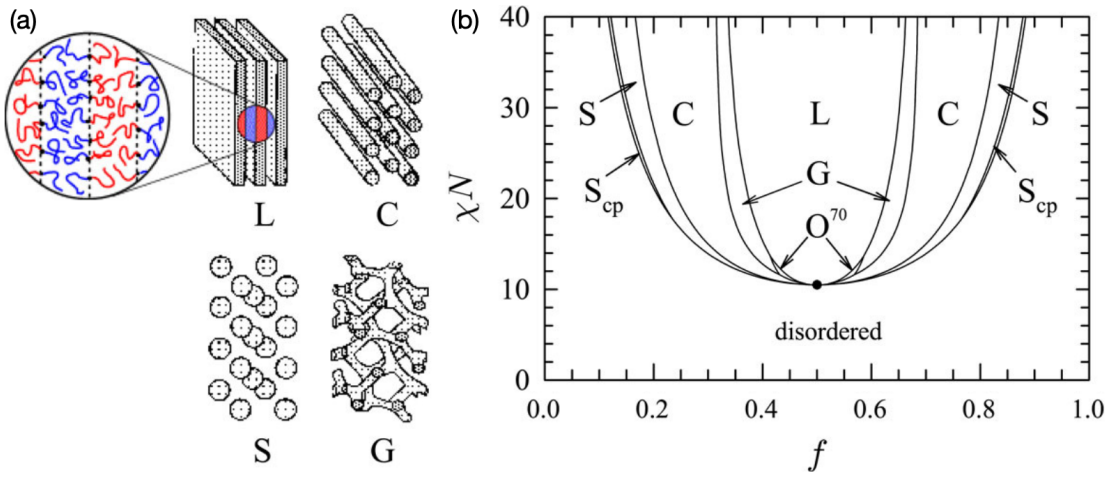

Figure 1.2: (a) A depiction of the lamellar (L), hex (C), bcc (S), and double gyroid (G) morphologies that can be found in a neat diblock copolymer, and (b) the classical diblock copolymer phase diagram showing regions of fcc (S_{cp}), bcc (S), hex (C), gyroid (G), O^{70}, and lamellae (L). The inset in (a) depicts a schematic of the hypothetical arrangement of diblock copolymers in the lamellar structure, with their junctions on the lamellar interface. Figure reproduced from Ref. 12 with permission.

this thesis on systems of diblock copolymers because, despite their simplicity compared to other block polymers, they remain a fruitful research subject for studying self-assembly. The classical phase behavior of the neat diblock copolymer is governed by two parameters. The first is block fraction, f_A, which describes the chain composition as a volume fraction of the A block in the chain. The second is segregation strength, χN where $\chi \propto T^{-1}$ is the temperature-dependent Flory-Huggins interaction parameter and N is the total chain degree of polymerization. When the first theoretical phase diagrams for diblock copolymers were published in the mid-1990s, these parameters lie on their axes.[13,14] On these early phase diagrams, one could identify five ordered morphologies: face-centered cubic spheres (fcc),[14–17] body-centered cubic spheres (bcc),[18–20] hexagonally packed cylinders (hex),[18] double gyroid network (gyr),[13,21] and alternating lamellae (lam).[18] Over a decade later, this classical phase diagram was ammended with the discovery of the O^{70} network phase[22,23] stability window in the low-χN portion of what was previously the gyroid region. The classical diblock copolymer phase diagram, along with illustrations of some of the phases represented on it, can be found in Fig. 1.2.

Around the same time as the early phase diagrams, researchers started noticing the

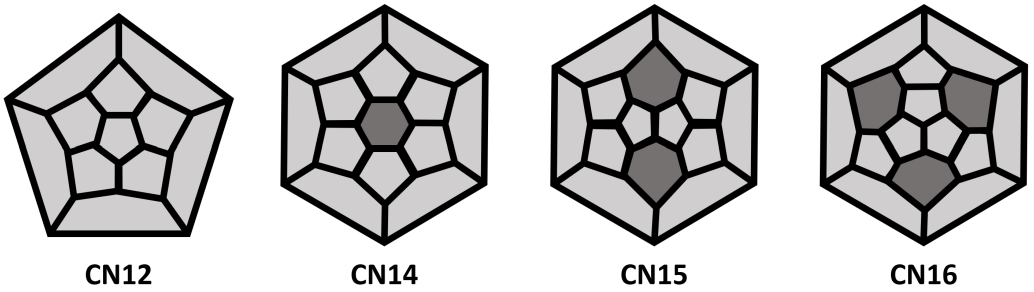

Figure 1.3: Planar graphs of the CN12, CN14, CN15, CN16 Frank-Kasper polyhedra. Each polyhedron is identified by its coordination number (CN).

importance of a third parameter for the neat diblock copolymer. This parameter is conformational asymmetry, $\epsilon = b_A/b_B$, which measures the ratio of the two monomers' statistical segment lengths, b_A and b_B.[24–27] A detailed discussion of conformational asymmetry can be found in Chapter 5. For now, we note only that the consideration of conformational asymmetry has introduced two complex sphere packings, the Frank-Kasper σ[28–30] and A15[30–32] phases, to the neat diblock phase diagrams.

There has been particular interest recently in understanding the emergence of these Frank-Kasper phases in block polymers. Originally defined more than 60 years ago, the Frank-Kasper phases are a class of low-symmetry particle packings first reported in metal alloys.[34,35] The structures consist of tetrahedrally close-packed particle sites with coordination shells of 12, 14, 15, or 16 neighboring particles, resulting in polyhedral Wigner-Seitz cells* with 12 pentagonal faces and either 0, 2, 3, or 4 hexagonal faces, respectively, as illustrated in Fig. 1.3. In comparison to fcc and bcc, Frank-Kasper phases are highly complex, with all such structures containing at least two symmetry-inequivalent particle positions and at least seven particles per unit cell. Discovery of the Frank-Kasper σ phase in diblock copolymers and tetrablock terpolymers in 2010[28] upended the assumption that high-symmetry phases such as fcc or bcc would always dominate the sphere-forming regions of block copolymer space. Since this ground-breaking discovery, four different Frank-Kasper phases have been identified as stable morphologies in block copolymer systems: σ[28–30,37–44] and A15,[30,45] as well as the C14 and C15 Laves phases[42,43,46–48] The mechanisms behind the stabilization of these

*The Wigner-Seitz cell, or Voronoi cell, for a lattice site (particle position) is the region of space closer to that lattice site than to any other lattice site.[36]

Frank-Kasper phases in block copolymers remains a working hypothesis[49,50] and we thus focus throughout this thesis on the emergence of Frank-Kasper phases in block copolymer systems.

1.2 Research Outline

In Chapter 2 we introduce the theoretical and computational framework of the modern polymer self-consistent field theory (SCFT). This theory, and its computational application, forms the foundation of the remaining work in this thesis. Having established an understanding of the underlying polymer theory, Chapters 3 and 4 detail the development of software tools relevant to the study of block polymer self-assembly. In particular, Chapter 3 discusses a software tool to automate the generation of initial guess fields for SCFT calculations, with methods for three distinct classes of self-assembled morphology. Chapter 4 details the development and testing of an open-source software for the design and discovery of block copolymers which uses particle swarm optimization (PSO) linked to SCFT calculations to drive a search for polymer parameters that can stabilize the formation of a targeted morphology. The remainder of the thesis focuses on the application of SCFT to study the behavior of two classes of binary block polymer blends. In Chapter 5, we use a binary diblock copolymer alloy of type AB/B′C to more deeply probe the role of conformational asymmetry in the formation of Frank-Kasper phases. Next, Chapter 6 discusses the lessons learned from a methodologically flawed investigation into the impacts of core-block and corona-block bidispersity on the emergence of Frank-Kasper phases in AB/A′B′ blends. Finally, Chapter 7 concludes the thesis with remaining questions and suggestions of avenues for future research in light of the efforts in Chapters 3–6.

Chapter 2

Self-Consistent Field Theory

2.1 Introduction

Computational study of polymer systems is typically done through one of two approaches: particle-based models or field-based models. Particle-based models treat a single polymer as a string of beads or particles and model the behavior of a polymer system using the pair-wise interaction potentials among beads from many chains. Simulations in the particle-based models will then be updated and sampled with Monte Carlo[51,52] or molecular dynamics[53] methods to collect a statistically descriptive sample of the system. In condensed-phase systems such as a polymer melts, such simulations demand substantial numbers of particles and proportionally large computational resources. Field-based models use a Hubbard-Stratonovich transformation to convert the many-body interactions of the particle models into interactions of independent polymer chains with chemical potential fields.[54,55] Such a transformation reduces the computational cost of the method without invocation of any approximations.[55]

In the full field theory produced through the Hubbard-Stratonovich transformation, it is still necessary to sample the fluctuating field with, for example, Langevin dynamics methodologies.[54,56] From here, approximations can be used to further reduce the computational cost of the method. Particularly useful is the saddle-point or mean-field approximation in which one field (the "mean field") is assumed to dominate the statistics of the system to such an extent that field fluctuations can be neglected.[55] This approximation leads to the self-consistent mean-field theory (SCFT) for polymers,

which is one of the most popular methodologies today for the computational study of block copolymer self-assembly.

Self-consistent field theory is the foundation of work presented in this dissertation, so we commit this chapter to discussion of the theory and its application. We start by describing the SCFT equations both in the canonical (N,V,T) and grand canonical (μ, V, T) ensembles. In this discussion, we omit the derivation of the SCFT equations which has been well-discussed elsewhere[55,57,58] and instead focus on the equations and their interpretations. We then briefly introduce the open-source Polymer Self-Consistent Field software packages which implement SCFT calculations and which are used throughout this work.

2.2 Self-Consistent Field Theory

For this discussion of SCFT, we focus initially on the formulation of SCFT in the canonical ensemble. Section 2.2.2 discusses differences that arise when formulating SCFT in the grand canonical ensemble. We consider an incompressible melt of linear block polymers modeled as continuous Gaussian chains. The polymers are composed of M unique monomer chemistries indexed using $\alpha, \beta \in \{1, 2, \ldots, M\}$. Each monomer has a unique statistical segment length b_α and is coarse-grained such that it occupies the common monomer reference volume v.* The Flory-Huggins parameter $\chi_{\alpha\beta}$ quantifies the interaction strength between two monomers α and $\beta \neq \alpha$ while self-interaction of a monomer α with itself is thermodynamically neutral such that $\chi_{\alpha\alpha} = 0$. The system is taken to be a blend of C block polymer species indexed using $k \in \{1, 2, \ldots, C\}$. Each polymer species consists of B_k blocks $j \in \{1, 2, \ldots, B_k\}$ with block degrees of polymerization $N_j^{(k)}$ such that species k has total chain degree of polymerization N_k given by

$$N_k = \sum_{j=1}^{B_k} N_j^{(k)}$$

*In this SCFT formalism, a "monomer" is primarily a bookkeeping device and need not conform to the formal definition of a monomer as a single chemical repeat unit. Instead, a "monomer" represents the molar mass of polymer chain occupying one monomer reference volume, v.[59] For more information about mapping these SCFT parameters to parameters of real polymers, see Sinturel et al.[60]

Traditionally, in the canonical ensemble, the number of particles or molecules of each species would be held constant; in the current discussion, we leverage the equivalence (imposed by incompressibility) between volume fraction and number of particles to specify system compositions in terms of volume fractions. The overall volume fraction of polymer k in the blend is given by ϕ_k subject to the requirement that

$$\sum_{k=1}^{C} \phi_k = 1$$

because the system contains only polymer species. This requirement also means that a system of C polymer species will only have $C-1$ independent ϕ_k values. The coarse-graining of monomers to occupy the same reference volume v yields an equivalence between volume and degree of polymerization allowing us to express the volume fraction of block j within polymer k in terms of block and chain degrees of polymerization as $f_j^{(k)} = N_j^{(k)}/N_k$. Calculations throughout this dissertation leverage unit-cell SCFT calculations, in which the SCFT equations are solved for a single unit cell with volume V and containing $n = V/v$ monomers. Fields within this unit cell are constrained to the space-group symmetry consistent with the morphology being studied and subject to periodic boundary conditions which allow the single unit cell to represent a macroscopic volume.

2.2.1 The Canonical SCFT Equations

The potential field acting on monomer α at spatial position $\boldsymbol{r}$ is denoted by $\omega_\alpha(\boldsymbol{r})$. It can be calculated with

$$\omega_\alpha(\boldsymbol{r}) = \sum_{\beta=1}^{M} \rho_\alpha(\boldsymbol{r})\rho_\beta(\boldsymbol{r})\chi_{\alpha\beta} + \xi(\boldsymbol{r}) \tag{2.1}$$

where $\rho_\alpha(\boldsymbol{r})$ is the average local volume fraction of monomer α at position $\boldsymbol{r}$ and $\xi(\boldsymbol{r})$ is a Lagrange multiplier enforcing the incompressibility constraint,

$$\sum_{\alpha=1}^{M} \rho_\alpha(\boldsymbol{r}) = 1 \tag{2.2}$$

Before starting an SCFT calculation, a software user must generate or identify an initial guess for each $\omega_\alpha(\boldsymbol{r})$ for the morphology of interest. Methods for generating these guesses, and a software tool for this purpose, are discussed in Chapter 3. The requisite statistical properties for each chain k can then be obtained from these fields by solving the initial value problems for the modified diffusion equations (MDEs)

$$\frac{\partial q_k(\boldsymbol{r}, N_k)}{\partial s} = \left[\frac{b_{\alpha(s)}^2}{6}\nabla^2 - \omega_{\alpha(s)}(\boldsymbol{r})\right] q_k(\boldsymbol{r}, s), \qquad q_k(\boldsymbol{r}, 0) = 1 \tag{2.3}$$

$$-\frac{\partial q_k^\dagger(\boldsymbol{r}, s)}{\partial s} = \left[\frac{b_{\alpha(s)}^2}{6}\nabla^2 - \omega_{\alpha(s)}(\boldsymbol{r})\right] q_k^\dagger(\boldsymbol{r}, s), \qquad q_k^\dagger(\boldsymbol{r}, N_k) = 1 \tag{2.4}$$

where $q_k(\boldsymbol{r}, N_k)$ and $q_k^\dagger(\boldsymbol{r}, N_k)$ are known as "propagator" functions, and where the contour coordinate $s \in [0, N_k]$ describes positions along the chain's length. In these MDEs, the subscript $\alpha(s)$ on $b_{\alpha(s)}$ and $\omega_{\alpha(s)}$ indicates that the statistical segment length and chemical potential field will be those corresponding to the monomer type at contour position s. Conceptually, these propagator functions represent the normalized partition functions of complementary chain segments under confinement of the chain segment s to position $\boldsymbol{r}$. In particular for chain k with segment s confined to position $\boldsymbol{r}$, the forward propagator $q_k(\boldsymbol{r}, N_k)$ is a normalized partition function for all chain segments on $[0, s]$ while the backward propagator $q_k^\dagger(\boldsymbol{r}, N_k)$ is the complementary partition function for the remaining chain segments on $[s, N_k]$.

Once solved, the propagator functions are used to compute all relevant statistical information about the polymers. At the appropriate extremum of the contour variable s, the propagator functions describe the statistical weight of the entire polymer chain when its end is found at position $\boldsymbol{r}$ as $q_k(\boldsymbol{r}, N_k)$ or $q_k^\dagger(\boldsymbol{r}, 0)$. Either of these functions can be used to compute the normalized partition function for the unconstrained chain with

$$Q_k = \frac{1}{V}\int_V d\boldsymbol{r}\, q_k(\boldsymbol{r}, N_k) = \frac{1}{V}\int_V d\boldsymbol{r}\, q_k^\dagger(\boldsymbol{r}, 0) \tag{2.5}$$

where the integral serves to remove the positional constraint on the chain end by summing the statistical weight of all possible chain-end positions within the unit cell. Further, the product of the propagator functions at the same contour position, $q_k(\boldsymbol{r}, s)q_k^\dagger(\boldsymbol{r}, s)$, gives the statistical weight of the entire chain when segment s is confined to position

$\boldsymbol{r}$. This statistical weight is proportional to the probability of finding the chain contour segment s at position $\boldsymbol{r}$ and that probability can, in turn, be used to compute the average local volume fractions for each monomer, $\rho_\alpha(\boldsymbol{r})$. In the canonical ensemble, $\rho_\alpha(\boldsymbol{r})$ is given by[58]

$$\rho_\beta(\boldsymbol{r}) = \sum_{k=1}^{C} \left[\frac{\phi_k}{Q_k N_k} \int_{\alpha(s)=\beta} ds\, q_k(\boldsymbol{r}, s) q_k^\dagger(\boldsymbol{r}, s) \right] \tag{2.6}$$

where the summation adds the contributions from all chains, and where the integral is taken over all contour segments containing monomer β.

Recognizing that the local monomer volume fractions calculated from the partition functions with Eq. 2.6 also appear in Eq. 2.1, which defines the monomer potential fields, and that these potential fields are themselves used to compute the partition functions, we see a coupled dependence among Eqs. 2.1–2.6. These equations form the complete set of SCFT equations. From the initial potential fields, these equations must be solved by an interative process until the fields become self-consistent; that is, until the potential fields computed using Eq. 2.1 are in sufficient agreement with the fields used to solve the MDEs of Eqs. 2.3 and 2.4. After the SCFT iterator converges, the non-dimensionalized Helmholtz free energy per monomer is given by[61]

$$\begin{aligned} \frac{F}{nk_BT} = \frac{1}{V} \sum_{\alpha=1}^{M} \sum_{\substack{\beta=1 \\ \beta\neq\alpha}}^{M} \chi_{\alpha\beta} \int d\boldsymbol{r} \rho_\alpha(\boldsymbol{r}) \rho_\beta(\boldsymbol{r}) - \frac{1}{V} \sum_{\alpha=1}^{M} \int d\boldsymbol{r} \omega_\alpha(\boldsymbol{r}) \rho_\alpha(\boldsymbol{r}) \\ + \sum_{k=1}^{C} \frac{\phi_k}{N_k} \left(\ln \frac{\phi_k}{Q_k} - 1 \right) \end{aligned} \tag{2.7}$$

where k_B is the Boltzmann constant and T is the absolute temperature.

2.2.2 Grand Canonical Ensemble

Instead of system composition, calculations in the grand canonical ensemble specify the chemical potential μ_k for each polymer k. These chemical potentials are related to the overall volume fractions by[58]

$$\exp\left(\frac{\mu_k}{k_BT} \right) Q_k = \phi_k \tag{2.8}$$

The incompressibility constraint combined with Eq. 2.8 means that a system of C polymer species will only have $C-1$ independent chemical potential values. Substitution of Eq. 2.8 into Eq. 2.6 gives the grand canonical formulation for the local monomer volume fractions as

$$\rho_\beta(\boldsymbol{r}) = \sum_{k=1}^{C} \left[\frac{1}{N_k} \exp\left(\frac{\mu_k}{k_B T}\right) \int_{\alpha(s)=\beta} ds\, q_k(\boldsymbol{r}, s) q_k^\dagger(\boldsymbol{r}, s) \right] \tag{2.9}$$

where the summation again combines the contribution of each polymer species, and the integral is again taken over all contour segments containing monomer β.

In the grand canonical ensemble, the free energy is given by[62]

$$F_g = -PV \tag{2.10}$$

where P is the system pressure. This grand canonical free energy is related to the Helmholtz free energy by[58]

$$F_g = F - \sum_{k=1}^{C} n_k \mu_k \tag{2.11}$$

where the sum is taken over all polymer species. Equations 2.10 and 2.11 to give

$$PV = -F + \sum_{k=1}^{C} n_k \mu_k \tag{2.12}$$

If we make the substitution $n_k = n\phi_k / N_k$ to get

$$PV = -F + \sum_{k=1}^{C} \frac{n \phi_k \mu_k}{N_k}$$

and non-dimensionalize by dividing through with nk_BT, we obtain

$$\frac{Pv}{k_B T} = -\frac{F}{nk_B T} + \sum_{k=1}^{C} \frac{\phi_k}{N_k} \left(\frac{\mu_k}{k_B T}\right) \tag{2.13}$$

which shows how all dimensionless quantities reported by PSCF are related for calculations in the grand canonical ensemble.[59]

2.3 Software

The works presented in this dissertation make use of two different versions of the Polymer Self-Consistent Field (PSCF) software to perform SCFT calculations. The two versions vary in programming language, hardware flexibility, available iterators, file structures, and acceptable polymer structures. These differences do not impact the interpretation or understanding of results presented in this thesis, but are briefly described here for (1) the reader's awareness of the differences and (2) for their relevance to some discussions in Chapter 4.

2.3.1 Fortran Version

The older version of the software, referred to throughout this work as PSCF, was developed in the Fortran 90 programming language.[59,61] It is written for serial execution on a single CPU core. Two iterators are available in this version: A pseudo-Newton-Raphson iterator with backtracking line search,[61] and an Anderson Mixing iterator.[63–66] Both iterators also include simultaneous optimization of unit-cell dimensions[66,67] for accurate free energy evaluation. This version is restricted to blends of linear block polymers, homopolymers, and solvents. This software version is used for Chapters 4 and 6.

2.3.2 C++/Cuda Version

A newer version of the software has been developed using C++,[68,69] and is referred to throughout this work as PSCFpp (for PSCF++, referencing the programming language). This version can be run on a single CPU, but also includes the ability to execute on a graphics processing unit (GPU) by including code written in Cuda. Execution on a GPU offers substantial performance benefits through high degrees of parallelization.[68,70] Presently, the only iterator available in this version is the Anderson Mixing iterator[63–66] with optional simultaneous unit-cell optimization.[66,67] This code is also generalized beyond linear polymers to enable study of arbitrarily branched acyclic block polymer structures. This version was used for calculations in Chapter 5.

Chapter 3

SCFT Initial Guess Generation[†]

3.1 Introduction

As stated in Chapter 2, every SCFT calculation requires an initial guess for the potential fields, $\omega_\alpha(\boldsymbol{r})$. Selection of a reasonable initial guess is critical to the successful application of SCFT. In some cases, a poorly chosen initial guess will result in failed convergence. In other cases, the algorithm will converge from a poor initial guess to a defective structure and thus return an inaccurate energy for the phase of interest. The best option for an initial guess would be the field returned by a previously converged SCFT calculation of the same phase at a nearby point in phase space. Such an approach would be analogous to a single step in a zeroth-order continuation. It is often the case, however, that calculations have not been done in a region of phase space sufficiently close to the current point of interest. Over modest distances in phase space, it can be reasonably efficient to span the distance from a previously converged solution to a new state point with a series of SCFT calculations in conjunction with a higher-order (first-order or higher) continuation method. This approach can be achieved using the `sweep` functionality available in the PSCF software.

In many cases, however, neither of these approaches are possible. Sometimes the state point of interest lies far in phase space from any prior work, such that the cost of

[†]Parts of this chapter are adapted from Logan J. Case, Kris T. Delaney, Glenn H. Fredrickson, Frank S. Bates, and Kevin D. Dorfman *The European Physical Journal E* **2021**, *44*(9), 115. (Ref. 71)

a sweep becomes prohibitive. Other times, sweeps will encounter regions in which convergence of the phase is difficult, thus blocking attempts to sweep from prior solutions. In still other cases, the research may consider a novel phase for which no converged solutions are available anywhere in state space. In these cases, having some method to generate initial guess fields becomes necessary.

Along with the launch of the Fortran-implemented version of PSCF, Arora et al. reviewed two methods for initial guess generation.[61] The first of these, the "form-factor" method, works for particle-packing phases with disconnected microdomains of one monomer component. The second, the "level-set" method, is better suited for network phases, such as the double-gyroid. Both methods were proposed and the success of each method was demonstrated, but each was demonstrated through the use of case-by-case Matlab scripts. This chapter describes a software tool, called `pscfFieldGen`, implementing a generalized form of these methods for PSCF, in addition to adding a basic methodology for generation of initial guesses for lamellar structures.

For the convenience of users, `pscfFieldGen` accepts a PSCF parameter file as part of its input and tries to use that parameter file to supply as much system-specific information as possible. In theory, this allows the user to set up their calculation via parameter file, generate their guess with the software based on this parameter file, and run their calculation using the same parameter file. In practice, this procedure only strictly holds true for particle and lamellar structures; the network level-set method requires some intermediate processing steps via the PSCF software for which the user must generate a specialized parameter file, as will be discussed in Section 3.3.

For all morphologies, the software first uses the polymer structures and blend fractions specified in the parameter file to compute the overall volume fraction of each monomer β according to

$$\phi_\beta = \sum_{k=1}^{C} \phi_k \sum_{\substack{j=1 \\ \alpha(j)=\beta}}^{B_k} \frac{N_j^{(k)}}{N_k} \tag{3.1}$$

where the notation $\alpha(j) = \beta$ indicates that the inner sum should be taken only over blocks j in polymer k which are composed of monomer type β. For a simple system such as a neat diblock polymer melt, this overall volume fraction would be equivalent to the block fraction of each block. In more complex systems, such as multi-block

polymers or blends, in which the same chemistry may appear in multiple places, ϕ_β represents the combined contribution of each block containing monomer chemistry β. These overall monomer volume fractions are used both to size the defining structure of the desired morphology and to ensure that the local volume fractions in the initial guess are consistent with the overall composition when the average is taken over the full unit cell.

Regardless of whether lamellae, networks, or particles are considered, the defining structure is sized based on a reference monomer α. This reference monomer is taken to be the monomer species in the core of the structure—i.e. that in the core of particles, or inside the struts and joints of a network. By default, this monomer is chosen to be that with the lowest overall volume fraction, $\min_\alpha \phi_\alpha$. This default selection gives the program some capacity to accommodate structural inversions that can occur with large fluctuations in chain composition; this is a particularly useful feature when, as described in Chapter 4, the guess generator is coupled with an automated search of the phase space. This approximation is only strictly accurate in the simple case of a neat melt of conformationally symmetric diblock copolymer, but should be reasonable in a variety of systems. The user also has the ability to override the default core selection (except for lamellae; see Section 3.4) by specifying a set of one or more monomers to consider in the core selection. If only one monomer is given in this set, that monomer will be used as the core of the structure. If two or more monomers are given, the core will be chosen as the monomer in the set with the lowest ϕ_α.

3.2 Particle Phases

This section describes the form-factor initialization method.[61,72] This method is best applied to morphologies consisting of discrete, disconnected domains of core monomer(s) arranged within a matrix (structured or unstructured) of non-core monomers. Most commonly, this category of structures consists of three-dimensional packings of spherical micelles or two-dimensional packings of cylinders.

3.2.1 Form-Factor Method

This generation method starts with a recognition that the real-space local volume fraction profile of monomer α can be represented as the Fourier series

$$\rho_\alpha(\boldsymbol{r}) = \sum_{\boldsymbol{q}} \rho_\alpha(\boldsymbol{q}) \exp\left(-i\boldsymbol{q}\cdot\boldsymbol{r}\right) \tag{3.2}$$

where $\rho_\alpha(\boldsymbol{q})$ is the Fourier coefficient for wave-vector $\boldsymbol{q}$, and where the sum is taken over all wave-vectors. In this representation, the zero-frequency coefficient* for each monomer represents the average concentration of the monomer in the system, i.e. $\rho_\alpha(\boldsymbol{0}) = \phi_\alpha$. All other coefficients represent the amplitude of wave-form deviations from this average, and ultimately give the field its structure. For a monomer α located entirely within the core of N_P particles k, these non-zero-frequency Fourier coefficient can be calculated from

$$\rho_\alpha(\boldsymbol{q}) = \frac{1}{V}\sum_{k=1}^{N_P} f_k(\boldsymbol{q}) \exp\left(i\boldsymbol{q}\cdot\boldsymbol{R}_k\right) \tag{3.3}$$

where $\boldsymbol{R}_k$ and $f_k(\boldsymbol{q})$ are the real-space position and form factor amplitude of particle k, respectively, and V is the unit cell volume.

The form-factors currently implemented in `pscfFieldGen` for cylinders and spheres represent homogeneous structures with sharply-defined boundaries. These sharp boundaries equate to micellar interfaces of near-zero width, which would only be expected in the limit of strong segregation. Most systems of interest, however, would be of low to moderate segregation strength. Further, although the iterator should be able to smooth interfaces which are too sharp, the spatial resolution required to resolve these sharp interfaces would greatly increase the computational load for the problem. It is preferable then to initialize the calculations with lower concentration gradients and allow the iterator to sharpen the interface if necessary. As long as the initial field remains representative of the targeted morphology, the smoother interface allows calculations to be run with resolutions no higher than is strictly necessary to resolve the interfaces for the problem of interest. We thus smooth the interfaces of the initial guess by introducing a

*The zero-frequency coefficient is that corresponding to a wave vector with magnitude 0; i.e. $\boldsymbol{q} = [0,0,0]$ for a 3-dimensional lattice.

Gaussian smearing factor

$$f_s(\boldsymbol{q}) = \exp\left(\frac{-\psi^2|\boldsymbol{q}|^2}{2}\right) \tag{3.4}$$

where $|\boldsymbol{q}|$ indicates the magnitude of the wave vector $\boldsymbol{q}$, and ψ is an interfacial width estimated from Helfand-Tagami theory[73] as

$$\psi = 2\sqrt{\frac{b_{\text{avg}}^2}{6\chi_{\text{avg}}}} \tag{3.5}$$

where b_{avg} and χ_{avg} are the geometric means of the statistical segment lengths (b_{avg}) and the interaction parameters between the core and non-core monomers (χ_{avg}). When this smearing factor is applied, Eq. 3.3 becomes

$$\rho_\alpha(\boldsymbol{q}) = \frac{1}{V}\sum_{k=1}^{N_P} f_k(\boldsymbol{q}) \exp\left(i\boldsymbol{q}\cdot\boldsymbol{R}_k\right) f_s(\boldsymbol{q}) \tag{3.6}$$

which gives the full Fourier amplitude of the core monomer concentration profile for each wave vector $\boldsymbol{q}$.

Although Eq. 3.6 specifies the Fourier amplitudes for the core monomer, it does not explicitly define the matrix amplitudes. To satisfy the requirement of incompressibility, the monomer Fourier amplitudes must sum to zero for each wave vector $\boldsymbol{q}$ with non-zero magnitude,* and thus

$$\sum_{\beta\neq\alpha} \rho_\beta(\boldsymbol{q}) = -\rho_\alpha(\boldsymbol{q})$$

must hold. The simplest way to satisfy this constraint is to weight the amplitudes of each non-core monomer β according to its prevalence in the system relative to all other non-core monomers using $\phi_\beta/\left(1-\phi_\alpha\right)$ as a weighting factor. The resulting Fourier amplitudes for the non-core monomers are given by

$$\rho_\beta(\boldsymbol{q}) = -\rho_\alpha(\boldsymbol{q})\frac{\phi_\beta}{1-\phi_\alpha} \tag{3.7}$$

*As stated earlier, the zero-frequency (or homogeneous) wave-vector coefficients defines the spatially-averaged volume fractions for each monomer, so by definition $\sum_\alpha \rho_\alpha(\boldsymbol{0}) = 1$. The non-zero wave-vector coefficients represent the amplitude of wave-form deviations from this average volume fraction for each monomer. To ensure that the volume fractions at any point in space sum to unity, any deviation by a monomer αabove its average demands a net deviation by monomers $\beta \neq \alpha$ *below* their averages. This leads to the requirement that $\sum_\alpha \rho_\alpha(\boldsymbol{q}\neq\boldsymbol{0}) = 0$.

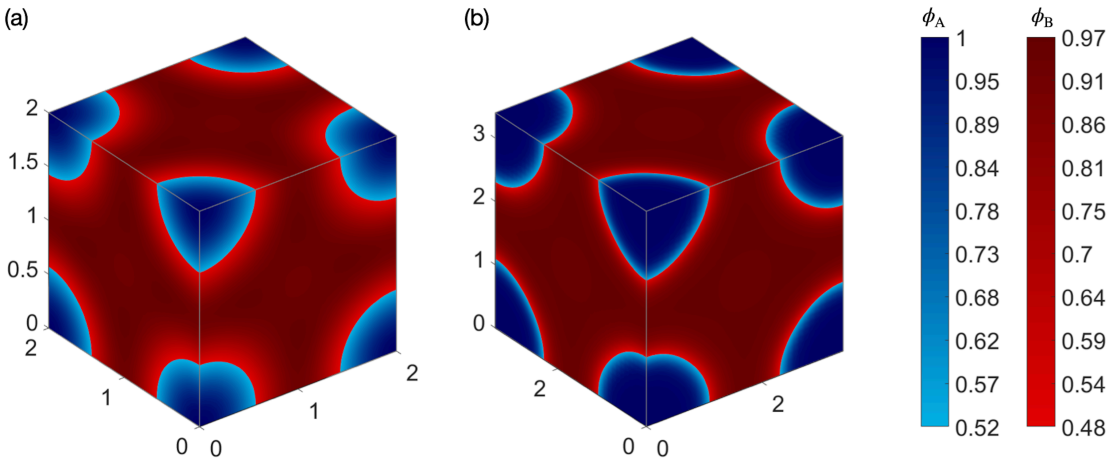

Figure 3.1: The (a) initial field generated by `pscfFieldGen` (after conversion to real-space coordinates via PSCF) and (b) converged field returned by PSCF for the bcc sphere phase.

which satisfies the incompressibility constraint while generating a well-mixed matrix. In initializing the matrix as well-mixed, we rely on the iterator to introduce any additional structure that might be present. Following generation of the field in reciprocal space through `pscfFieldGen`, procedures available in PSCF may be used to convert the field into either a real-space concentration field (such as the one shown in Fig. 3.1) or, more importantly, to the chemical potential fields required for the SCFT calculations.[59]

3.2.2 Implementation

In order to generate guesses for particle phases, we need to be able to evaluate Eq. 3.6. To do this, we need the following information:

1. Unit cell data.
2. Polymer Data.
3. Core monomer.
4. Particle Data.
    - Particle Positions $\boldsymbol{R}_k$
    - Particle Sizes

- Particle Form Factors $f_k(\boldsymbol{q})$

The unit cell data in item 1 is used to enumerate the reciprocal space vectors $\boldsymbol{q}$ and determine the volume of the unit cell. Polymer data in item 2 is used to determine system composition and estimate interfacial width for the smearing factor. All information from these items 1 and 2 can be taken directly from the parameter file supplied by the user. The core monomer for item 3 can be specified by the user or estimated from the parameter file. The data in item 4 are a bit more subtle. Particle sizes can be estimated from the system composition and unit cell volume by assuming that all of the core monomer is located within the particles, computing the total volume of pure core monomer, and distributing this volume evenly across the set of particles. The particle form factors, currently, are hard-coded as that of spheres for 3D structures and circular disks in 2D structures (representing the cross-section of a cylinder). The particle positions must be supplied by the user in some capacity, and are among the most critical inputs since the position of particles determine the symmetry of the phase.

In `pscfFieldGen`, the user has two options to input the particle positions. The first is that the user can supply the program with a complete list of particle positions within the unit cell. We refer to this option as the "basis" input style, since the user directly supplies the full particle basis. The second option is an added convenience feature for the user which we call the "motif" input style. For a motif input, the user specifies only a minimal set of representative particle positions. From this, `pscfFieldGen` will automatically expand the particle list to the full basis required for the generation of the structure using space group symmetry operations. To achieve this, the software comes with a library specifying the full set of symmetry operations in each space group. If the motif input style is specified, the program will look up the symmetry operations of the space group from the library. It will then apply these symmetry operations to a symbolic position vector* in order to generate a set of symbolic general equivalent positions

*A "symbolic" variable in computation is an object which represents not a numerical value but an algebraic variable (such as `x` or `y`), and on which mathematic operations can be performed as if the calculation were done by hand on an algebraic expression. Thus, executing `x + 1` on a symbolic object `x` will return not a value but the actual expression `x + 1`. Numerical values can later be substituted in place of the symbolic variables to yield numerical results. A "symbolic vector" is simply a vector of such values (such as `[x, y, z]`) on which vector operations can be performed (i.e. applying the inversion symmetry operator to the last example would yield `[-x, -y, -z]`). The symbolic math employed in the particle enumeration procedure uses the `SymPy` Python library.

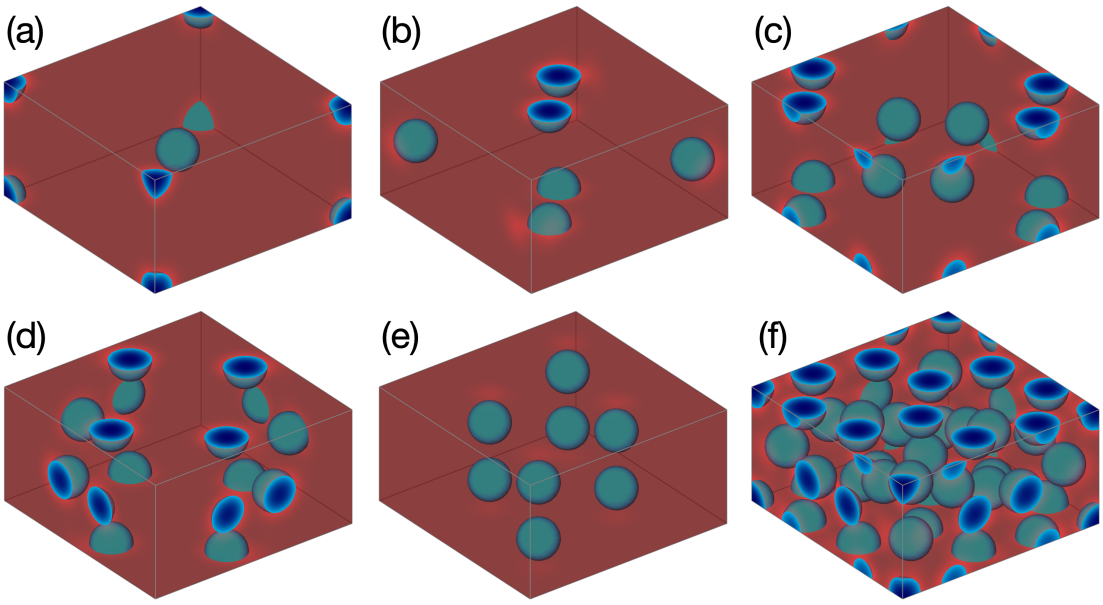

Figure 3.2: Initial field generated by `pscfFieldGen` from an input particle motif containing (a) one particle at Wyckoff Position $2b$ (b) one particle at Wyckoff Position $4f$ (c) one particle at Wyckoff Position $8i$ (d) one particle at Wyckoff Position $8i'$ (e) one particle at Wyckoff Position $8j$ and (f) all five particle positions input to generate the structures in (a)-(e).

(GEPs) consistent with the space group. The coordinates of each motif position are then substituted for their symbolic counterpart in each GEP, and the resulting positions are screened to remove duplicates, or any positions outside the bounds of a single unit cell. In the case of the Frank-Kasper σ phase, which contains 30 particles in its unit cell, the motif input option allows the user to specify only the five symmetry-inequivalent positions in the unit cell, and `pscfFieldGen` will enumerate the remaining 25 positions. This process is illustrated in Fig. 3.2, which shows the particles enumerated for a σ phase guess from each of the five initial positions.

3.3 Network Phases

For network phases such as double gyroid or O^{70}, the software implements the level-set method.[61,74,75] Conceptually, this approach uses a small set of symmetry-adapted basis functions to construct a coarse approximation of the structure. PSCF is used to convert these basis functions into a real-space concentration field. This concentration field is

then used to find a level-surface enclosing a region equal in volume to the total volume of core monomer in the system. The region enclosed by the level surface will be filled with all core monomer, while the matrix is treated as well-mixed.

In practice, this method requires that the user input two parameter files as well as a template field file in symmetry-adapted format. One parameter file should correspond to the intended calculation; the second should contain the system definition, and the `FIELD_TO_RGRID` command used to convert a symmetry-adapted field to real space. This second parameter file is used internally by `pscfFieldGen` to run PSCF as a subprocess and convert the basis functions to a real-space concentration field. The template field file should correspond with the structure of interest. The homogeneous basis function, $\{0, 0, 0\}$, should be included in the file, but the coefficients for this basis function are arbitrary* and can simply be set to zero. The remainder of the file should contain coefficients for only as many basis functions as required to capture the basic geometry of the targeted structure. For a double-gyroid phase, this would require only one basis function, that of the $\{2, 1, 1\}$ star.[61,76] For other network structures, additional basis functions may be required. For each of these inhomogeneous basis functions, the coefficients used for the core monomer will be specified in the first monomer position (the left-most column in the field file), regardless of the core monomer that will actually be used for the generated guess. In single-use calculations, this organization may seem counter-intuitive since the user likely knows which monomer will be in the core. When the user allows `pscfFieldGen` to automatically select the core monomer, however, this requirement ensures that the program knows which coefficients to assign to the core.

When run, `pscfFieldGen` creates a symmetry-adapted field file and parameter file for an internal subprocess execution of PSCF which generates a real-space concentration field, called the intermediate field in Fig. 3.3. From this point, `pscfFieldGen` generates the initial guess according to the flow chart depicted in Fig. 3.3. The intermediate field is used to generate a cumulative density function $f(\rho_\alpha)$ of grid points and selects an isovalue c as the volume fraction of core monomer α for which a fraction $f(c) = \phi_\beta$ of the grid points meet the criteria that $\rho_\alpha(\boldsymbol{r}) \leq c$. This is illustrated on the histogram in Fig. 3.3 with the overlaid bold horizontal and vertical lines indicating, respectively,

*The homogeneous basis function serves only to shift the resultant concentration fields uniformly up or down in value. This uniform shift will be reflected in the isovalue but will not change the position of the level surface; thus it does not impact the initial guess.

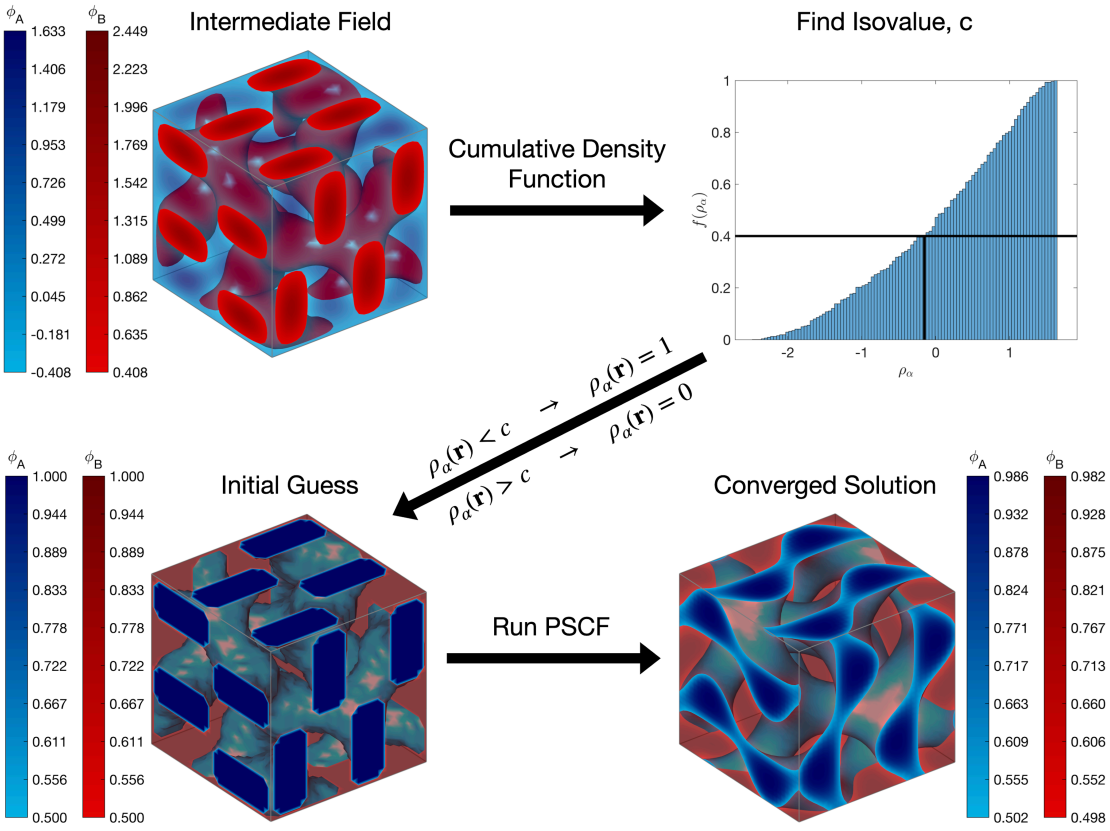

Figure 3.3: A flow chart representing the level set method after PSCF has been used to convert the initial basis functions to the intermediate concentration field (top-left). The $\rho_A(\boldsymbol{r})$ from the intermediate field is used to compute a cumulative density function (cdf), as shown in the histogram (top right). The volume fraction of A at which the cdf has a value equal to f_A is chosen as the isovalue, c. This isovalue is used to identify grid points within the level surface and construct the initial guess (bottom left). Running PSCF on the initial guess yields a converged field (bottom right). Example here is a double-gyroid phase with $\chi N = 20$, $f_A = 0.4$ for an AB diblock using a $32 \times 32 \times 32$ grid.

conditions of $f(\rho_\alpha) = \phi_\alpha$ and $\rho_\alpha = c$. The intermediate field is then used to generate the initial guess by assigning $\rho_\alpha^{\text{guess}}(\boldsymbol{r}) = 1$ at any position where $\rho_\alpha^{\text{intermediate}}(\boldsymbol{r}) \leq c$. The remaining positions (those outside the level surface) are then filled with non-core monomers assuming the matrix to be well-mixed, i.e. $\rho_{\beta\neq\alpha}^{\text{guess}}(\boldsymbol{r}) = \phi_\beta / (1 - \phi_\alpha)$ for positions where $\rho_\alpha^{\text{intermediate}}(\boldsymbol{r}) > c$. It is interesting to note that, due to the isovalue definition used in this methodology, the intermediate field appears, when visualized, to be the inverse of the generated guess, although the numerical values in this intermediate

concentration field are far from physically relevant.

We discuss in Section 3.2 that it is typically preferable to start with softer interfaces in the initial guess and let the iterator sharpen the transitions. This idea was, in fact, the entire motivation behind the introduction of the Gaussian smearing factor. Despite this, the guess generated here contains only infinitely sharp interfaces.* This choice can largely be ascribed to the nature of the methods: the form-factor method operates in Fourier space, where introduction of Gaussian smearing represents a trivial additional step in a coefficient calculation that is being done anyway; the level-set method, operating in real space, would require messier processing steps to introduce similar smearing. In practice, the sharp interfaces in these initial guesses can typically be relaxed by the SCFT iterator without too much difficulty. Thus, the additional complexity required to introduce interface smearing to level set method has not been deemed necessary.

3.4 Lamellae

Among structures handled by `pscfFieldGen`, lamellae are by far the simplest. Consisting of periodic layers of monomer separated by flat interfaces (in the bulk, mean-field limit), they involve compositional variation along only one dimension, orthogonal to the interfaces. Naturally, such a simple structure requires only the most basic generation algorithm.

As with the other methods discussed in this chapter, the lamellar initial guess is generated based on a reference monomer α. Likewise, this monomer is chosen as that with the lowest overall volume fraction ϕ_α in the system. The lamellar structure is initialized using only two basis functions to define a concentration profile. The homogeneous basis function coefficient for each monomer α is set equal to the monomer's overall volume fraction ϕ_α. Spatial variation is introduced using the next basis function. Here, the reference monomer α is assigned a basis function coefficient equal to $\phi_\alpha/\sqrt{2}$, where division by $\sqrt{2}$ relates to the relates to the basis function's multiplicity of two (i.e. that the basis function represents two equivallent wave vectors). These first two

*All grid points either contain pure core monomer, or zero core monomer, with the interface obscured between neighboring grid points.

basis function coefficients initialize the reference monomer concentration profile, $\rho_\alpha(\boldsymbol{r})$, as a single-period sinusoidal wave with equal amplitude and average value of ϕ_α. In this initialization scheme, the reference monomer will always have $\rho_\alpha(\boldsymbol{r} = 0.5d) = 0$. Other monomers are treated as well mixed, with coefficients set to enforce incompressibility.

The simplicity of this initialization method also means that the choice of reference monomer must be restricted. In this scheme, the reference monomer is set such that it will have a minimum local volume fraction of zero at the midpoint of the unit cell, and the amplitudes of all other monomer composition profiles are scaled according to this reference. If the reference monomer is not the one with the lowest overall volume fraction, it is possible that a lower concentration monomer could be initialized with local volume fractions dropping below zero. Take, for example, the case of a neat diblock copolymer. If the majority component is chosen as the reference monomer and has $\phi_\alpha > 0.5$, the local volume fraction profile would be initialized with an equal amplitude. This would result in a maximum local volume fraction for the reference monomer of $2\phi_\alpha > 1$ which represents a nonphysical local volume fraction. To ensure initial guesses do not contain nonphysical volume fractions, the user is not able to select or restrict the reference monomer choice for lamellae; rather, the lowest overall volume fraction is always chosen.

3.5 Conclusion

The `pscfFieldGen` software is a valuable tool to simplify the critical task of producing initial guesses for SCFT calculations of novel phases or known phases in new design spaces. The software generalizes the form-factor and level-set methods described in prior literature[61,72,74,75] expanding the potential base of users by removing the need to write specialized scripts for each phase and calculation. The software produces reliable initial guesses with a relatively simple input. Despite the value of the software, there are constraints and limitations to the tool as it is presently implemented. Currently, only one monomer may be selected as the core for the structures. This means that more complex or exotic structures, such as the Janus-like structures recently investigated by Xie et al.,[77] will not be accessible.

Chapter 4

A Software Platform for Block Polymer Inverse Design[†]

4.1 Introduction

As discussed in Chapter 1, the neat diblock copolymer exhibits a rich array of nanostructured morphologies based on only its three dimensionless parameters: the volume fraction of block A, f_A, defining chain composition; conformational asymmetry, $\epsilon = b_A/b_B$ where b_i is the statistical segment length of chemistry i; and the segregation strength, $\chi_{AB}N$, consisting of the temperature-dependent Flory-Huggins interaction parameter, χ_{AB}, and degree of polymerization, N. Going beyond the capabilities of the diblock copolymer melt requires adding more blocks, which quickly increases the complexity of the problem.[1] Simply adding one additional block to a triblock polymer increases the number of possible morphologies, even for something as simple as the particle-forming phases,[78] while also increasing the dimensionality of the design space. Adding yet another block using the same palette of three monomers produces a tetrablock terpolymer, a system that has proven to be a particularly fruitful avenue for materials discovery.[28,44,77,79–83] Here, each of the nine available block sequences (ABAC, ABCA, ACAB, BABC, etc.) offers an 8-dimensional design space, with three segregation strengths, three independent block fractions, and two statistical segment length

[†]This chapter is adapted from Logan J. Case, Kris T. Delaney, Glenn H. Fredrickson, Frank S. Bates, and Kevin D. Dorfman *The European Physical Journal E* **2021**, *44*(9), 115. (Ref. 71)

ratios. Adding more blocks and chemistries leads to factorial growth in the number of block sequences of linear polymers in addition to new block fractions, segregation strengths, and segment lengths.[1] Still more degrees of freedom become available when considering branching architectures or multi-component blends.[3,84–88] Thorough experimental exploration of such vast design spaces is infeasible.

A more efficient paradigm computationally screens large design spaces to identify regions where a desired morphology is likely to occur, and then uses these promising regions to guide experimental study or a more thorough computational analysis of the region. Indeed, theory has often played a central role in driving and rationalizing the discovery of new phases in diblock copolymer melts cited at the outset.[13,18,22,31] The question then becomes: how should this computational screening be done? The exhaustive grid searches used in the traditional, forward approach to these design problems become prohibitively expensive for high-dimensionality systems, forcing researchers to constrain the design spaces. Examples of such constrictions can be seen in previous cases where theory played a key role in driving experiments.[22,26,44,79,89,90] A particularly relevant example of such theory-driven collaborations is the work of Chanpuriya et al.[79] Leveraging prior experimental findings, they focused on poly(styrene)-*b*-poly(isoprene)-*b*-poly(styrene)′-*b*-poly(ethylene oxide) (SIS′O) at fixed temperature,[79] thus fixing the block sequence, Flory-Huggins parameters and statistical segment lengths (eliminating six degrees of freedom). They further constrained their search by fixing the degree of polymerization of the SIS′ parent triblock as well as the ratio of total styrene (in both blocks) to isoprene in that parent triblock.[79] Ultimately, their search considered only two design parameters from the nine possible degrees of freedom: distribution of styrene between the S and S′ blocks, and the block fraction of ethylene oxide, the latter of which was constrained further to low volume fractions to focus on the sphere-forming region. Their calculations predicted the emergence of the Frank-Kasper σ phase; accompanying experiments not only confirmed the existence of σ, but identified even more morphologies including an A15 phase.[79] In another example, Liu et al.[44] presented a theoretical study of binary blends of AB diblock copolymer, and predicted the formation of Frank-Kasper phases, including σ and A15. A blend of two AB diblock copolymers offers six degrees of freedom, including two block fractions, a segregation strength, a conformational asymmetry, a blend fraction, and a length ratio between the two chains. To make

their analysis feasible, they were forced to constrain their system to conformationally symmetric diblocks with fixed segregation strength and one fixed block fraction. Of the remaining three variables, their grid searches varied only the blend fraction and block length ratio, while restricting the second block fractions to two cases: equivalent majority blocks in both chains, or fixed length of the second minority block.[44] Recent experiments, inspired by these calculations, have confirmed the emergence of σ and A15, among other morphologies, in similar binary diblock blends.[43,91] These works offer valuable examples of theory guiding experimental discovery, but also highlight the compromises required to make exhaustive searches computationally feasible.

An alternative to a constrained grid search is inverse design. Here, a guided search of the design space is performed using optimization algorithms set to target a particular property.[92] Various methods have been proposed for such inverse design protocols in block polymers,[93–96] including Monte-Carlo[97,98] and evolutionary[99–101] algorithms. Most of this work, however, focuses on directed self-assembly in thin films, rather than the less-constrained problem of bulk morphologies.

The approach we choose to pursue here applies particle swarm optimization (PSO) in conjunction with self-consistent field theory (SCFT) calculations to the problem of block polymer design. SCFT serves as the compute engine to determine the fitness of a given morphology, and the motion through the design space is controlled by PSO, which emerged from the study of biological swarming behavior seen in, *e.g.*, birds, insects, and fish[102,103] and has been applied to a diverse range of problems including predictions of crystal structures,[104] mechanical structure design,[105,106] scheduling,[107] and robotics.[108] Similar to the biological case, the PSO algorithm relies on communication among several individuals ("particles" or "agents") to direct the movement of the group ("swarm") as a whole towards a region of high fitness,[102,103] which will correspond in our case to a low free energy for the desired block polymer morphology when compared to all competing candidate phases. As each agent moves through hyperspace, they gain more knowledge about the likely location of the global optimum, and communicate this information with the rest of the swarm until the group reaches a consensus.[102,103] This idea is illustrated in Fig. 4.1.

PSO has been used previously in two studies of block polymer phase behavior. Paradiso et al.[109] first demonstrated the ability of the PSO algorithm to search block

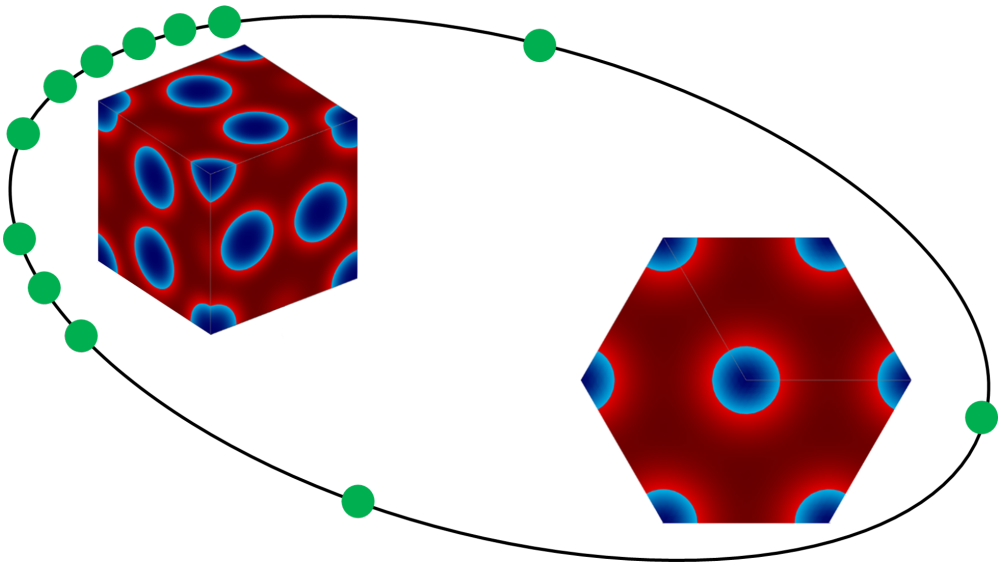

Figure 4.1: An abstract representation of the PSO search algorithm in which agents (green circles) skew along their ring communication graph toward a target phase (A15) and away from a competitor (hex). Figure reproduced from Ref. 71.

polymer parameters for those that favored particular morphologies in thin films. This work leveraged the reduced dimensionality of thin-film systems to simplify the forward problem of determining an equilibrium morphology for a given set of polymer parameters. Khadilkar et al.[110] introduced the additional complexity of metastability in bulk morphologies. In this case, they leveraged free energy differences among a set of predefined competing morphologies to demonstrate PSO's capacity to sort among these metastable competitors to identify regions of stability for bulk morphologies. These works demonstrate the potential for PSO to be deployed as a materials discovery engine for block polymer design. However, they were developed in the context of a custom software code that poses an obstacle to more widespread use.

To make PSO more broadly accessible to the block polymer community, the present work adapts the previous PSO approach for bulk morphologies[110] into an open-source software package for the design of block polymers. The work described here diverges from that of Khadilkar et al.[110] in two important ways. First, our program, called `pscfInverse`,[111] is distributed freely as an open-source wrapper around the open-source

Polymer Self-Consistent Field (PSCF) software,[61] with which users may already be familiar. Second, we attempt to lower the barrier to use by non-computational research groups by seeding SCFT calculations with algorithmically generated fields, rather than a pre-computed library. By operating in this way, we reduce the set-up work required of the user to prepare for the calculation. This new tool for algorithmic initial guess generation, called `pscfFieldGen`[111] and described in Chapter 3, should also find utility in stand-alone SCFT calculations where previous solutions are unavailable, e.g., when analyzing a promising new morphology. The robustness of the PSO tool is demonstrated through the solution of two simple two-dimensional search problems for conformationally symmetric diblock copolymers, and a more challenging and computationally intense three-dimensional search for the Frank-Kasper σ phase for a conformationally asymmetric diblock polymer.

4.2 Algorithm and Implementation

4.2.1 Particle Swarm Optimization

In many biological systems, large groups of individual organisms demonstrate the ability to move with a great deal of cohesion as a group. A flock of dozens or hundreds of birds will fly, as a group, to the center of a field after a handful or bucket of seed is thrown. A school of fish will dynamically dodge the advances of a predator. In each case, the movement of the group relies on coordination and communication among numerous individuals. The Particle Swarm Optimization (PSO) algorithm evolved from the study of these highly complex biological systems.[102,103] Like in the biological case, this heuristic algorithm leverages communication among a group (swarm) of individuals (agents) to achieve a group objective.[102,103] Like birds responding to the position and motion of their neighbors to guide their own descent to seeds in a field, the agents in a PSO swarm communicate data about their individual experiences with their neighbors to guide the swarm as a whole to the global extrema of a specified objective function.[102,103,112]

Analogies aside, the basis of the PSO algorithm is using network communication to facilitate decentralized decision-making and consensus-building as a means to solve a global optimization problem. For a search in D-dimensions, each agent i tracks its position $\boldsymbol{x}_i = (x_{i1}, x_{i2}, ..., x_{iD})$, and its velocity $\boldsymbol{v}_i = (v_{i1}, v_{i2}, ..., v_{iD})$. At each position

it visits, the agent computes the objective function $\Omega(\boldsymbol{x}_i)$ to measure the fitness of that position. To maintain a historical record of its experience, the agent additionally tracks the "personal" best seen position in its history, $\boldsymbol{p}_i = (p_{i1}, p_{i2}, ..., p_{iD})$ as well as the fitness of that personal best position. The agent keeps this personal best position up to date by comparing the fitness of each new position visited to the fitness of its personal best position and, if the new position has a better fitness, setting the new position as its personal best.

For PSO to work, it is not sufficient that each agent track its personal experience: agents must also be able to communicate those experiences. Early formulations of the PSO algorithm used Euclidean distance within the search space to determine the "neighbors" with which each agent could communicate.[112] As the algorithm advanced, this Euclidean neighbor criterion was replaced with a less computationally intensive graph-based approach.[112] With a graph-based communication network, each agent is able to communicate only with a fixed set of neighbors, regardless of position within the search space. In the current implementation, we use a ring-graph communication topology, depicted in Fig. 4.2, which allows each agent i to communicate with two neighbors, $i+1$ and $i-1$, and using index-wrapping such that the first and last agents are mutually communicable neighbors. For a swarm with the ring communication topology illustrated in Fig. 4.2, agent 2 would be able to communicate with agents 2 and 4, while index wrapping makes it so that agent 1 is able to communicate with agents 2 and 8.

At each PSO iteration, the agent i first determines the "global" best position visited by any of its neighbors $\boldsymbol{g}_i = (g_{i1}, g_{i2}, ..., g_{iD})$ by comparing the fitnesses of the neighbors' personal best positions. This global best position is then used to update the agent's position and velocity according to[112]

$$\boldsymbol{v}_i^{(k+1)} = \gamma \left[\boldsymbol{v}_i^{(k)} + c_1 \boldsymbol{\epsilon}_1 \odot \left(\boldsymbol{p}_i - \boldsymbol{x}_i^{(k)} \right) + c_2 \boldsymbol{\epsilon}_2 \odot \left(\boldsymbol{g}_i - \boldsymbol{x}_i^{(k)} \right) \right] \tag{4.1}$$

$$\boldsymbol{x}_i^{(k+1)} = \boldsymbol{x}_i^{(k)} + \boldsymbol{v}_i^{(k+1)} \tag{4.2}$$

where superscripts are used to indicate the old (k) and new $(k+1)$ values of position and velocity, and where $\odot$ indicates the Hadamard product of two vectors. Here, the positional update equation is greatly simplified by the use of a unit time-step, and requires little discussion. Several aspects of the velocity update equation, however,

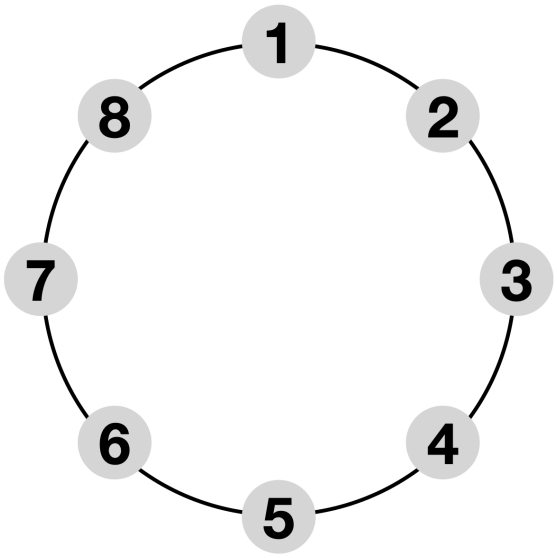

Figure 4.2: The ring-graph communication topology used in the current implementation of the PSO algorithm to define the neighbors with which each agent in the swarm can communicate. This illustration depicts a swarm of 8 agents with each individual labeled with an ID number from 1-8.

should be discussed. The acceleration of the agent is proportional to its distance in each search dimension from both its personal and global best positions; the further the agent is from either "best" position, the potentially stronger the accelerating pull of that reference will be. The actual contribution of each acceleration term varies according to the values of random vectors $\boldsymbol{\epsilon}_1$ and $\boldsymbol{\epsilon}_2$. These vectors are randomized for each agent at each step with elements on $(0, 1]$. Two scalar weighting factors, c_1 and c_2, are also applied to each acceleration term. Finally, γ is a scalar constriction factor in the range $(0, 1]$. Based on a stability analysis of the algorithm,[113] the standard formulation of PSO recommends values of $\gamma = 0.72984$ and $c_1 = c_2 = 2.05$ for the constriction and weighting factors, respectively.

In order to define an objective function for use in this PSO algorithm, we need to consider how SCFT is generally used to determine phase stability. When using SCFT to determine the most stable phase at any position in state space, the intensive free energies of the candidate phases are compared, with the stable phase being that with the lowest free energy (in absence of phase separation). By this metric, a "target" phase in a design will be stable when its free energy is lower than that of any competitor. To

maximize the likelihood of observing a target phase, we would like to find a point not just where it has the lowest free energy among competitors, but where it has the lowest free energy *by the greatest margin.* Therefore, for a PSO search targeting phase T against a set of competitors C we use the SCFT-computed intensive free energy, F, of each phase to compute an objective function[110]

$$\Omega = \min_{m \in C} (F_m) - F_T \tag{4.3}$$

which uses a sign convention in which phase T is stable when $\Omega > 0$. Based on this sign convention and the goal of maximizing the margin of target phase stability, the algorithm seeks to maximize the objective function.

4.2.2 Parameter Mapping

In the PSO inverse design approach, SCFT is used to solve the forward problem of phase stability at a particular set of polymer parameters while the PSO wrapper iteratively updates the polymer parameters in an attempt to maximize the objective function. For the PSO parameter updates to have any effect, however, updates to the parameters being searched by the outer PSO optimizer must be communicated to the inner, forward solver as SCFT-relevant values. In other words, there must be some explicit map between the parameters searched by PSO and the parameters required to set up and run an SCFT calculation. The most obvious such mapping is a 1:1 direct map in which the PSO algorithm directly searches degrees of polymerization, statistical segment lengths, Flory-Huggins parameters, etc. This approach would be simple, easy to implement, and quite transparent and straightforward from the perspective of usability. A substantial drawback to this mapping, however, is that it provides the user with very little flexibility in defining their search. In a direct-map scheme, there is no way to relate parameters and no mechanism for more nuanced control of the search. For example, a direct map would offer no mechanism by which Chanpuriya et al.[79] could control the distribution of styrene between the S and S′ blocks of the SIS′O tetrablock terpolymer studied in their work.

To provide more flexible control of searches, `pscfInverse` defines PSO search variables and constraints as "relationships" among polymer parameters. These parameter

relationships were designed with two particular goals in mind. First, as long as the system is properly specified by the available variables and constraints, there should be an analytical solution for the PSO-to-SCFT mapping.* To achieve this goal, each parameter relationship is designed to be linearizable in terms of the SCFT-relevant polymer parameters. Ensuring that all variables and constraints are linearizable means that at each position in the PSO search space, the variables and constraints can be used to construct a set of linear equations of the form $\underline{\underline{A}}\ \underline{x} = \underline{b}$ in which the solution $\underline{x}$ contains the value of each SCFT-relevant polymer parameter. For a properly specified system, this system of equations will always have a unique solution that is easy to compute. Second, the relationships should make few (if any) assumptions about the structure of the underlying system. This goal relates most specifically to the polymer structures themselves, particularly regarding the order of blocks in a polymer, which chemistries they may contain, or whether or not the polymer is branched. As will be described later, this is achieved by using only a polymer index and block index to reference polymer structure. This structure-agnostic approach to PSO definition promotes simplicity in program input while allowing flexibility in the types of systems that can be studied, or which softwares can be interfaced with the PSO wrapper. The five parameter relationships currently defined in `pscfInverse` are described in the following paragraphs and are summarized in Table 4.1.

The composition of polymer chains is defined through two types of parameter relationships, both of which relate block degrees of polymerization (referred to here as the "block length"). The first is the total block length, L_T. As the name implies, this relationship is defined as the sum of the lengths of a set of blocks i according to $L_T = \sum N_j$. This relationship trivially meets the linearizability criterion, being linear as defined. The second relationship is a logarithmic ratio of block length sums. For this relationship, two different sets of blocks are defined; one set is designated to be accounted in the numerator of the ratio, while the other is designated to be accounted in the denominator. The ratio was given a logarithmic scaling to balance the numerical representation of a ratio with its reciprocal within the PSO search bounds. Functionally,

*Existence of an analytical solution avoids any potential problem with convergence that could occur if iterative methods were needed to solve the mapping.

Table 4.1: Parameter relationships available for use as PSO search variables or search constraints in `pscfInverse`, including their definition and linearized form.

	Definition	**Linearization**
Block Length		
Total block length	$L_T = \sum N_j$	$\sum (1)(N_j) = L_T$
Block length ratio	$L_R = \ln\left(\frac{\sum N_n}{\sum N_d}\right)$	$\sum_n (1)(N_n) - \sum_d \exp(L_R) N_d = 0$
Statistical Segment Length (SSL)		
SSL	$S_L = b_\alpha$	$(1)(b_\alpha) = S_L$
SSL ratio	$S_R = \ln \frac{b_\alpha}{b_\beta}$	$(1)(b_\alpha) - \exp(S_R)(b_\beta) = 0$
Segregation Strength		
Flory-Huggins parameter	$X = \chi$	$(1)(\chi) = X$

the ratio is defined for numerator blocks n and denominator blocks d as

$$L_R = \ln\left(\frac{\sum N_n}{\sum N_d}\right)$$

which can be linearized by moving the value L_R into an exponential coefficient for the denominator blocks according to

$$\sum_n (1)(N_n) - \sum_d \exp(L_R) N_d = 0$$

If any blocks are designated to be accounted in both the numerator and denominator, coefficients contributed from the numerator and denominator would simply be added, resulting in a coefficient of $[1 - \exp(L_R)]$ for that block. In both of these parameter relationships, the blocks that are accounted in any given set are specified according to a polymer and block index only. The mapping of these indices to a polymer structure is handled by the SCFT file managers, making the PSO interface independent of the polymer structures. This formulation provides a high degree of flexibility to the types of structural variables that can be considered.

The relationship definitions for statistical segment length and Flory-Huggins parameters are simpler than those for polymer composition and demand far less discussion. Like polymer composition, statistical segment lengths have two relationship types. The

first is a direct map of the statistical segment length, $S_L = b_\alpha$ which is analogous to the total block length, but restricted to one species. The second is the logarithmic statistical segment length ratio, $S_R = \ln(b_\alpha/b_\beta)$, Similar to the block length ratio, the statistical segment length ratio is linearizable by moving S_R into an exponential coefficient yielding $(1)(b_\alpha) - \exp(S_R)(b_\beta) = 0$. Also similarly to the block length ratio, logarithmic scaling was chosen to balance representation of a ratio with its reciprocal. Finally, the Flory-Huggins parameters currently only have the option of a direct map.

4.2.3 SCFT Initialization and Convergence

The importance of the initial guess in SCFT calculations was already discussed at some length in Chapter 3. In the context of this inverse design methodology, the results produced by that initial guess (following SCFT convergence) are used to establish the fitness of a given point in the search space. Reliance of the inverse design protocol on the results of the forward SCFT calculation make this guess all the more critical. The initial guess for each calculation must be of sufficient quality to ensure that fitness values at each point in the search space are repeatable.* In prior work, Khadilkar et al.[110] accomplished this repeatability by initializing calculations from a pre-computed library of defect-free seed fields, selected from each phase's known stability windows. From these seed fields, parameters would be swept to the appropriate PSO search position to determine the fitness. As discussed in Chapter 3, sweeping from a converged field to a new desired position in phase space can be a highly efficient approach. For an inverse design methodology, however, this approach has some drawbacks.

First, regardless of the system being studied, collecting these seed fields requires substantial effort: running a moderate to large set of test calculations, and then manually confirming that each converge field is defect-free. These seed fields need not necessarily be collected from a region in which the phase is thermodynamically stable, only regions in which the phase is "numerically stable" meaning that SCFT calculations of the phase will reliably converge without substantial difficulty. Generally, these numerical stability regions for a phase will coincide with those in which the phase is either thermodynamically stable or competitively metastable. Thus, for well-studied systems, numerical stability windows will generally be known or easily inferred. For novel design

*To within reasonable numerical tolerance, of course...

spaces (those in which automated inverse design protocols are most useful) knowledge of numerical stability regions may not exist. In such cases, a researcher would need to manually explore the design space for each phase's numerical stability windows from which seed fields could be collected. If the design space is large and complex, or if the user's intuition when predicting "likely" numerically stable regions is unreliable, this preliminary search can become quite expensive; in the extreme case, it could devolve into the unguided grid search the PSO methodology is proposed to replace.

Following collection of the seed fields, the user still must make the fields accessible for the search. This would first require indexing and databasing the seed fields in some way to that the software can access them. Then, a querying protocol must be defined to identify the "best" seed field from which to start based on the current position in phase space. Automating the indexing, databasing, and query setup in a manner accessible to those without experience in database design and use, but still flexible enough to handle the wide variety of polymer systems that could be explored is a complicated endeavor.

Finally, in order to be reliable and efficient, the curated library would need to be reasonably representative of the targeted search area. Efficient application of the library methodology necessarily assumes that failure of a sweep to reach a target position indicates that the phase will not be thermodynamically competitive at that position. If the seed library is representative of the search space, this is a reasonable assumption. If the library is *not* representative of the search space, a region of stability or competitive metastability for a phase could be separated from the seed fields by a region of numerical instability. In this case, a sweep would be unable to pass through the numerically unstable region and the metastability region would be hidden from the search.

For these reasons, `pscfInverse` does not make use of library initialization. Instead, it has been designed to rely on algorithmic generation of initial guesses by interfacing with the `pscfFieldGen` software discussed in Chapter 3. By making use of algorithmic guess generation, `pscfInverse` lowers the barrier to running a calculation by eliminating the library-building steps.

4.2.4 Robustness of SCFT Calculations

Calculation of fitness values for the PSO algorithm requires that accurate free energies be obtained from SCFT calculations. However, converging a solution of the highly

nonlinear SCFT equations is a nontrivial task, and numerical errors are not uncommon. When calculations are being launched and monitored by a researcher, such errors are typically easy to identify and correct. In the context of an automated design process such as PSO, these calculations are being launched, and their results are being processed, by the algorithm itself, with limited human monitoring. It is imperative that the algorithm have safeguards in place to identify and respond to a variety of numerical inaccuracies that occur during SCFT calculations.

After an SCFT calculation completes, `pscfInverse` checks for four potential errors. The first, and by far the most common, is a calculation failing to reach convergence. This is detected by simply comparing the allowed iterations for the calculation to the iterations used; if more iterations are reported than are allowed, the calculation failed to reach convergence. The second error considered is the case of numerical divergence. Although it is exceedingly rare, the program can occasionally encounter a numerical instability which results in PSCF reporting non-numeric or infinite energies. If this is detected, the calculation is also flagged as unsuccessful. The third error, convergence to a defective field, is the most subtle and the most difficult to detect. Even with symmetry constraints, it is possible for a calculation to converge to disorder or a supergroup structure.[110,114] To screen for these errors, `pscfInverse` checks for similarity between the initial guess and the final converged fields by calculating the inner product of the normalized Fourier modes. By definition of the inner product, orthogonal fields with no appreciable similarity will have an inner product of zero. At the other extreme, two identical fields will yield a normalized inner product of unity. In this way, the normalized inner product provides a bounded scale on which to measure similarity between fields. Screening converged fields by their similarity to the initial guess requires only setting a minimum threshold value for the normalized inner product below which the converged field is assumed to be defective and therefore rejected. According to our testing, this similarity check is generally sufficient both to screen for collapse to disorder and to detect supergroup and defect emergence using a threshold value of 0.7. Despite general reliability, the similarity check is not perfect and its effectiveness can vary between phases depending on phase compexity and initialization method. In our testing, the lamellar phase seems to be a particularly poor match for this check due to its simplicity. Initializing lamellar structures using only two basis modes (with one being

the homogeneous basis function which is invariant in the canonical ensemble) leaves very little data on which to compare the initial and final structures. This restriction makes it very difficult for lamellar structures to *not* pass the similarity check, the effects of which are discussed further in Section 4.3. Due to the imperfection of the similarity check, manual inspection by the researchers of converged SCFT calculations obtained from the PSO search could be useful to identify any defective or supergroup fields that might be erroneously accepted. In direct response to the issues observed with the similarity check for lamellar structures, an optional fourth error check was added which would screen for convergence to disorder by calculating the absolute variation in the real-space concentration fields. This check considers the difference between the maximum and minimum local volume fractions of each monomer in the converged field (i.e. the maximum variation in the monomer field), and rejects the solution if the difference between these volume fractions is below a user-defined threshold for all monomers.

If an error is detected in a phase's SCFT calculation, the reported energy from PSCF will be neglected and the phase is assigned an arbitrarily high free energy.* The assignment of this arbitrarily high free energy automatically leads, through the definition of the objective function, to the appropriate response by the software. If the error is detected for a competing phase, that phase is unlikely to factor into the fitness calculation at all, as another phase is likely to have a finite (i.e. lower) free energy, and be identified as the most stable competitor. If the error is detected for the target phase, the fitness for that point in phase space will become $\Omega = -\infty$. In determination of an agent's personal best fitness, any position of target phase numerical stability will be favored as the best position. In communication with neighbors, favor will again always be given to positions of numerical stability. Thus, as the search progresses, memory of the numerically unstable position will slowly fade from the swarm's memory in favor of positions at which data are available; in turn, the position's impact on the search is then minimized.

*In particular, the phase will be assigned an energy equal to `numpy.inf`, rather than an arbitrary numerical value.

4.3 Case Studies

4.3.1 Classical Phases in Diblock Copolymers

When testing any software, it is often best to start with the simplest cases before moving on to more complex problems. In block polymers, the simplest system would be the single-component, conformationally symmetric ($\epsilon = 1$) diblock copolymer. Thus, for our initial tests, we run searches on the classical AB diblock copolymer phase diagram, varying chain composition and segregation strength. For these searches, we bound our chain composition search according to a block length ratio variable $-2.5 \leq \ln(f_\mathrm{A}/f_\mathrm{B}) \leq 2.5$ (approximately $0.0759 \leq f_A \leq 0.9241$), where we have also applied a total chain length constraint of $N_\mathrm{A} + N_\mathrm{B} = 1 = f_\mathrm{A} + f_\mathrm{B}$ to create a numerical equivalence between the block fraction and block degree of polymerization. We bound segregation strengths in the search to the range $10 \leq \chi N \leq 30$. To further simplify these initial searches, we consider only four phases: body-centered cubic spheres (bcc), hexagonally-packed cylinders (hex) double-gyroid (gyr), and lamellae (lam). We use a swarm of five agents, and run 100 PSO steps for each search.

Figure 4.3 shows the position and fitness histories from a search for the BCC phase in a conformationally symmetric diblock copolymer melt. Initially, the swarm has no positions within the stability window for spheres, leading the swarm to identify points in the lamellar region as the best seen positions. Within three steps, however, one agent identifies a point in the A-minority BCC window, near the coexistence line with cylinders. From here, an additional 27 steps are required before every agent has individually found a point where BCC is stable, during which time, positions were identified in both the A-minority and B-minority sphere regions. Identification of both windows leads the swarm to explore both stable regions rather than converging on just one side of the phase diagram. This behavior is most clearly illustrated by the presence of dense clusters in both upper corners of the search space in Fig. 4.3a, with a high number of late-step positions directly between those clusters as agents fly between the two regions. The positional diversity within the swarm enforced by these competing stability basins can be seen in Fig. 4.3c, where the range of current fitness values remains wide throughout the search. At the same time, the swarm's search emphasizes ever more promising regions, indicated by the reduced frequency of failed target-phase SCFT calculations

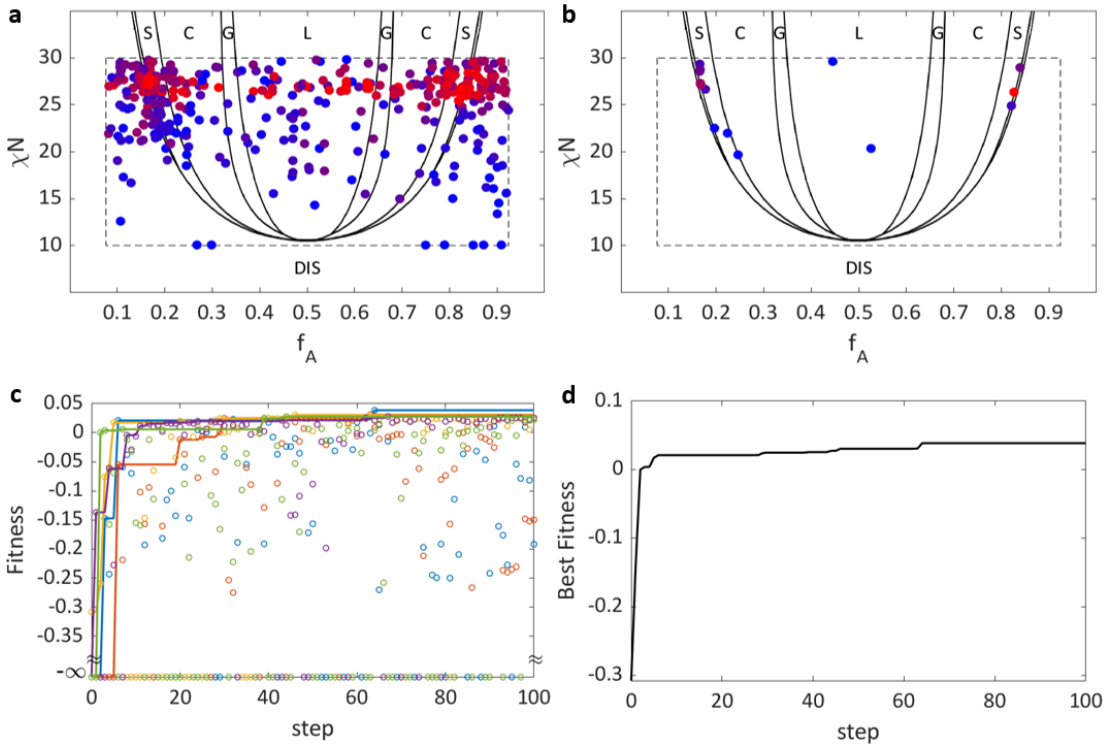

Figure 4.3: Results of a 2D search for BCC phase in a conformationally symmetric diblock copolymer melt showing (a) all positions visited during the search and (b) all positions that, at one time in the search, were the best found by the swarm, (c) current fitness (circles) and personal best seen fitness (lines) at each step for each agent and (d) the best fitness found by the swarm through each step. (a) and (b) are both plotted over the known diblock phase diagram (modified from Ref. 57) with the dotted line marking the search bounds and with point color varying from blue (early steps) to red (late steps). Figure reproduced from Ref. 71.

(indicated by points along the bottom axis), which are more likely farther from the target's stability window. Khadilkar et al.[110] presented a similar search for BCC in their demonstration of this method. In contrast to the results shown in Fig. 4.3, their search, which used four agents and ran 200 PSO steps, identified only the A-minority stability basin, and clustered primarily around that region. This difference illustrates both the randomness of the PSO search, which is affected by the initial positions and the number of agents, and the robustness, since both our search and the prior work[110] successfully found the BCC phase.

Changing the target to a lamellar phase, shown in Fig. 4.4, emphasizes the effect

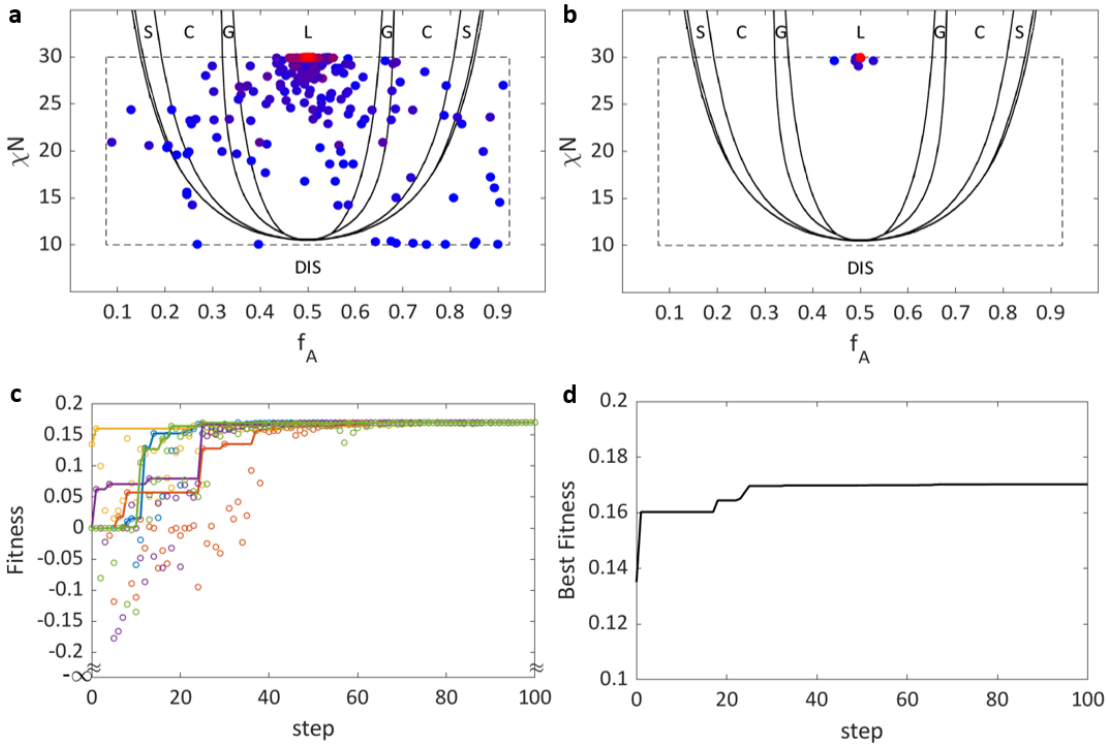

Figure 4.4: Results of a 2D search for the lamellar phase in a conformationally symmetric diblock copolymer melt showing (a) all positions visited during the search and (b) all positions that, at one time in the search, were the best found by the swarm, (c) current fitness (circles) and personal best seen fitness (lines) at each step for each agent and (d) the best fitness found by the swarm through each step. (a) and (b) are both plotted over the known diblock phase diagram (modified from Ref. 57) with the dotted line marking the search bounds and with point color varying from blue (early steps) to red (late steps). Figure reproduced from Ref. 71.

that competing stability basins can have on the PSO searches. Here, random initialization of agent positions serendipitously placed one of the agents at a point ($f_A \approx 0.45$, $\chi N \approx 29.64$) very close to the global optimum for the lamellar phase within the search window ($f_A = 0.5$, $\chi N = 30$). Although the swarm maintains some diversity in agent position early in the search, this fails to identify any reasonably competitive regions. Knowledge of the near-optimum from one agent's initial position quickly permeates the swarm and drives the search toward that point. Without any significant competing stability basins, each agent quickly finds positions high in the lamellar window. Once the personal best positions collapse to a small region, the swarm quickly loses momentum and converges around the global optimum by step 40. Tight clustering in Fig. 4.4a

shows this quick convergence, but the importance of diverse personal best positions for continued exploration can be seen in Fig. 4.4c. Around step 25, all but one agent has found a position very close to the global optimum; after that step, the only agent to not have found a near-optimum position is also the only one to stray noticeably from the rest of the swarm. Once that agent finds a near-optimum position, the whole swarm quickly settles at the optimum.

Comparing Fig. 4.3c and Fig. 4.4c reveals a sharp contrast in the number of "failed" target phase calculations, with none appearing in Fig. 4.4c. The small size and low dimensionality of the one-dimensional lamellar SCFT problem means that the calculation always converges within the maximum allowed number of iterations (set at 200). We observe that, rather than failing to converge as other phases often do in highly unfavorable regions of phase space, the lamellar calculations tend to collapse to disorder. At the same time, the simplicity of the initialized field (using only two basis functions) makes the similarity check ineffective. In this calculation, the concentration variation test was not used to check the final real-space concentration field, causing many calculations which converged to disorder to be erroneously accepted by the program. This can be seen in the clustering of points along $\Omega = 0$ in early steps. Despite the erroneous acceptance of these SCFT calculations, the PSO algorithm proved robust enough to tolerate the errors and yield a correct result. We repeated this calculation using the concentration range test such that any converged lamellar calculation with a total concentration range for each monomer below $\Delta\rho = 0.001$ would be rejected as defective; results are shown in Fig. 4.5. These results show that several calculations were identified as failed based on this criteria, evidenced by the appearance of several agent positions with $\Omega = -\infty$ in Fig. 4.5c. Given the rapid convergence in the original calculation and this rerun, however, the impact of these new positions is minimal.

4.3.2 Frank-Kasper σ in Diblock Copolymers

For a more challenging test of the software's capabilities, we next consider a search for the Frank-Kasper σ phase. Frank-Kasper phases offer a valuable route to increase the complexity of design problems in diblock polymer space, and serve as a more stringent test of the PSO algorithm. Not only do Frank-Kasper phases require expansion of the search into a third dimension to access conformationally asymmetric diblock polymers,

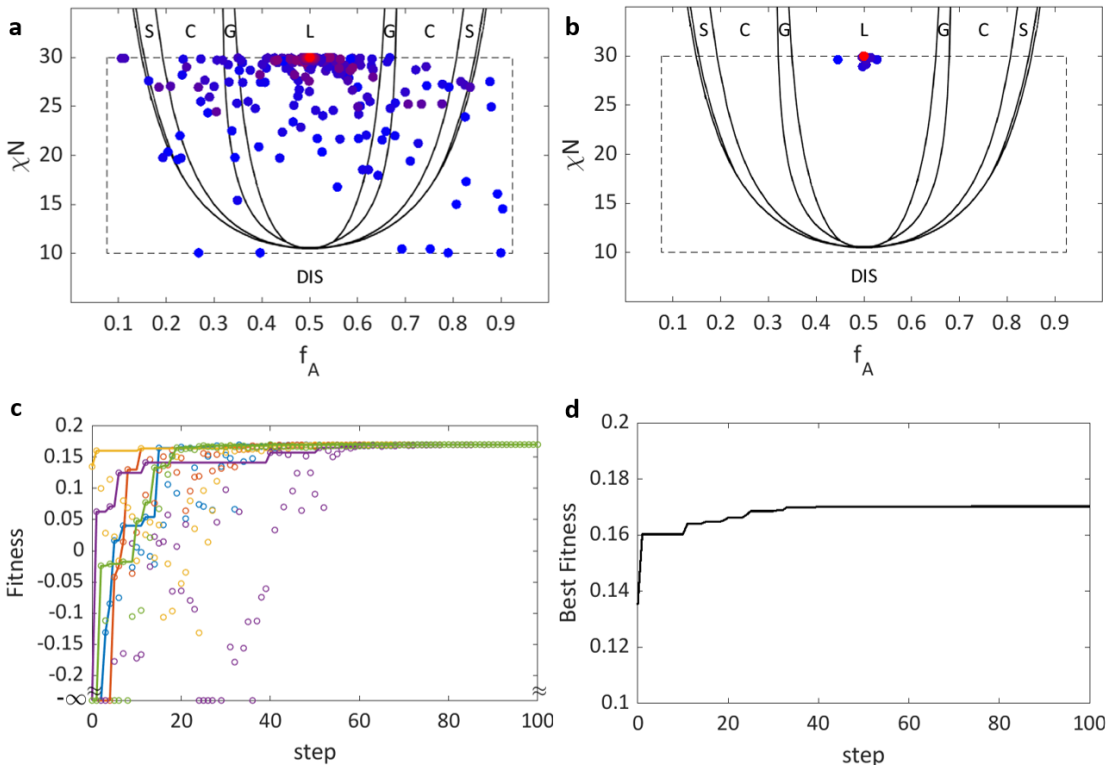

Figure 4.5: Results of a 2D search for the lamellar phase in a conformationally symmetric diblock copolymer melt using an explicit disorder check showing (a) all positions visited during the search and (b) all positions that, at one time in the search, were the best found by the swarm, (c) current fitness (circles) and personal best seen fitness (lines) at each step for each agent and (d) the best fitness found by the swarm through each step. (a) and (b) are both plotted over the known diblock phase diagram (modified from Ref. 57) with the dotted line marking the search bounds and with point color varying from blue (early steps) to red (late steps). Figure reproduced from Ref. 71.

but the near-degeneracy of the free energies of most Frank-Kasper phases[30,31,33] combined with the higher complexity of the Frank-Kasper structures themselves make the robustness of the automated SCFT protocols all the more critical. In this trial, we introduce conformational asymmetry, ϵ, as an additional design parameter in order to make Frank-Kasper phases accessible and allow it to vary on $1 \leq \epsilon \leq 2$. Chain composition is constrained as it was for the classical phases, with $-2.5 \leq \ln(f_A/f_B) \leq 2.5$. In comparison to the classical phases, the range for χN was reduced to $10 \leq \chi N \leq 20$ in order to restrict the size of the σ-stability window,[29] making for a more challenging search. The set of candidate phases for this last example is expanded to include FCC

spheres, as well as the Frank-Kasper σ and A15 phases. In the larger design space, we expand to a swarm of 10 agents, and again run 100 PSO steps.

Figure 4.6 shows results of a 3D search for the Frank-Kasper σ phase. With this particular set of random initial positions, the swarm initially has no agents at positions where σ is the stable phase, and most agents do not even successfully converge the target phase due to its relatively small volume in the phase space and the challenges in converging metastable σ phase solutions. By assigning failed convergence of σ to have infinite energy, rather than discarding the calculation, we force the swarm to move away from these numerically challenging regions of the state space, which tend to be regions far from the σ stability window. Early in the search, the swarm's best seen positions generally fall in or near the A-minority BCC stability windows at low ϵ. Early improvements in the swarm's best seen position do, however, trend toward higher χN

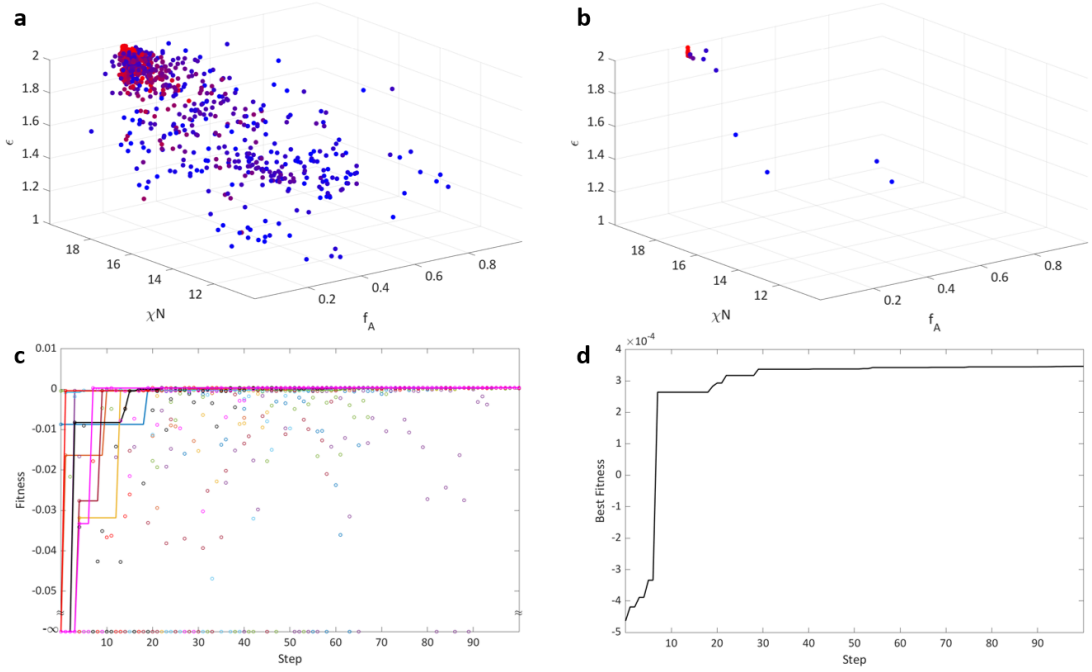

Figure 4.6: Results of a 3D search for sigma phase in a neat diblock copolymer melt showing (a) all positions visited during the search and (b) all positions that, at one time in the search, were the best found by the swarm, (c) current fitness (circles) and personal best seen fitness (lines) at each step for each agent and (d) the best fitness found by the swarm through each step. (a) and (b) also show search progression by varying point color from blue (early steps) to red (late steps). Figure reproduced from Ref. 71.

and ϵ, in the direction of the known σ phase stability window. Rather early in the search an agent identifies a position where σ is stable, after which the swarm gradually coalesces around the high-χN and high-ϵ σ phase stability window. Following the identification of a stable point, the swarm periodically identifies positions further within the stability basin, approaching a global optimum within the search space. During this time, reduced frequency of infinite fitness values in Fig. 4.6c as well as clustering in Fig. 4.6a indicate that the swarm narrows its search to areas where σ calculations readily converge.

4.4 Conclusion

This work introduces an open-source software package for the inverse design of linear block polymers to target bulk morphologies using PSO and SCFT. Unlike in prior applications of PSO to such design problems,[110] the present software package is made more accessible through the use of algorithmic generation of initial guess fields for SCFT calculations using broadly accessible software. Software functionality was demonstrated with design problems in the diblock polymer parameter space. The software successfully identified stability windows for BCC and lamellae in (f_A,χN) space, as well as σ in (f_A,χN,ϵ).

We have demonstrated a successful implementation of PSO for block polymer design using the open-source PSCF program, but several limitations of the existing tool should be noted. The present implementation uses the Fortran version of PSCF[61] for SCFT calculations, which restricts its application to linear polymers at this time. The `pscfInverse` program was designed to allow different SCFT solvers to be wrapped by the PSO code with relative ease, and extension to interface with the new C++ version, PSCFpp,[68] would enable design with the branched architectures available in the C++ code. Likewise, it should be relatively easy for users who already have their own SCFT code to implement this PSO wrapper with some modest modifications to provide compatibility with input/output files in their code. Moving toward consideration of branched architectures, further improvements to the PSO wrapper will be required to access the full polymer design space. For example, the nature of the PSO algorithm restricts searches to continuous variables, limiting its ability to search discretized design parameters such as the number or connectivity of blocks. Creative use of discrete ranges

on a continuous variable could enable access to such design parameters, but the program does not presently support this functionality. Other, more generic, improvements could also be implemented. The guess generation algorithms, as previously discussed, place limitations on the variety of phases that can be considered. Improvements to the guess-generation algorithms would further broaden the potential of the program. Finally, the method is unable to consider any morphology not in the set of candidate phases. Identification of unanticipated stable morphologies[115–118] remains a significant open question in block polymer material design.[1]

Testing of this tool has also uncovered a subtle difficulty in the application of this method. Fundamentally, this method relies on the ability of the SCFT solver to obtain converged fields for each phase in all regions of the search space where the phase is reasonably competitive and thus of interest in the search. We attempted a search for the A15 phase in the three-dimensional diblock parameter space, but were unable to obtain accurate results. Analysis of the results showed abnormally high failure rates for σ phase at high conformational asymmetry ($\epsilon > 2.5$) where A15 is known to become stable.[30] Since σ should be the closest competitor to A15 over much of this range, and should provide the lower bound to the A15 stability window in the f_A dimension, failure of these calculations proved significant and caused the swarm to converge on points in the σ phase window, rather than that of A15. The cause of these convergence problems in PSCF is presently unknown, but was only seen in the course of this work to impact σ at high conformational asymmetry. In general, understanding the convergence of SCFT calculations is a challenging issue[119] due to the nonlinear, non-local nature of the problem and the need to combine multiple numerical methods to achieve the solution. Convergence of SCFT will return as a theme in Chapter 6 of this thesis. Investigation and correction of this or similar convergence difficulties in PSCF or any other SCFT solver interfaced with this tool can enable application of the approach to more problems.

Although already less computationally expensive than brute-force grid searches,[110] there may be ways to further improve the efficiency of the PSO methodology. Acceleration of the underlying SCFT calculations, for example on a Graphics Processing Unit,[68,70] could reduce the overall run-time of the program. Adoption of a hybrid approach to initial field seeding, perhaps by combining a library and generation approach,

could also reduce the cost of underlying SCFT calculations by minimizing the repetition of more expensive generated-guess calculations at neighboring or identical points in phase space. Nevertheless, the open-source platform presented here represents a significant step toward the broader adoption of inverse design methodologies by providing a robust new tool for block polymer materials discovery via PSO to the research community.

Chapter 5

Conformational asymmetry in sphere-forming AB/B′C diblock polymer alloys[†]

5.1 Introduction

At sufficiently low temperature, a diblock copolymer melt will spontaneously order to balance the entropic cost of chain stretching against the increasing enthalpic penalty for unlike contacts as the temperature decreases. The selection of the ordered state is controlled, to a first approximation, by the segregation strength, $\chi_{\mathrm{AB}}N$, where χ_{AB} is the Flory-Huggins interaction parameter between monomers A and B and N is the total degree of polymerization, and the chain composition, characterized by the block fraction $f_{\mathrm{A}} = N_{\mathrm{A}}/N$ for a block with degree of polymerization N_{A}. These two parameters alone enable access to a range of equilibrium morphologies, including the body-centered cubic (bcc) and face-centered cubic (fcc) sphere phases, the hexagonally-packed cylinders (hex) phase, the double gyroid and O^{70} network phases, and the lamellar phase.[121] While χN and f_{A} are the two axes of the classical diblock copolymer phase diagram,[13,14,22,122] there exists a third parameter that impacts the selection of the ordered state: conformational asymmetry.

[†]This chapter is adapted from Logan J. Case, Frank S. Bates, and Kevin D. Dorfman, *Soft Matter* **2023**, *19*(1), 115. (Ref. 120)

5.1.1 Conformational Asymmetry and Frank-Kasper Phases

Conformational asymmetry quantifies the relative entropic cost of stretching two different blocks in a copolymer,[24] and can be produced through either architectural or elastic variations. Architecturally, branching structures introduce conformational asymmetry relative to the linear case when a linear block i having degree of polymerization N_i is replaced with n_i branches having degree of polymerization N_i/n_i.[26] This restructuring leaves the volume fraction of the block unchanged, but shortens the branch blocks which then incur a higher entropic penalty than the linear block to extend the same perpendicular distance from the interface when filling space. Elastic control of conformational asymmetry is done by changing the statistical segment length of one block relative to the other.[25,27] In this case, changes to the statistical segment length of a block impact both the preferred extension of the block, quantified by the block's radius of gyration, $R_g = b\,(N/6)^{1/2}$ and the Gaussian entropic penalty of stretching for the block, which is inversely proportional to statistical segment length.[26,123] Equivalence of the architectural and elastic contributions to conformational asymmetry only holds in the strong stretching (high χN) limit; at lower χN, deviation of the blocks from trajectories perpendicular to the interface impact the packing geometries available to branched architectures.[50] In this work, we consider only linear diblocks for which conformational asymmetry is expressed in terms of the statistical segment lengths, b_{A} and b_{B}, as $\epsilon_{\mathrm{AB}} = b_{\mathrm{A}}/b_{\mathrm{B}}$ where $\epsilon_{\mathrm{AB}} > 1$ indicates a lower entropic cost to stretch A than to stretch B and tends to favor interfacial curvature toward A.[24,26,124]

Recent interest in conformational asymmetry is connected to its importance in the formation of the Frank-Kasper phases in compositionally asymmetric neat diblock copolymer melts, where f_{A} is small.[28,30,33,125] Emergence of these Frank-Kasper phases, four of which are depicted in Fig. 5.1a, has been attributed to a tendency of these systems to imprint the Wigner-Seitz cell geometry onto the micelle core, in which case phases with more spherical* Wigner-Seitz cells (the Frank-Kasper phases) would be favored over phases with less spherical Wigner-Seitz cells (bcc). In this sphericity theory of Frank-Kasper phase emergence, the interfacial faceting which is central to the hypothesis emerges as a result of two effects as conformational asymmetry increases:

*It is known that a perfect sphere has a minimal ratio of surface area (interface) to volume (amount of polymer); thus sphericity here acts as a proxy for interfacial contact per volume.

(1) higher accessible core volume fractions for spherical micelle phases, and (2) greater deformability, or greater softness, of the micelle core.

In the first effect, particle phases remain stable at increasingly higher values of f_A because interfacial curvature toward the minority block becomes favored.[26,31,124] This property was exploited by Grason et al.[31] who predicted using self-consistent field theory (SCFT) the emergence of A15 between bcc and hex in conformationally asymmetric diblocks. Their argument starts with an analysis of the interfacial and stretching energies of sphere phases in the strong segregation limit. Assuming a perfectly spherical core, increasing f_A leads to reduced curvature of the interface.[31] This reduced interfacial curvature then reduces the restoring force produced by deformations of the interface.[31] In a crystalline assembly, the greater deformability of the interface causes the core to increasingly adopt the geometry of its Wigner-Seitz cell as f_A increases.[31] In this polyhedral interface limit (high f_A), they predict A15 to be the lowest energy sphere phase as a result of its minimized interfacial area, and despite the fact that bcc was expected to minimize chain stretching.[31] This potential A15 window was confirmed with SCFT, but predicted to occur in the hex regime for conformationally symmetric diblocks.[31] To better access this polyhedral interface regime, they used architecturally-derived conformational asymmetry to shift the sphere-forming region to higher f_A and predict with SCFT the emergence of an A15 window between bcc and hex.[31] Subsequent work has confirmed the emergence of Frank-Kasper phases between bcc and hex with increasing conformational asymmetry, although σ is the first to emerge at modest ϵ, with A15 found between σ and hex at very high conformational asymmetry.[28,30,125]

In the second effect, conformational asymmetry makes the micelle core much softer (i.e. easier to deform) which, similarly, leads to faceting of the nominally spherical micelle interface.[32,50,127,128] To understand this effect, consider a micelle confined to its Wigner-Seitz cell. To uniformly fill space, corona blocks must stretch to reach the edges and vertices of the micelle's polyhedral Wigner-Seitz cell. The stretched corona block is able to partially relax by pulling on and deforming the interface, which requires the core blocks to stretch. This deformation leads to a net entropic gain due to the lower stretching penalty in the core, but incurs an enthalpic penalty associated with higher interfacial area. As this faceting becomes more pronounced, the local geometry of the

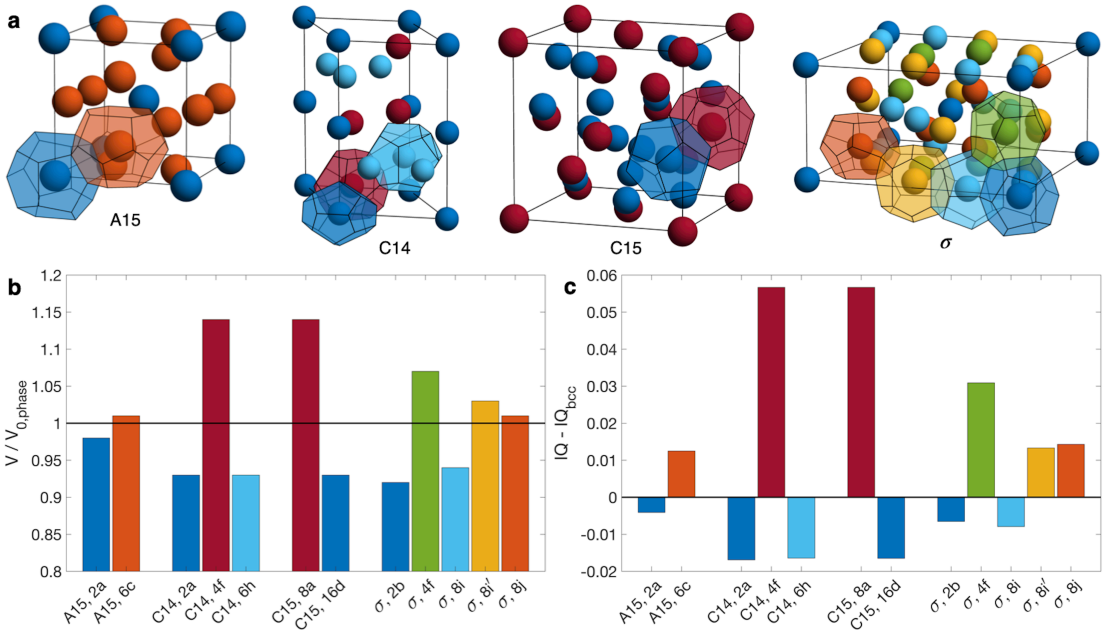

Figure 5.1: (a) Illustration of the Frank-Kasper σ, A15, C14, and C15 phases, highlighting the symmetry-inequivalent particle positions and associated Wigner-Seitz cells. (b) Volume of each particle type relative to the number-averaged particle volume for the structure, $V_{0,\text{phase}}$. (c) Isoperimetric quotient $\text{IQ} = 36\pi \text{V}^2/\text{S}^3$ of each particle type as reported by Kim et al.,[33] relative to that of bcc, where V is the particle volume and S is the particle surface area. Bar colors in (b) and (c) match the colors of the corresponding particles in (a). Particles are labeled in (b) and (c) according to phase and Wyckoff position. Structures in (a) are generated using a Matlab program developed by Lindsay et al.[126] Figure reproduced from Ref. 120.

Wigner-Seitz cell onto which the interface is imprinting becomes more thermodynamically relevant with more spherical Wigner-Seitz polyhedra creating less interfacial area relative to the micelle volume. Frank-Kasper phases are proposed to emerge in the neat diblock as a result of this faceting since they contain more spherical Wigner-Seitz polyhedra than the simpler fcc or bcc packings.[128]

The centrality of conformational asymmetry to the emergence of Frank-Kasper phases is, on the one hand, well established.[28,30–32,50,125,127,128] Sphericity theory, on the other hand, remains a working hypothesis. As stated in Chapter 1, Frank-Kasper phases are highly complex and contain multiple particle types, and each of these particle types possesses a unique volume (Fig. 5.1b) and sphericity (Fig. 5.1c). The central

argument that Frank-Kasper phases emerge because they have "more spherical" Wigner-Seitz cells relies on aggregate measures of particle sphericity in the neat diblock melt because such a melt has but a single conformational asymmetry parameter, ϵ_{AB}, which will impact all particles in the system. To more deeply probe sphericity theory and the impact of conformational asymmetry, it is desirable to independently manipulate the conformational asymmetry in each particle. One system which could offer such control, and the one chosen for the present work, is that of the diblock copolymer alloy.

Recently, Magruder et al.[129] used SCFT to predict the emergence of Laves phases with a diblock alloying methodology. They considered two conformationally symmetric sphere-forming diblocks, AB and B′C where the B and B′ blocks differ in degree of polymerization, with highly immiscible core blocks, A and C, which form distinct A-core and C-core micelles.[129] Blending of these diblocks, and the hypothesized "alloy" structure that results, is illustrated in Fig. 5.2. The segregation of chains into two distinct micelle types grants independent control of the properties of those micelles through the respective diblocks. In their work, Magruder et al.[129] controlled the asymmetry in micelle volumes by varying the degree of polymerization of the B′C chain. They found that proper selection of $N_{\mathrm{B'C}}$ stabilizes the Frank-Kasper Laves phases on a very narrow blend fraction range, producing what is effectively a non-ideal line compound (a phase field) on a eutectic phase diagram.[129] This prior work leveraged the independent control of the degree of polymerization enabled by the alloy system, but the methodology would also enable independent control of conformational asymmetry in the micelles. Such an approach has the potential to provide new insights into the role of conformational asymmetry in phase selection and act as a new lever with which to tune the phase behavior of block copolymers.

For our goal of probing sphericity theory and the role of conformation asymmetry, the Frank-Kasper Laves phases represent excellent target structures. Laves phases are the largest subset of the Frank-Kasper phases, with a unique AB_2 particle stoichiometry of smaller Z_{12} B particles and larger Z_{16} A particles.[35] In metal alloys, these structures most often appear as line compounds in binary systems with high atomic volume asymmetry (roughly $V_A/V_B = 1.2$) such as $MgZn_2$ (C14) or $MgCu_2$ (C15).[130] Both of these structures are illustrated in Figure 5.1a. As shown in Fig. 5.1c, the two particles in Laves structures are estimated to have substantially differing sphericities, with small particles

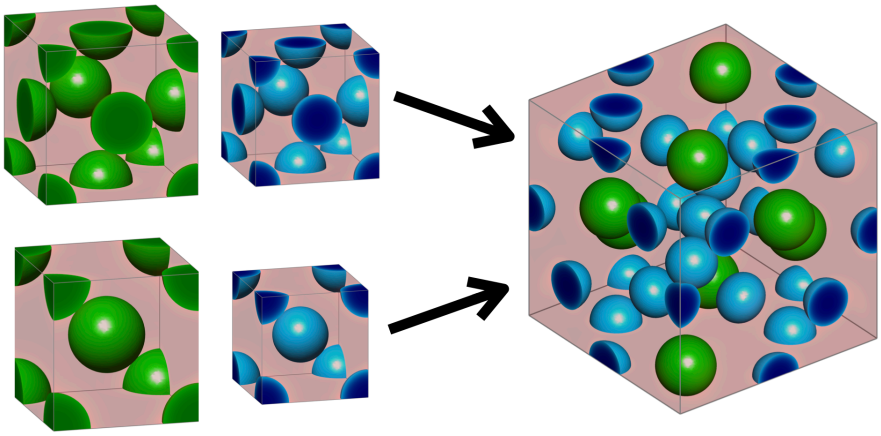

Figure 5.2: A simple schematic of the diblock alloying process in which diblocks with highly immiscible core blocks, which would form simple fcc or bcc sphere phases in the neat melt, are blended to form an "alloy" with A-core and C-core micelles in different particle positions of a C15 Laves Phase.

less spherical than bcc and large particles much more spherical than bcc.[128] Isolating conformational asymmetry effects to the two particle types in the Laves phases, each with opposite sphericity in comparison to bcc, creates an ideal test case for probing the role of a tunable conformational asymmetry.

In addition to having favorable particle properties for this study, the Laves phases represent an interesting test case because, in comparison to σ and A15, the Laves phases are a more difficult set of structures to stabilize in block polymers, requiring more elaborate approaches to produce them. In an equilibrium neat diblock melt, even at high conformational asymmetry, the chain stretching required to produce large volume asymmetry between particles makes Laves phases metastable, with the less asymmetric A15 and σ forming instead.[28,30,33,49,125] In a neat diblock melt, thermal processing is the only method found to produce Laves phases.[33,40,49,131] In this case, a deep quench from disorder kinetically traps a non-equilibrium distribution of micelle volumes such that Laves phases may form.[33,40,49,131] Stable Laves phases have been identified in diblock/homopolymer blends, where homopolymer localization in particle cores relieves packing frustration to enable the Laves volume asymmetry,[42,46–48] as well as in diblock blends, where differing length of the core blocks enables the volume asymmetry.[43,44,132] The most recent prediction of Laves phase emergence was that by Magruder et al.[129]

described in the last paragraph. The difficulty of stabilizing Laves phases makes the structures a more stringent test of the effectiveness of the conformationally asymmetric alloying approach.

5.2 Methods

5.2.1 System Specifications

Since our focus here is on the effect of conformational asymmetry on the formation of complex sphere phases (the Laves phases), we constrain our analysis to compositionally asymmetric diblocks with each polymer in our AB/B′C alloy having a minority volume fraction $f_A = f_C = 0.20$. We simplify our analysis by assuming symmetric segregation strengths for the individual diblocks in our system such that $\chi_{AB}N_{AB} = \chi_{BC}N_{B'C} = \chi N$, where the Flory-Huggins parameter, χ_{AB} or χ_{BC}, for each chain is scaled according to its associated polymer's total degree of polymerization, N_{AB} or $N_{B'C}$ respectively. Achieving an alloy-style blending behavior requires that the core blocks, A and C, are highly immiscible. If the interaction between these blocks were weaker than the core-corona interactions, it could lead to the formation of mixed-core micelles. We instead choose to enhance the immiscibility of the A and C monomers relative core-corona interactions by setting $\chi_{AC}N_{AB} = 2(\chi N)$. When reporting results, particularly for phase diagrams, it is convenient to express these segregation strengths in terms of temperature as well. To achieve this, we assume purely enthalpic contributions to χ and choose a reference temperature T_0 corresponding to $\chi N = 30$.

As stated in the introduction to this chapter, we are focusing our study on the Frank-Kasper Laves phases. Among the three most common Laves phases (C14, C15, and C36),[130] we consider only C14 and C15 because they are generally expected to be stable compared to C36,[133] and are the only Laves phases observed in block polymer systems.[33,40,42,49,131,132,134] We find that C14 is the more stable of the two within their stability window, and thus choose it as the relevant target when analyzing our results. However, we find that the Laves phases are nearly degenerate in this system (see Fig. 5.7), which is consistent with prior literature,[33,49,88,129,133] and thus selection of C14 over C15 for our analysis is inconsequential. Prior studies of these AB/B′C alloys find that large portions of the phase diagram are regions of macrophase separation

involving the AB-rich and B′C-rich bcc spheres.[129] We anticipate a similar behavior in this study, and at all points compare our Laves phase energies to macrophase separation. For this macrophase separation reference, we consider three classical candidate phases: face-centered cubic spheres (fcc), body-centered cubic spheres (bcc), and hexagonally-packed cylinders (hex), each with both AB-rich and B′C-rich varieties.

5.2.2 SCFT Details

As with all other work in this dissertation, our analysis here uses SCFT[135,136] with a Gaussian chain model.[55,57,135] Our calculations are performed with the C++ version of the PSCF code described in Section 2.3 using both the canonical and grand canonical ensembles.[58,68,137] All calculations are converged to a tolerance of 1×10^{-6} using the relative residual norm described by Matsen[65] and use a contour length step size $\Delta s = 0.01$. SCFT iterations use Anderson Mixing[64–66] with simultaneous optimization of unit-cell parameters[66,67] to ensure accurate free energies. Methods to compute phase equilibria and phase boundaries are described in Appendix A.1.

5.3 Results and Discussion

5.3.1 Effects of Conformational Asymmetry

Our objective is to understand how conformational asymmetry affects the stability of Laves phases. However, we also want to ensure that the alloy is able to accommodate the particle volume asymmetry found in the Laves phases, so that the phases are not artificially destabilized by inappropriate micelle volumes. To this end, we start our analysis by varying conformational asymmetry at a range of chain length asymmetries, $0.5 \leq N_{\mathrm{B'C}}/N_{\mathrm{AB}} \leq 2.0$, which will allow chain length asymmetry to serve as a counter-balance to any micelle-volume effects brought about by changes to conformational asymmetry. Our calculations consider conformational asymmetries of 1.00, 1.25, and 1.50 applied to (i) the AB diblock, (ii) the B′C diblock, and (iii) both the AB and B′C diblocks simultaneously. For each of these conditions, we performed canonical SCFT simulations of the C14 and C15 Laves phases and compared their free energies per chain of size N_{AB} (denoted by $F/nk_{\mathrm{B}}T$) against potential macrophase separation

via the common tangent construction.[138] At each condition, the common tangent representing macrophase separation for comparison to the Laves phases was taken to be the lowest-energy tangent among those formed by each (AB-rich, B′C-rich) macrophase-separation-candidate phase pairing. The analysis was performed at two segregation strengths, $\chi N = 25$ and $\chi N = 28$, chosen based on the neat diblock phase diagrams[139] such that a neat diblock melt with block fraction $f_i = 0.2$ and conformational asymmetry of $\epsilon_{ij} = 1.0$ or $\epsilon_{ij} = 1.5$, respectively, would be approximately centered in the bcc window.

Figures 5.3 and 5.4 depict the lowest energy of the C14 Laves phase relative to macrophase separation at each of the conditions described above at $\chi N = 28$ and $\chi N = 25$, respectively. At $\chi N = 28$, the macrophase separation reference is dominated by coexistence of AB-rich and B′C-rich bcc morphologies; the only exceptions occur when B′C-rich fcc overtakes B′C-rich bcc at the highest conformational asymmetry condition ($\epsilon_{ij} = 1.5$) for very low $N_{\mathrm{B'C}}/N_{\mathrm{AB}}$. On the other hand, at $\chi N = 25$ both fcc and bcc appear frequently on both ends of the macrophase separation tangent, with fcc more frequent at higher conformational asymmetries. The emergence of these fcc phases on the macrophase separation tangent is indicated on Figs. 5.3 and 5.4 by the shaded regions.

The data in Figs. 5.3 and 5.4 demonstrate the distinct effects of each conformational asymmetry on both the stability of the Laves phases and the chain length asymmetry most favorable to their formation. Increasing the conformational asymmetry of the AB diblock (Figs. 5.3a and 5.4a) generally destabilizes Laves phases while shifting the minima of the F vs $N_{\mathrm{B'C}}/N_{\mathrm{AB}}$ toward higher chain length asymmetry. If instead ϵ_{BC} is increased (Figs. 5.3b and 5.4b), the opposite effect is observed with the Laves phases becoming more stable with increasing conformational asymmetry and the minima of F vs $N_{\mathrm{B'C}}/N_{\mathrm{AB}}$ shifting to lower $N_{\mathrm{B'C}}/N_{\mathrm{AB}}$. Simultaneously increasing both ϵ_{AB} and ϵ_{BC} (Figs. 5.3c and 5.4c) leads to competition between these two opposing trends, resulting in only minimal changes to F vs $N_{\mathrm{B'C}}/N_{\mathrm{AB}}$.

The stabilizing effect of ϵ_{BC} and the destabilizing effect of ϵ_{AB} both can be attributed to the softening of micelle cores and the resultant imprinting on the polyhedral Wigner-Seitz cell.[32,50,127,128,140,141] As conformational asymmetry increases, faceting of the micelle core creates more interfacial area, but the thermodynamic cost, relative to

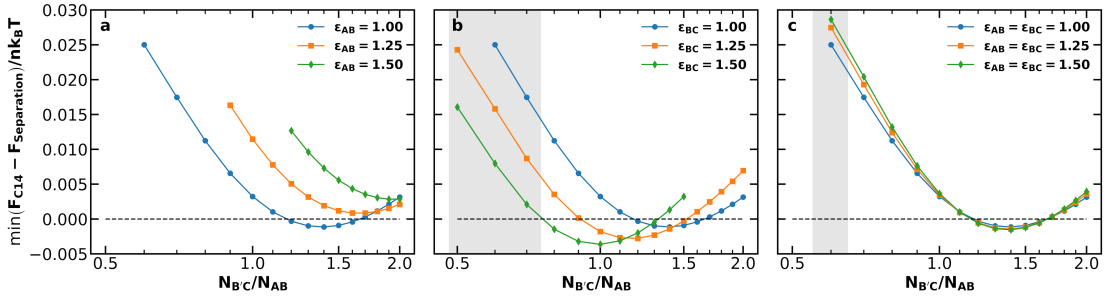

Figure 5.3: Minimum free energy of the C14 Laves phase relative to the macrophase separation tangent line versus logarithmically-scaled chain length asymmetry at various conformational asymmetries for (a) the AB diblock, (b) the B′C diblock, or (c) both the AB and B′C diblocks for $\chi_{AB}N_{AB} = \chi_{BC}N_{B'C} = 28.0$, $\chi_{AC}N_{AB} = 56.0$, and $f_A = f_C = 0.20$. Shaded regions indicate those in which B′C-rich fcc is used in the macrophase separation tangent, rather than B′C-rich bcc, which only correspond to $\epsilon_{BC} = 1.5$ in (b) or $\epsilon_{AB} = \epsilon_{BC} = 1.5$ in (c). Figure modified from Ref. 120.

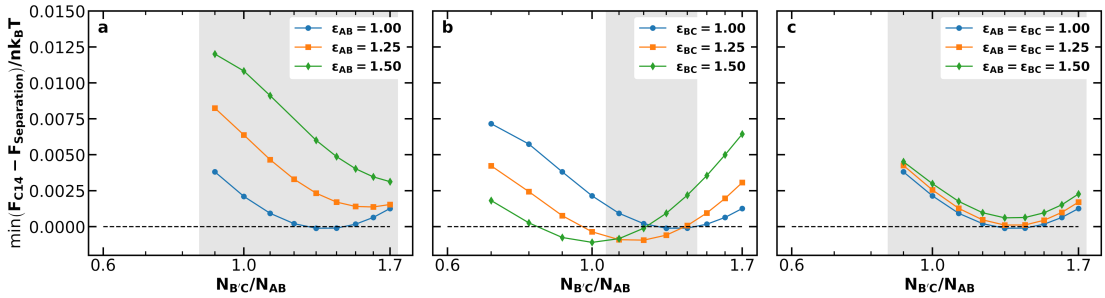

Figure 5.4: Minimum free energy of the C14 Laves phase relative to the macrophase separation tangent line versus logarithmically-scaled chain length asymmetry at various conformational asymmetries for (a) the AB diblock, (b) the B′C diblock, or (c) both the AB and B′C diblocks for $\chi_{AB}N_{AB} = \chi_{BC}N_{B'C} = 25.0$, $\chi_{AC}N_{AB} = 50.0$, and $f_A = f_C = 0.20$. Shaded regions indicate those in which one or both of the AB-rich and B′C-rich fcc phases are used in the macrophase separation tangent (in place of the corresponding bcc phase) at one or more of the conformational asymmetries studied here. Figure modified from Ref. 120.

micelle volume, is lower for more spherical polyhedra.[31,32,128] In neat diblock systems, Frank-Kasper phases are proposed to form at higher conformational asymmetry because their particles are, on average, more spherical than in bcc.[33,128] Critically, however, this does not mean that all Wigner-Seitz polyhedra in a Frank-Kasper phase are more spherical than those in bcc,[33] as shown in Fig. 5.1c. Rather, the thermodynamic benefits of the polyhedra that are more spherical (the red Laves phase particles in Fig. 5.1) tend to outweigh the costs of those that are less spherical. In the Laves phases, the smaller

micelles (AB) reside in domains that are less spherical than bcc, while the larger micelles (B′C) are in more spherical domains.[33] Therefore, when increasing ϵ_{AB}, there is a thermodynamic cost (relative to bcc formation) incurred by deforming the small micelle cores without the larger domains as a counter-balance; likewise, increasing ϵ_{BC} creates a relative thermodynamic benefit without the opposing cost of the smaller micelles.

The observed shifts in the locations of the F vs $N_{B'C}/N_{AB}$ minima result from the effects of conformational asymmetry on the radius of gyration of a diblock copolymer. Increasing ϵ_{ij} at fixed N increases the micelle volume. When increasing ϵ_{AB}, this swelling applies to the smaller particles in the Laves structure. Such changes reduce the volume asymmetry, making the Laves structure less stable. Increasing the chain length asymmetry compensates somewhat for the unfavorable swelling of AB micelles, resulting in the rightward shift of the curves. The reverse holds true for B′C: increasing ϵ_{BC} swells the larger particles for a given value of N, thus promoting excess volume asymmetry and demanding reduced length asymmetry in response to stabilize the Laves phase. In fact, the swelling induced by $\epsilon_{BC} = 1.50$ is sufficient on its own to produce the requisite Laves volume asymmetry, with the observed minimum occurring at $N_{B'C}/N_{AB} = 1.0$.

Neither of these trends are evident in Figs. 5.3c and 5.4c, in which ϵ_{BC} and ϵ_{AB} are increased together. Instead, simultaneous changes to both conformational asymmetries obscure the competing effects described above, resulting in minimal changes to the free-energy curve. This condition is analogous to the single conformational asymmetry available in neat diblock melts obscuring the individual particle effects, and highlights the value of leveraging multiple conformational asymmetries. For both values of χN, the Laves phases had their lowest relative free energy when $\epsilon_{BC} = 1.5$ and $N_{B'C}/N_{AB} = 1.0$, so this condition was selected for further analysis.

5.3.2 Evaluating A Simple Model to Predict Laves Phase Emergence

It would be useful to have some model with which to predict the optimal conditions for emergence of Laves phases in this type of alloy system. In this section, we introduce a simple model for this task and evaluate its accuracy in light of the results presented in Section 5.3.1. Stabilization of a Laves phase in this alloy system requires that (i) the AB and B′C polymers form micelles with appropriate volume asymmetry $\alpha = V_{B'C}/V_{AB}$ and (ii) the chains are blended at a ratio which yields a particle stoichiometry

of approximately 2:1.[129] If we choose the B′C diblock to form the larger micelles (the red particles in Fig. 5.1), the expected blend fraction for Laves phase formation is

$$\phi_{\mathrm{AB}} = 1 - \phi_{\mathrm{B'C}} = \frac{2}{2+\alpha} \tag{5.1}$$

as in prior work.[129] The preferred micelle radius for the AB diblock scales as its radius of gyration $R_{g,\mathrm{AB}}$, and similarly for the B′C diblock, so the volume asymmetry can be written as $\alpha = (R^3_{g,\mathrm{B'C}}/R^3_{g,\mathrm{AB}})$. Using the unperturbed radius of gyration as a starting point for the particle size and Gaussian statistics, then $R_{g,\mathrm{AB}}$ is given by $R^2_{g,\mathrm{AB}} = R^2_{g,\mathrm{A}} + R^2_{g,\mathrm{B}}$, and similarly for $R_{g,\mathrm{B'C}}$. The corresponding Laves phase volume asymmetry for a given set of AB and B′C chains is then

$$\alpha = \left(\frac{N_{\mathrm{B'C}}}{N_{\mathrm{AB}}}\right)^{3/2} \left[\frac{1 + f_{\mathrm{C}}\left(\epsilon^2_{\mathrm{BC}} - 1\right)}{1 + f_{\mathrm{A}}\left(\epsilon^2_{\mathrm{AB}} - 1\right)}\right]^{3/2} \tag{5.2}$$

where we have grouped the terms to highlight the separate contributions of the chain lengths in the first term, and the statistical segment lengths in the second term. Note that when all monomers have the same statistical segment lengths (i.e., $\epsilon_{\mathrm{AB}} = \epsilon_{\mathrm{BC}} = 1.0$), Equation 5.2 reduces to the result obtained previously for conformationally symmetric alloys.[129]

Figure 5.5 compares the optimum $N_{\mathrm{B'C}}/N_{\mathrm{AB}}$ at $\chi N = 25$ and $\chi N = 28$ from our SCFT results against values predicted by Eq. 5.2 with varying conformational asymmetry. Predicting $N_{\mathrm{B'C}}/N_{\mathrm{AB}}$ from Eq. 5.2 requires a volume asymmetry α to use as a basis. For this basis, $\alpha = 1.48$ is a good choice because the same value has appeared in prior work as (i) the best volume asymmetry observed from SCFT in conformationally symmetric diblock alloys,[129] and (ii) the optimum volume asymmetry for Laves phases obtained from the unconstrained diblock foam model.[128] Figure 5.5 reveals two shortcomings in this estimate. First, the model fails to capture the effects of χN, consistently underestimating the chain length asymmetry for $\chi N = 28$. Second, the model significantly underestimates the impact of ϵ_{AB}. However, when varying ϵ_{BC}, the model shows reasonable agreement with the observed value. Overall, the simple model of Eq. 5.2 captures the $\chi N = 25$ behavior in panels b and c of Fig. 5.5, but fails to capture the effects of segregation strength or accurately reflect the behavior in Fig. 5.5a.

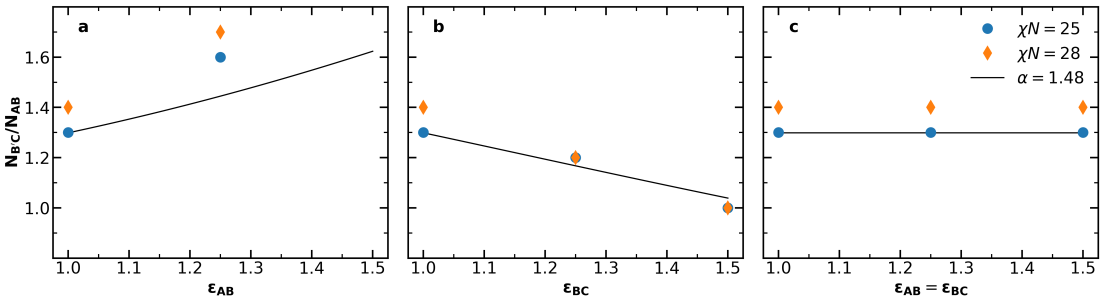

Figure 5.5: The chain length asymmetry $N_{\mathrm{B'C}}/N_{\mathrm{AB}}$ at the F vs. $N_{\mathrm{B'C}}/N_{\mathrm{AB}}$ minima at $\chi N = 25$ (Fig. 5.4) and $\chi N = 28$ (Fig. 5.3), compared to the chain length asymmetry predicted by Equation 5.2 for $\alpha = 1.48$ when (a) ϵ_{AB} is varied, (b) ϵ_{BC} is varied, and (c) ϵ_{AB} and ϵ_{BC} are varied together. In (a), no minimum could be clearly observed for $\epsilon_{\mathrm{AB}} = 1.5$, as the lowest observed free energy occurred at $N_{\mathrm{B'C}}/N_{\mathrm{AB}} = 2.0$, which was the highest value considered. Figure reproduced from Ref. 120.

5.3.3 Phase Diagram for a Conformationally Asymmetric Alloy

We now continue our investigation with a thorough analysis of the phase behavior of the diblock alloy system with $N_{\mathrm{B'C}}/N_{\mathrm{AB}} = 1.0$, $\epsilon_{\mathrm{AB}} = 1.0$, and $\epsilon_{\mathrm{BC}} = 1.5$, found to most effectively stabilize the Laves phases amongst all of the systems we studied. To generate the phase diagram in Fig. 5.6, most phase boundaries were established first using the common-tangent construction[138] and canonical ensemble SCFT calculations. In addition to the C14, C15, fcc, bcc, and hex phases already described, 15 additional competitors were included in these calculations. The competing phases are inspired by a 2014 study of $\mathrm{B_1AB_2CB_3}$ multiblock terpolymers by Xie et al.[125] and are identical to those chosen by Magruder et al.[129] for their block polymer alloys study. A list of all phases considered in the calculations is included in Table A.1. Subsequent grand canonical calculations were used to resolve the region near each invariant point, where grand canonical ensemble's higher accuracy for problems involving macrophase separation[137] substantially benefits the identification of the three-phase coexistence at these points. Grand canonical calculations were also used to map the phase boundaries near the ODT, where both canonical SCFT calculations and common tangent calculations started to suffer from failed convergence. C14 was used to represent the Laves phases while mapping the phase diagram. Methodologies to compute phase equilibria are detailed in Appendix A.1.

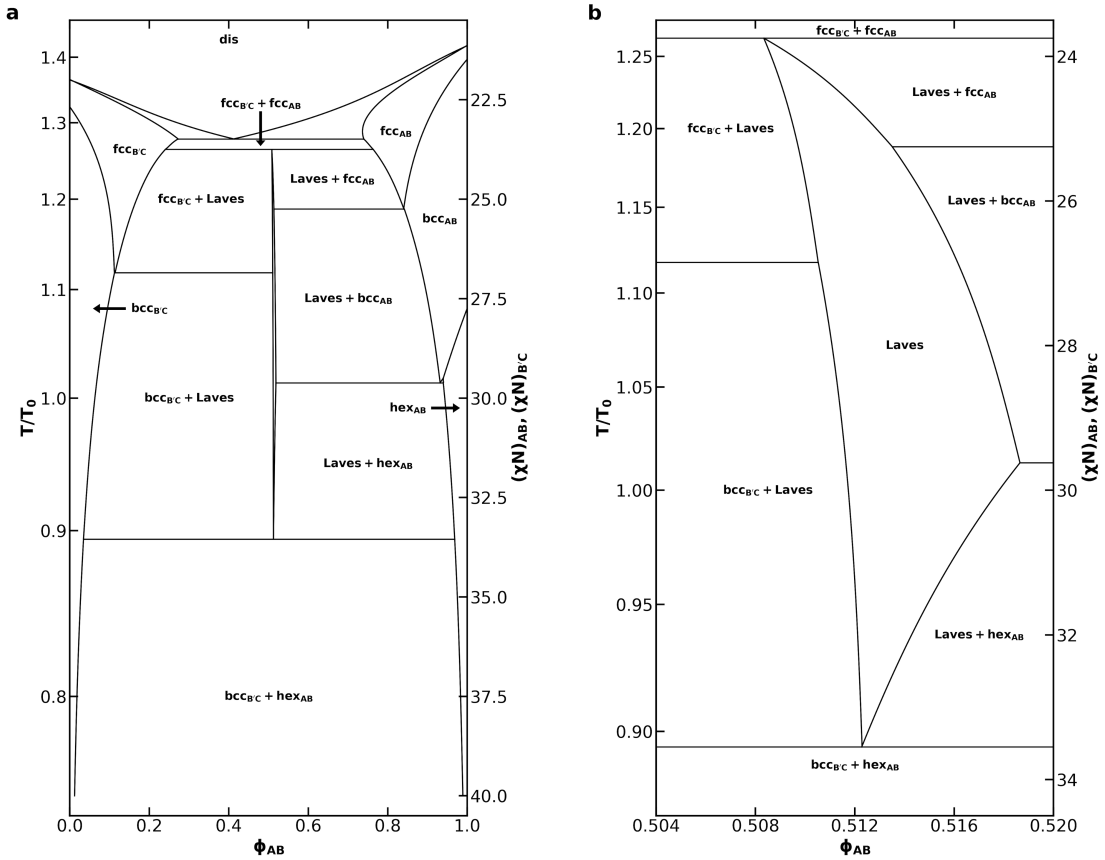

Figure 5.6: (a) Phase diagram for an AB/B′C alloy with $N_{\mathrm{B'C}}/N_{\mathrm{AB}} = 1.0$, $f_{\mathrm{A}} = f_{\mathrm{C}} = 0.20$, $\epsilon_{\mathrm{AB}} = 1.0$, $\epsilon_{\mathrm{BC}} = 1.5$, and assuming purely enthalpic χ values such that $\chi_{\mathrm{AC}} N_{\mathrm{AB}} = 2\,(\chi N)$ at all T and (b) a detailed view of the Laves phase field within that phase diagram. The reference temperature, T_0, was chosen to correspond to $\chi N = 30$. Non-linear segments of the phase diagram are drawn using cubic splines fit to the sampled data. Figure reproduced from Ref. 120. A complementary phase diagram indicating all points at which data were collected is available in Appendix A, Fig. A.2.

The phase diagram in Fig. 5.6a bears substantial qualitative resemblance to that presented by Magruder et al. for the conformationally symmetric case,[129] with many characteristics reminiscent of metal alloy phase diagrams. In each case, the diblock alloys display a eutectic transition from a disordered liquid to coexistence between AB-rich and B′C-rich fcc phases, as well as a peritectoid transition to a Laves phase field upon cooling from coexistence of simple sphere phases (fcc or bcc). In the conformationally

asymmetric case, however, the temperature difference between the eutectic and peritectoid points is greatly reduced when compared to prior results for a conformationally symmetric system.[129] The peritectoid transitions of the two systems also differ on which simple sphere phase overtakes the Laves phase: bcc in the conformationally symmetric case,[129] and fcc here. As also noted by Magruder et al.,[129] experimental realization of this narrow eutectic to peritectoid transition is unlikely, given that fluctuation effects are expected to destroy the high-temperature regions of the diagram.

Below the peritectoid point, the Laves phase field widens as temperature decreases, and Laves coexistence with AB-rich and B′C-rich fcc phases is overtaken by coexistence with the corresponding bcc phases. At $\chi N = 28$, the highest segregation strength tested by Magruder et al.,[129] we find a Laves phase field with a width of 0.006 in ϕ_{AB}. This exceeds the 0.002 width in ϕ_{AB} reported previously,[129] consistent with the expectation that conformational asymmetry stabilizes Laves phases in the blend, while still possessing the narrow width characteristic of a phase field. The phase field reaches a maximum width at $\chi N = 29.62$ where the AB-rich bcc field closes, and the Laves phase starts to coexist with the AB-rich hex phase. At this segregation strength, the AB diblock would naturally form a hex phase in the neat melt. As the system is cooled further, conversion of the cylinder-forming AB diblock into spheres becomes increasingly unfavorable. The Laves phase field thus closes in a eutectoid transition to coexistence of B′C-rich bcc and AB-rich hex, which dominates the phase diagram at lower temperatures. The shape of the Laves phase field is difficult to resolve in Fig. 5.6a, so we include Fig. 5.6b to focus on the Laves window and help illuminate these details. Appendix A also contains a complementary phase diagram (Fig. A.2) which shows all points at which SCFT data were collected, if the reader wishes to verify that drawn phase boundaries faithfully reflect the underlying data.

We claim in Section 5.2 that C14 was chosen to represent Laves phases in this work because it is more stable than C15. We also claim that near-degeneracy of the two morphologies suggests little would change in the analysis were C15 used instead. To justify these claims, Fig. 5.7 shows the energy of C15 relative to C14 according to canonical ensemble data used to generate Fig. 5.6. We see that within the blend fraction range containing the Laves phase field (between the vertical dotted lines in Fig. 5.7), C14 is indeed more stable than C15. We also see that their free energies

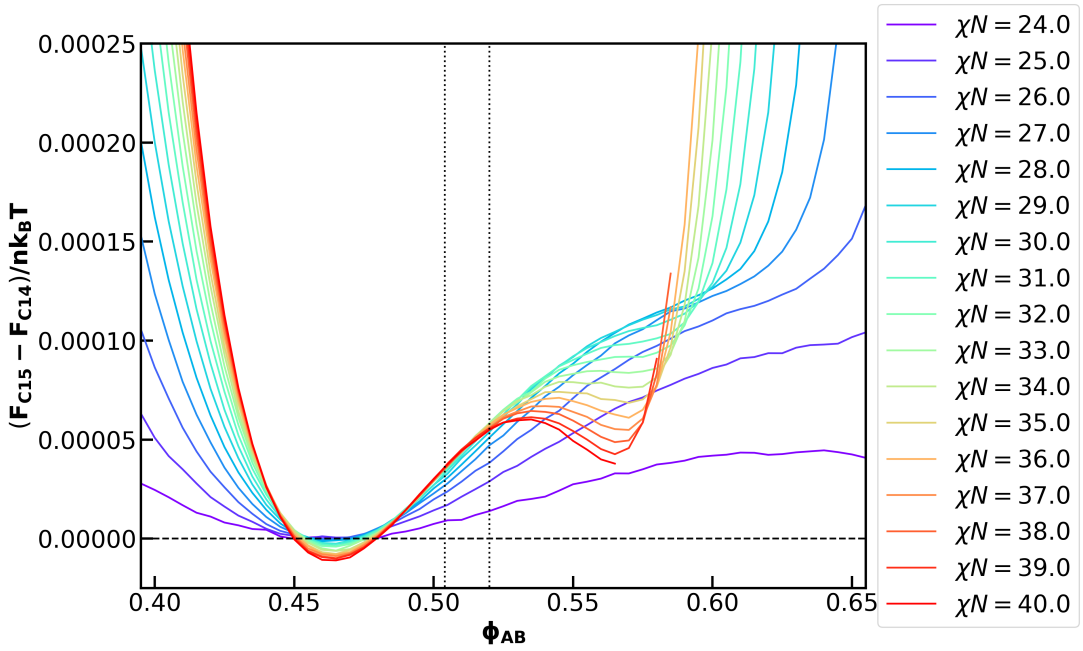

Figure 5.7: The energy of the C15 Laves phase relative to that of C14 from canonical ensemble SCFT data in units of k_BT per chain of length N_{AB} used to generate the phase diagram in Fig. 5.6. The vertical dotted lines represent the bounds (in ϕ_{AB}) of Fig. 5.6b, and serve as a guide for the range relevant to the Laves phase field reported in this work. Figure reproduced from Ref. 120.

differ by less than 1×10^{-4} k_BT per chain of length N_{AB}, indicating near-degeneracy of the structures. Interestingly, this data does indicate that C15 is more stable than C14 over a narrow composition window. However, this occurs at blend fractions where both Laves structures are metastable relative to macrophase separation and thus does not impact our analytical approach.

5.3.4 Phase Field Extension to High Segregation Strength

The difference in conformational asymmetry of the two diblocks results in substantial asymmetries in the phase diagram, particularly with regard to AB-rich and B′C-rich phase transitions. Conformational asymmetry shifts the phase boundaries of the neat B′C diblock relative to that of the AB diblock.[26,31,121,124,139,142] These morphological differences between the neat diblock melts carry over into the blended behavior, resulting in the asymmetries observed in Fig. 5.6. Of particular interest is the absence of any

B′C-rich hex formation. The presence of hex on the AB-rich side of the diagram results in a transition from a gradually broadening Laves phase field to a rapidly narrowing one.

The narrowing of the Laves phase field at the AB-rich bcc-hex transition suggests that, without competition from hex phases, conformationally asymmetric binary diblock alloys may exhibit a Laves phase field out to strong segregation. In order to test this speculation, we need to select a system in which neither diblock undergoes a transition to hex in the neat melt. From Fig. 5.3c, we see that when both diblocks have a conformational asymmetry of 1.5, the Laves phase remains stable when the ratio of the degrees of polymerization is used to induce volume asymmetry. We also know that a neat diblock with $\epsilon = 1.5$ and $f = 0.2$ will not assemble into hex below $\chi N = 40$,[139] which is an approximate upper bound for the ability to converge Frank-Kasper phase SCFT calculations with our software. Thus, we choose to further analyze an alloy system where $\epsilon_{\mathrm{AB}} = \epsilon_{\mathrm{BC}} = 1.5$ and $N_{\mathrm{B'C}}/N_{\mathrm{AB}} = 1.4$, which corresponds with the lowest relative free energy for Laves phases at the desired conformational asymmetry from our testing.

Using the same set of competing phases as for Fig. 5.6, the Laves phase field was mapped for this alloy. Canonical ensemble calculations were used in a common tangent analysis to identify the stable region for the Laves phase. As can be seen in Fig. 5.8, the Laves window remains open and continues to broaden up to $\chi N = 40$. The Laves window also shifts to lower ϕ_{AB} upon cooling, consistent with the trend seen in the work of Magruder et al. for conformationally symmetric alloys where $N_{\mathrm{B'C}}/N_{\mathrm{AB}}$ was also used to create distinct particle sizes.[129] It is also interesting to note that at the low-temperature end of Fig. 5.8, the AB-rich (right) side of the Laves window is much more nearly vertical than on the B′C-rich (left) side. Diblocks with the same block fraction and conformational asymmetry should exhibit the same phase behavior in the neat-melt limit; one might expect this symmetry to carry into the blending behavior and, likewise, into the Laves coexistence boundaries. However, both the deflection of the Laves window to lower ϕ_{AB} and the differing verticality of the coexistence boundaries demonstrate that this is not the case. This difference results from the asymmetry in chain length between the AB and B′C diblocks and resultant differences in their ability to pack in the interstitial sites of the bcc phases.

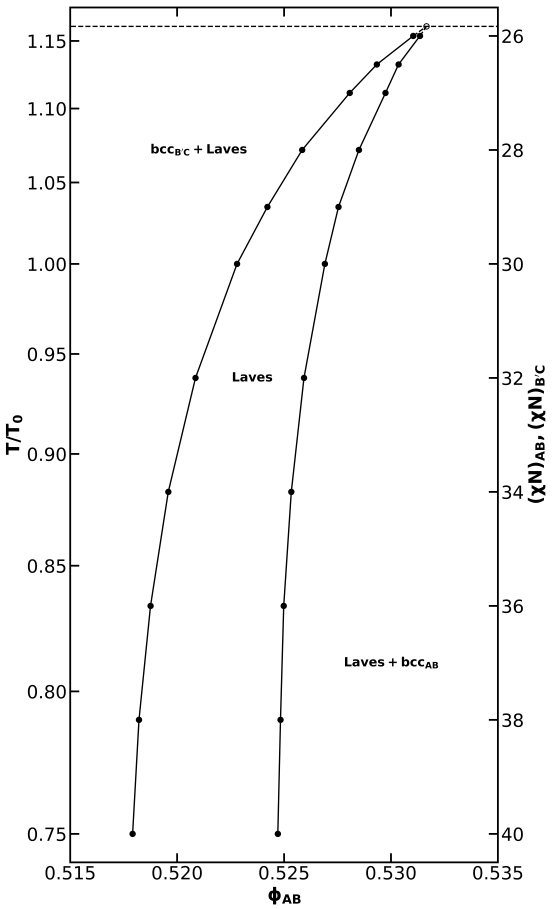

Figure 5.8: The Laves phase window for $N_{\mathrm{B}'\mathrm{C}}/N_{\mathrm{AB}} = 1.4$, $f_{\mathrm{A}} = f_{\mathrm{C}} = 0.20$, $\epsilon_{\mathrm{AB}} = \epsilon_{\mathrm{BC}} = 1.5$, and assuming purely enthalpic χ values such that $\chi_{\mathrm{AC}} N_{\mathrm{AB}} = 2\,(\chi N)$. The reference temperature T_0 was chosen to correspond to $\chi N = 30$. A peritectoid point and its associated tie line are included as a guide for the eye, but the position is interpolated from common-tangent data at $\chi N = 25.5$ and $\chi N = 26$, and are therefore marked with a dashed line and open data marker to reflect the imprecision of this estimate. Figure reproduced from Ref. 120.

5.4 Conclusion

Using the Frank-Kasper Laves phases as a case study, we have demonstrated the ability of block polymer alloys to decouple the potentially competing effects of conformational asymmetry in different particle types, thereby probing the subtleties of its role in phase selection. In Laves phases, this decoupling revealed that increasing conformational asymmetry in the smaller, less spherical Laves particles has a detrimental effect on Laves phase stability, while increasing it in the larger, more spherical micelles is beneficial. The absence of significant changes to Laves stability when conformational asymmetry is simultaneously increased in both particles highlights how information can be obscured by competition when only a single conformational asymmetry is available – such as in a neat diblock melt.

Our results also demonstrate the value of independent conformational asymmetry control as a tool for designing self-assembling block polymer systems. Not only do we find that increasing conformational asymmetry in the large particles stabilizes the Laves phases, we also find that this effect is sufficient to produce the volume asymmetry required for Laves phase formation, without the need for asymmetry in the degrees of polymerization of the constituent chains, and results in a lower relative free energy for the Laves phases than was seen in the conformationally symmetric case. The phase diagram of this system bears a striking resemblance to that reported for the conformationally symmetric case,[129] with a slightly broader Laves window and a greater variety of phases coexisting with the Laves phase. With increasing segregation strength, increasing preference for cylinder formation by one of the diblocks causes cylinders to rapidly out-compete the Laves phases, thus closing the Laves phase field. We are further able to leverage conformational asymmetry to avoid this cylinder formation and stabilize the Laves phases out to high segregation strength, suggesting the potential to extend the Laves phase field out to the strong segregation limit by balancing chain composition, degrees of polymerization, and conformational asymmetries.

Chapter 6

Frank-Kasper phase formation in AB/A′B′ blends

6.1 Introduction

In Chapter 5 we briefly mentioned the predicted emergence of Laves phases in AB/A′B′ blends of diblock copolymers with distinct core block lengths. Here, we revisit this topic to consider more broadly the emergence of Frank-Kasper phases in binary AB/A′B′ blends, in which the two chains contain blocks of identical chemistries but different block fractions and chain lengths, as indicated by the prime notation. SCFT calculations by Liu et al. predicted that a binary blend of diblock polymers AB and A′B with equal corona block lengths, $N_{B,1} = N_{B,2} = N_{\mathrm{B}}$, and distinct core block lengths, $N_{A,1} \leq N_{A,2}$, stabilizes the FK σ and A15 phases.[44] This SCFT prediction was amended later, following the discovery of the C14 and C15 Laves phases,[33] when Kim et al. predicted the emergence of Laves phases (which had not been among the candidate phases considered in the prior study) over large portions of what had been the σ window.[49] Experiments using blends of diblock copolymers with unequal core block lengths have observed the ostensibly stable windows for the σ,[39,43,91,143,144] A15,[43,91,143,144] and C14[43] phases.

The current mechanistic understanding of this phenomenon, as proposed by Liu et al.[44], parallels, to some extent, the Chapter 5 discussion of conformational asymmetry's role in Frank-Kasper phase formation via sphericity theory. In particular, the proposed mechanism posits that a bidisperse core has two primary effects: (1) it promotes

deformability of the micelle cores and (2) it enables extension of the quasi-spherical micelle regime to higher core block volume fractions. For the matter of micelle core deformability, Liu et al.[44] predicted that the bidisperse core blocks segregate regionally on the micelle interface, with the smaller core blocks localized at regions of high interfacial curvature while the longer core blocks concentrate in regions of low interfacial curvature. In this way, the blend reduces the entropic penalty for deformation of the micelle interface compared to the neat melt. This enhanced core deformability, just as in the case of conformational asymmetry, acts to extend the particle-forming window to higher volume fractions of the micelle core. Simultaneously, the introduction of longer core blocks proportionally increases the core volume, driving the system toward the FK phase window near the deflected sphere-cylinder transition.

Subsequent work[43] has offered another mechanism for the emergence of FK phases in AB/A′B′ blends in systems where the smaller chain is highly compositionally asymmetric (disordered in the neat melt) and the larger chain is more compositionally symmetric (forming double-gyroid in the neat melt). In this work, Lindsay et al. predict transitions from C15 to the close-packed fcc and hcp phases to FK σ and A15 phases with decreasing blend fraction of the asymmetric copolymer.[43] This transition sequence cannot be explained by segregation along the micelle interface as described by Liu et al.[44] This sequence, and the Laves phase emergence in particular, also could not be explained by segregation of the different chains into bidisperse micelles (somewhat analogous to the alloys from Chapter 5) because (1) the highly asymmetric copolymer would be unable to form micelles on its own, and (2) SCFT data show the micelle cores in the C15 phase are all roughly the same volume despite high volume asymmetry between the particle sites. Instead, Lindsay et al. suggest that C15 is able to form because the asymmetric chain delocalizes from the micelle interface and collects in the matrix surrounding the large particle sites to relieve coronal packing frustration. The full transition sequence Lindsay et al. observe, in fact, corresponds with the volume of interstitial voids in the structures for nearly monodisperse micelle cores: C15 has very large interstitial voids which can accommodate large amounts of asymmetric polymer; fcc and hcp can accommodate moderate amounts of asymmetric copolymer in the matix; σ and A15 emerge when very little copolymer can or must localize in the interstices.[43]

Much attention has been paid to the role of core block asymmetry in Frank-Kasper

phase formation by systems of AB/A′B′ blends. Far less is known about the role of corona block asymmetry in FK phase formation. Experimental works have demonstrated the emergence of FK phases in systems with both asymmetric core and asymmetric corona blocks[39] indicating that corona block asymmetry does not preclude the formation of FK phases. However, Liu et al. predict with SCFT that a conformationally symmetric AB/A′B′ blend with core block asymmetry $(N_2/N_1)_{\text{core}} = 3$ would exhibit a narrowing and, eventually, closing σ phase window with increasing corona block asymmetry $(N_2/N_1)_{\text{corona}} > 1$,[44] suggesting that corona block asymmetry (or perhaps excessive overall chain length asymmetry) might disfavor FK phase formation.

As part of his thesis work,[144] Aaron Lindsay sought to address the question of corona block asymmetry's role in FK phase formation. In particular, he sought to establish design rules for binary diblock blends with potential to form FK phases, particularly as they relate to the relative degree of asymmetry needed in the core and corona blocks. Figure 6.1, based on a similar figure in Ref. 144, summarizes the results of this thesis work, as well as theoretical and experimental results from prior studies.[39,44,49,91,132,143,145] The figure shows the core block asymmetry $(N_2/N_1)_{\text{core}}$ and corona block asymmetry $(N_2/N_1)_{\text{corona}}$ of AB/A′B′-style blends, indicating (by color) whether FK phases were (blue) or were not (red) observed or predicted for the system. On the basis of these compiled results, Lindsay hypothesized that (1) stability of FK phases requires that $(N_2/N_1)_{\text{core}} > (N_2/N_1)_{\text{corona}}$ and (2) there exists some critical threshold chain length asymmetry (N_2/N_1) that is dependent on the polymer system, the core block asymmetry, and the corona block asymmetry which must be met to stabilize FK phases.[144] Here, we aim to computationally test these hypotheses over a wider range of the parameter space than the shaded regions of Fig. 6.1 using SCFT. In particular, we wish to determine how the range of corona block asymmetries in which FK phases may form is impacted by changes to core block asymmetry. On the basis of Lindsay's hypotheses, we expect that no FK phases will emerge below the $(N_2/N_1)_{\text{core}} = (N_2/N_1)_{\text{corona}}$ line and that the maximum $(N_2/N_1)_{\text{corona}}$ at which FK phases will emerge should vary with changes to $(N_2/N_1)_{\text{core}}$.

Ultimately, the results from this study were unable to be used for a publication due to a series of problems including methodological mistakes, and computational difficulties. Methodologically, the framing of the research question, and criterion chosen for

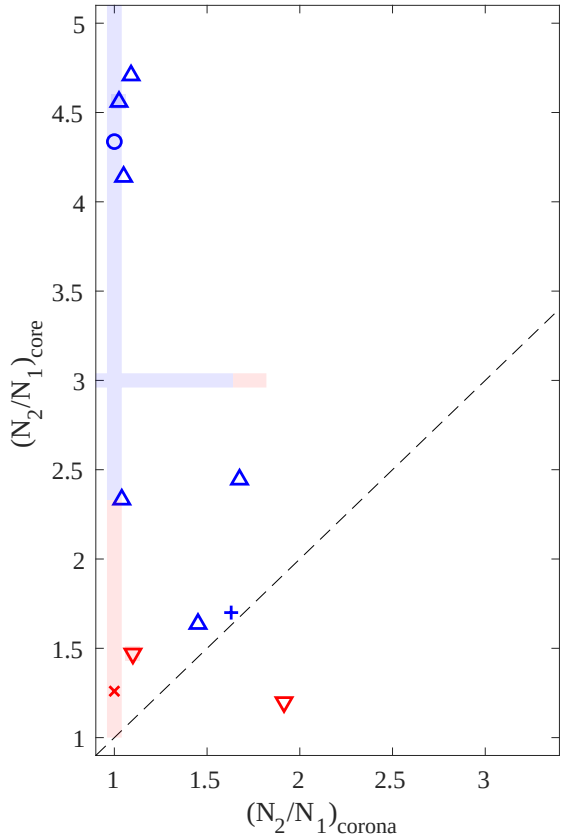

Figure 6.1: A plot of $(N_2/N_1)_{\text{core}}$ *vs* $(N_2/N_1)_{\text{corona}}$ indicating whether Frank-Kasper phases or related quasicrystals were (blue) or were not (red) observed in binary diblock blends with bidisperse core or corona blocks, based on prior studies. Shaded regions indicate the results of SCFT studies at conformational asymmetries of $\epsilon = 1.0$ and $\epsilon = 1.3$.[44,49,132,145] Triangles indicate experimental results in poly(styrene)-*b*-1,4-poly(butadiene) from various studies,[91,132,144,145] with blue upright triangles ($\triangle$) indicating emergence of FK phases and red inverted triangles ($\triangledown$) indicating no observed FK phases. Blends of poly(ethylene-*alt*-propylene)-*b*-poly(lactide) in which FK phases formed are marked with a blue plus (+) and those without FK phases are marked with a red X ($\times$).[39] Results from poly(styrene)-*b*-poly(methyl acrylate) blends are represented as blue circles.[143] Figure based on similar plot found in Ref. 144.

evaluation of results, was too lenient to draw valid conclusions. In particular, the approach ignored the macrophase separation that is always possible in a blend system. At a computational level, many phases were computed with insufficient spatial resolution, leading to concerns about the accuracy of those results. This problem was compounded as block lengths in one chain were increased, effectively increasing the already high segregation strength. Finally, the high segregation strength, along with known convergence

difficulties for Frank-Kasper phases in the PSCF software, led to a high frequency of failed SCFT convergence. This led to inconsistent availability of results, complicating analysis. Together these errors meant that rectifying the situation to obtain usable results would take excessive effort and the project was abandoned.

6.2 Methods

To address this question, SCFT calculations were performed for a variety of binary diblock blends of type AB/A′B′ where monomer A resides in the core, and monomer B resides in the corona. We fix the degree of polymerization, $N_1 = N_{1,A} + N_{1,B}$, and composition, $f_1 = N_{1,A}/N_1 = 0.15$, of the reference diblock, AB. Since our goal is to explore the limits of Frank-Kasper phase emergence with variation in core and corona block bidispersity, we allow the degree of polymerization of both blocks in the A′B′ chain, $N_{2,A}$ and $N_{2,B}$, to vary in order to obtain desired values of core length asymmetry, $(N_2/N_1)_{\text{core}} = N_{2,A}/N_{1,A}$, and corona length asymmetry, $(N_2/N_1)_{\text{corona}} = N_{2,B}/N_{1,B}$. For consistency with prior SCFT work on similar systems,[44] we fix the Flory-Huggins parameter in the system such that $\chi N_1 = 40$. To match the poly(styrene)-*b*-1,4-poly(butadiene) polymers studied in related experimental work,[144] we select a conformational asymmetry $\epsilon = b_{\text{A}}/b_{\text{B}} = 1.3$. At each explored value of $(N_2/N_1)_{\text{core}}$ and $(N_2/N_1)_{\text{corona}}$, we attempt to sample the full range of blend fractions, $\phi_1 = 1 - \phi_2 \in [0, 1]$ for each phase. We consider 3 canonical phases (bcc, hex, and lam) as well as five Frank-Kasper phases (A15, C14, C15, σ, and Z). Calculations are performed in the Fortran version of PSCF using the canonical ensemble, and converged to an error tolerance of 1×10^{-5}, as defined in Ref. 66.

In this work, our goal was to evaluate at which $(N_2/N_1)_{\text{core}}$ and $(N_2/N_1)_{\text{corona}}$ values FK phases would have the potential to emerge. Although this goal is similar to construction of a phase diagram, the "phase diagram" itself would be obscured by the projection used in Fig. 6.1. Based on this, we hypothesized that construction of formal, rigorous phase diagrams would not be necessary, and that we could instead rely on a looser criterion: the "competitiveness" of Frank-Kasper phases. In this "competitiveness" framing, we define a given $(N_2/N_1)_{\text{core}}$ and $(N_2/N_1)_{\text{corona}}$ as having the *potential* to form FK phases if, at any ϕ_1, one of the FK phases has the lowest Helmholtz free

energy among the candidate phases. As will be discussed later, this particular approach proved to be too lenient for the project.

6.3 Results and Discussion

6.3.1 Impact of Spatial Resolution

The spatial resolution in an SCFT calculation must be set high enough that the calculation can smoothly resolve interfaces. A failure to do so can lead to inaccuracies in computed free energies as well as convergence difficulties. A properly resolved SCFT calculation will have smoothly varying concentration profiles across interfaces, such as the the concentration profiles shown in Fig. 6.2. The optimal spatial resolution will depend on multiple factors, but ultimately hinges on resolution of interfacial concentration profiles. One very important factor in this selection is the complexity of the structure being studied. More complex phases will have more interfaces to resolve within the domain. In this regard, consider the cubic phases C15 and bcc: the C15 phase is far more complex than the bcc phase. Despite both phases being cubic unit cells, the C15 phase, containing 24 particles in a unit cell, has far more interfaces within that cube than bcc, which contains only two particles, and thus C15 requires greater resolution along each basis vector. The other important factor is the width of interfaces. Narrow interfaces require more nodes to smoothly resolve the rapidly changing composition, thus requiring more spatial resolution. When selecting resolutions for the candidate phases in this project, we did not properly account for the impact of this interfacial width and selected spatial resolutions that were too coarse-grained.

When choosing spatial discretizations for candidate phases in this work, we used data from prior work[33] showing the extent to which the free energy computed by PSCF varied with grid size. These calculations considered a polymer very similar to our reference AB chain, with $\chi N = 40$ and $f_{\mathrm{A}} = 0.15$, but with slightly higher conformational asymmetry. From the reported data, the lower resolution was chosen when the computed free energy differed by less than $1 \times 10^{-4}\ k_B T$ per chain between the lower and higher resolution calculations. With the data suggesting minimal change in the free energy by increasing the resolution, we felt that the reduced computational cost of the lower-resolution calculations would be valuable. Upon visual inspection of the converged fields

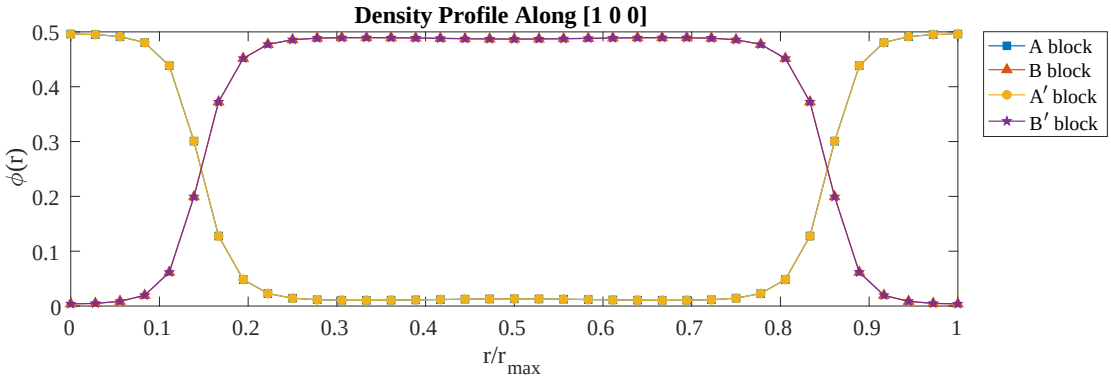

Figure 6.2: The concentration profile of each unique block in the AB/A′B′ blend system along the [100] direction of the A15 phase. Represented blend is for a system with $\phi_1 = 0.5$, $(N_2/N_1)_{\text{core}} = 1$, $(N_2/N_1)_{\text{corona}} = 1$, and $\epsilon = 1.3$.

from initial calculations (with no core or corona block asymmetry), most of the fields seemed to have reasonable resolution. As an example, consider the concentration profile shown in Fig. 6.2, which represents this initial condition with a blend fraction $\phi_1 = 0.5$ for A15.

Accepting *adequate* resolution at the most forgiving condition of two identical chains ended up being a substantial oversight. We did not consider at the time the degree to which changes to the degree of polymerization of the second chain would impact the resolution needed for the calculations. Increasing the degree of polymerization of the A′B′ chain relative to the AB chain increased the effective segregation strength of the system: if $\chi N_1 = 40$, then $\chi N_2 = 40 \times (N_2/N_1)$, with the effective segregation strength being a weighted average. Increasing this effective segregation strength meant that the interfaces in each structure were narrowing, which then requires higher resolution. As an example, consider Fig. 6.3, which depicts the concentration profile along the same direction in the A15 unit cell as Fig. 6.2, but for $(N_2/N_1)_{\text{core}} = 3$ and $(N_2/N_1)_{\text{corona}} = 3.35$. In this figure, concentration profiles for all blocks are well-resolved near the micelle cores (far right and far left) and in the matrix (near $r/r_{max} = 0.5$). The problem arises on the interfaces where the concentration profiles, particularly for the AB chain, are significantly under-resolved. Looking at the concentration profile of the A block, the local volume fraction rises from $\phi(r) \approx 0.2$ to $\phi(r) \approx 0.5$ across four nodes from the interior of the micelle to the shell of the core-shell micelle and rapidly drops again to

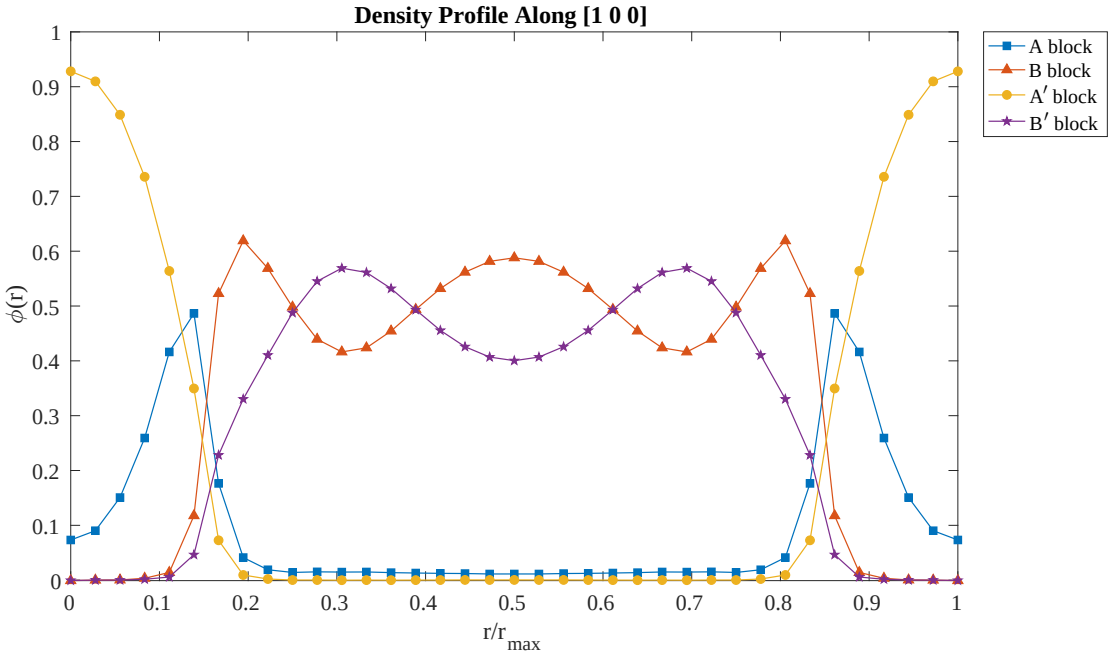

Figure 6.3: The concentration profile of each unique block in the AB/A′B′ blend system along the [100] direction of the A15 phase. Represented blend is for a system with $\phi_1 = 0.5$, $(N_2/N_1)_{\text{core}} = 3$, $(N_2/N_1)_{\text{corona}} = 3.35$, and $\epsilon = 1.3$.

$\phi(r) < 0.1$ over just two nodes from the micelle shell to the matrix. Similarly poor resolution was present for other phases as well.

The inadequacy of this spatial discretization meant that there was a high likelihood of erroneous free energies in many of our calculations. Indeed, Fig. 6.4 depicts computed free energies for each candidate phase relative to bcc and highlights some of these errors. This is most obvious for the A15 phase, which displays a strong oscillatory behavior in its predicted free energy at low ϕ_1. Similar, but smaller, oscillations also occur for the Frank-Kasper Z phase. Such behavior reflects an artifact of the numerical method (likely the low spatial resolution) rather than any physical property of the system. We should note that such substantial numerical inconsistencies do not appear everywhere in the data: the example shown in Fig. 6.4 is an outlier in terms of the severity of these numerical issues. There were many instances of energy profiles displaying only modest inconsistencies such as that shown in Fig. 6.5, which has only minor discontinuities in one phase (Z) where another phase (A15) is clearly (according to the data) more

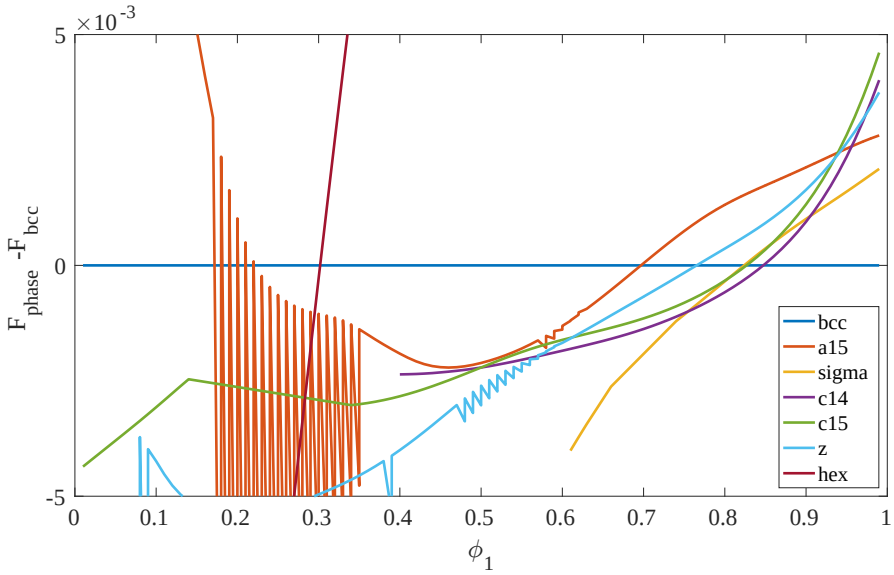

Figure 6.4: The free energy of each candidate phase relative to bcc ($F_{phase} - F_{bcc}$) versus blend fraction of the AB chain ϕ_1 for a blend with $(N_2/N_1)_{\text{core}} = 3$ and $(N_2/N_1)_{\text{corona}} = 1.4$, showing inconcistencies in computed free energy for multiple FK phases including A15, Z, C15, and σ.

stable. There were also many instances of energy profiles such as that shown in Fig. 6.6 which display smoothly varying energy curves without any noticeable discontinuities. Regardless, appearance of such significant problems raises doubts about the veracity of other data from the study, even data which demonstrates little to no erroneous behavior.

6.3.2 Convergence Difficulties

In completing this project, PSCF's sweep functionality was used frequently to obtain results across a range of blend fractions or block lengths. This operation, in the Fortran code, uses first-order continuation methods after each converged result to obtain an initial guess field for the SCFT calculation at the next sweep point. As with any SCFT calculation, it is always possible for a calculation at one point in the sweep to fail to converge. The program responds to this failure by backtracking and reducing the step size. However, if calculations continue to fail, the program will terminate a sweep when the step size falls below a threshold.

While completing this project, these sweep failures tended to happen often and in a highly unpredictable way. By way of illustration, Fig. 6.7 shows the positions at

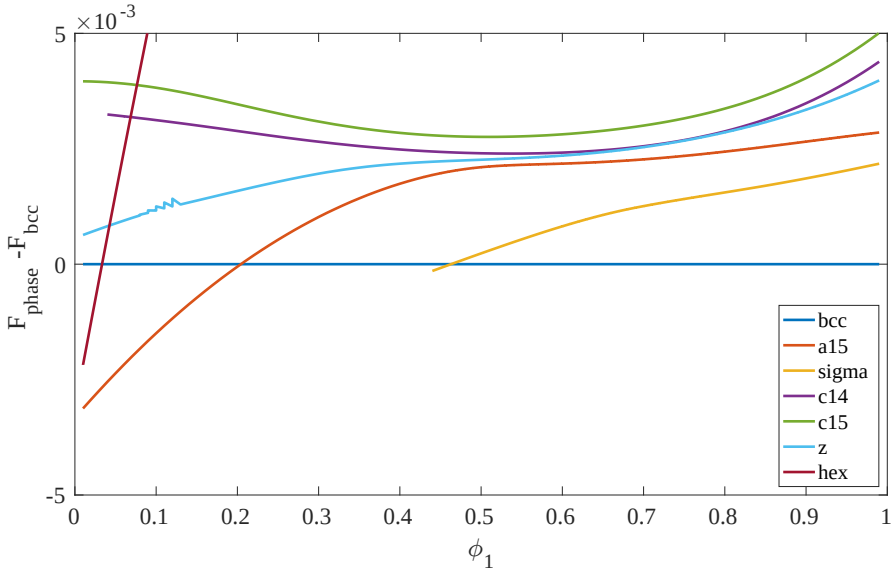

Figure 6.5: The free energy of each candidate phase relative to bcc ($F_{phase} - F_{bcc}$) versus blend fraction of the AB chain ϕ_1 for a blend with $(N_2/N_1)_{\text{core}} = 2$ and $(N_2/N_1)_{\text{corona}} = 1.54$, showing only minor inconsistencies in the Z phase energy profile.

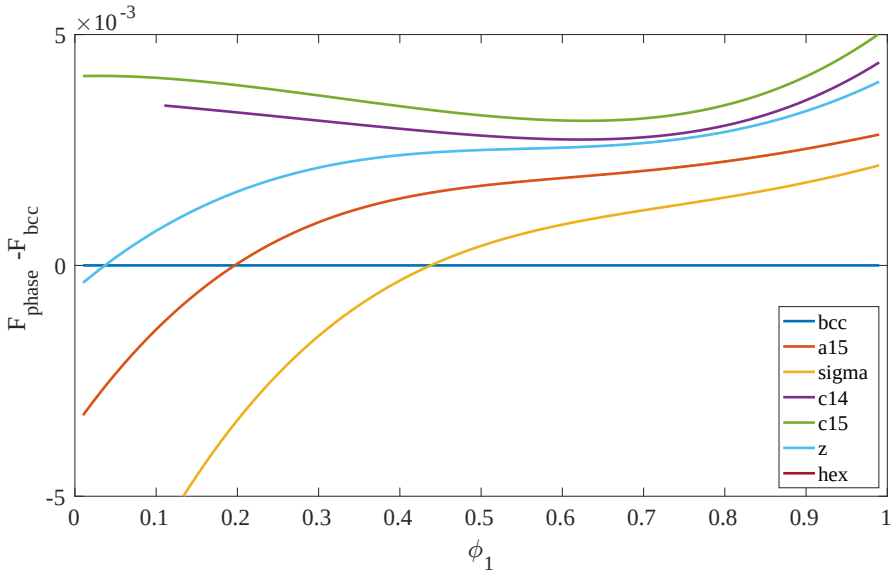

Figure 6.6: The free energy of each candidate phase relative to bcc ($F_{phase} - F_{bcc}$) versus blend fraction of the AB chain ϕ_1 for a blend with $(N_2/N_1)_{\text{core}} = 2$ and $(N_2/N_1)_{\text{corona}} = 2.41$, showing consistent energy profiles, with no obvious discontinuities or other erroneous behavior.

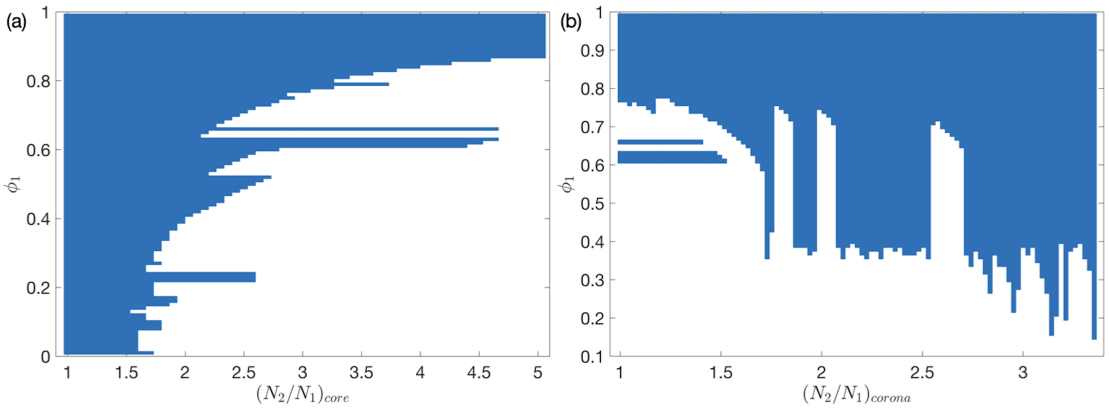

Figure 6.7: A plot of positions at which σ phase converged in (a) ϕ_1 vs $(N_2/N_1)_{\text{core}}$ space with $(N_2/N_1)_{\text{corona}} = 1$, and (b) ϕ_1 vs $(N_2/N_1)_{\text{corona}}$ space with $(N_2/N_1)_{\text{core}} = 3$. In (a) sweeps were only done in $(N_2/N_1)_{\text{core}}$. In (b) an initial sweep was done in $(N_2/N_1)_{\text{corona}}$ wherever data were available, and a secondary sweep was done in ϕ_1 from high ϕ_1 to low ϕ_1.

which the FK σ phase converged within two phase planes explored in the calculation. The first of these (Fig. 6.7a) shows σ convergence in the ϕ_1 vs $(N_2/N_1)_{\text{core}}$ plane with $(N_2/N_1)_{\text{corona}} = 1$ The initial point for sweeps in this data set were at the left side of the plot, at all possible blend fractions of, essentially, a pseudo-single-component system containing two identical diblock copolymers. As we would expect, all of those initial calculations converge. Sweeps were used to sequentially increase $N_{\text{A},2} > N_{\text{A},1}$ and thus to change $(N_2/N_1)_{\text{core}}$. General trends in convergence behavior for this phase-plane, with calculations tending to fail at the bottom-right of the figure are unsurprising. As $N_{\text{A},2}$ is increased at constant $N_{\text{B},2}$ (moving to the right), core block fraction of the second chain, $f_2 = N_{\text{A},2}/(N_{\text{A},2} + N_{\text{B},2})$, is increased, reaching a value of $f_2 = 0.47$ at the right-most position in the figure. Such a high block fraction makes the A′B′ chain lamellae-forming in the neat melt, and makes A′B′-rich blends increasingly unfavorable for particle-forming phases such as σ. The surprising outcome here is the relatively inconsistent point of failure for many of these calculations. Calculations at high ϕ_1 tend to succeed, and the failure point of the sweeps clearly trend to lower $(N_2/N_1)_{\text{core}}$ as ϕ_1 is decreased. Just above $\phi_1 = 0.6$, however, a set of calculations suddenly converge out to very high core block asymmetry. Lowering ϕ_1 further again sees reduced sweep convergence before spiking again around $\phi_1 = 0.5$. There is yet further noise in the convergence behavior at low ϕ_1 with a particularly prominent spike

just above $\phi_1 = 0.2$. The second panel depicts σ convergence on the ϕ_1 vs $(N_2/N_1)_{\text{corona}}$ plane with $(N_2/N_1)_{\text{core}} = 3$. The data shown in this plot were generated with two sets of sweeps. The first, a sweep in $N_{\text{B},2}$ from the converged fields at $(N_2/N_1)_{\text{core}} = 3$ in Fig. 6.7a, yielded the horizontal bars just above $\phi_1 = 0.6$ seen in the plot as well as convergence out to the right side of the figure for $\phi_1 > 0.8$. A second set of sweeps down from $\phi_1 = 0.8$ were then done to collect data over more of the phase plane. In this plane, convergence of the σ phase is expected to be worst in the lower left, where blends are rich in an A′B′ chain with $f_2 \approx 0.35$ which is far too high for spherical micelle formation in a neat A′B′ melt. Based on this observation, better convergence at higher $(N_2/N_1)_{\text{corona}}$ is unsurprising, but the occasional regions of very poor convergence (around $(N_2/N_1)_{\text{corona}} \approx 1.75, 2, 2.6$) are still very strange. Certainly, some variation in convergence behavior can be reasonably expected with any numerical methods, but these results show a puzzling inconsistency in the convergence behavior of the σ phase calculation, with similarly puzzling inconsistency for other phases.

Convergence of Frank-Kasper phases has proved difficult before in many cases. Indeed, we discussed similar convergence difficulties in Chapter 4. In part, the high segregation strength used in these calculations, $\chi N_1 = 40$, contributes to some of this convergence difficulty. Generally, the PSCF software struggles to converge FK phases at segregation strengths above $\chi N = 40$. Running these calculations near the software's upper limit for Frank-Kasper phase convergence is only made worse by increasing the length of the A′B′ chain, which has the effect of increasing the effective segregation strength, as discussed previously. Convergence of these calculations was likely also made more difficult by the spatial resolution problems discussed in Section 6.3.1.

The unpredictability of phase convergence, and large regions of missing data made analysis of the data difficult and led to very noisy results when applying the competitiveness criteria we chose for our analysis, which will be discussed in Section 6.3.3. Improperly accounting for the effect of these segregation strength changes with increasing chain length, and the resultant effect on convergence, was one of several challenges encountered while working on this project.

6.3.3 Issues with Competitiveness Metric

Our results using the competitiveness framework defined in Section 6.2 are shown in Fig. 6.8. In generating this figure, we have retained the general format of Fig. 6.1, as well as the experimental data. We have replaced the computational predictions from prior studies with the results of our analysis. Looking at our predictions in this figure (shaded rectangles) we see three overarching trends. First, when the polymer cores are monodisperse ($(N_2/N_1)_{\text{core}} = 1$), no degree of corona bidispersity stabilizes the Frank-Kasper phases. As discussed in the introduction, the current understanding of Frank-Kasper phase emergence in AB/A′B′ blends relies on core block asymmetry, such that the distinct core blocks can preferentially segregate to different particle positions or different regions of the particle interface. If both core blocks are identical, this mechanism for FK phase stabilization would no longer be available, and there is no expectation that corona block asymmetry would have a favorable effect on FK phase formation. Thus, our prediction of this trend remain consistent with our expectation and current understanding of the systems.

In the second trend, we see Frank-Kasper phase emergence with increasing core block asymmetry when the corona blocks are monodisperse ($(N_2/N_1)_{\text{corona}} = 1$). If we compare this trend in Fig. 6.8 to that from prior works [44,49] shown in Fig. 6.1, we see that our work predicts FK phase emergence at a much lower degree of core block asymmetry. Prior work predicts FK phases to emerge at $(N_2/N_1)_{\text{core}} \approx 2.33$ [44,49] while we predict FK phase emergence at $(N_2/N_1)_{\text{core}} \approx 1.5$. Note that due to the sampling interval used in our work, data were not collected at exactly $(N_2/N_1)_{\text{core}} = 1.5$; we leave a gap in the shaded region of Fig. 6.8 to indicate that this exact transition was not resolved. The main panel of Fig. 6.9 shows the "phase diagram" in ϕ_1 vs $(N_2/N_1)_{\text{core}}$ generated by our method and showing the phase with the lowest free energy at each point; the inset of Fig. 6.9 re-plots data from Kim et al. over the same range of $(N_2/N_1)_{\text{core}}$ for comparison. Note that, particularly among the Frank-Kasper phases, the stability windows in our data are rather inconsistent due to the convergence difficulties discussed in Section 6.3.2. As seen in Fig. 6.9, our work yields results that are qualitatively similar to results of prior work shown in the inset,[49] with the FK σ phase emerging in a broadening window between bcc and hex with increasing $(N_2/N_1)_{\text{core}}$, followed by emergence of the C14 Laves phase at high ϕ_1 as $(N_2/N_1)_{\text{core}}$ increases further. The emergence of FK phases

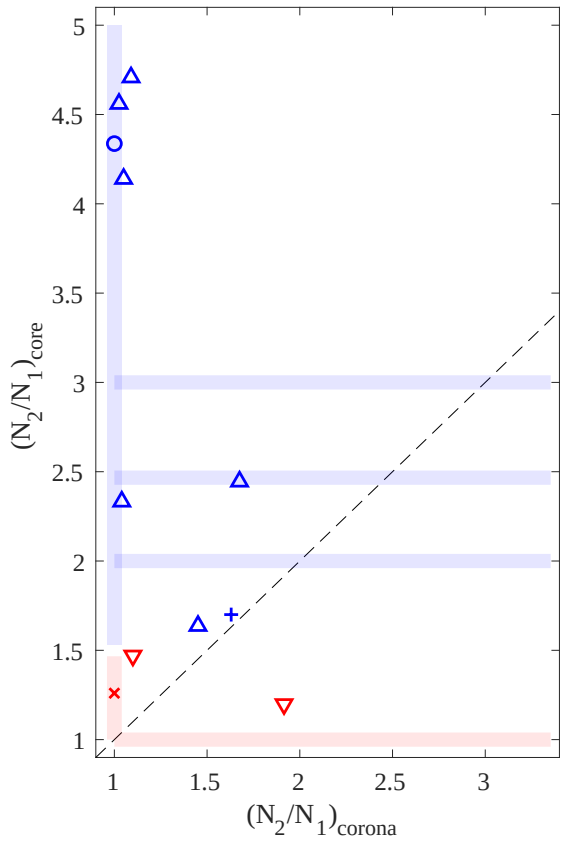

Figure 6.8: A plot of $(N_2/N_1)_{\text{core}}$ *vs* $(N_2/N_1)_{\text{corona}}$ indicating whether Frank-Kasper phases were (blue) or were not (red) observed in binary diblock blends with bidisperse core or corona blocks. Shaded regions indicate the SCFT results from this work. Markers represent experimental results. Triangles indicate experimental results in poly(styrene)-*b*-1,4-poly(butadiene) from various studies,[91,132,144,145] with blue upright triangles (△) indicating emergence of FK phases and red inverted triangles (▽) indicating no observed FK phases. Blends of poly(ethylene-*alt*-propylene)-*b*-poly(lactide) in which FK phases formed are marked with a blue plus (+) and those without FK phases are marked with a red X (×).[39] Results from poly(styrene)-*b*-poly(methyl acrylate) blends are represented as blue circles.[143]

at lower $(N_2/N_1)_{\text{core}}$ in our data results from the modest conformational asymmetry we use. Although $\epsilon = 1.3$ is not sufficient to stabilize FK phases in the neat melt, we would expect it to slightly stabilize FK phases relative to bcc or hex everywhere, thus reducing the core block asymmetry required to stabilize FK phases in the blend.

Finally, we see that after the core block asymmetry becomes sufficiently high, no degree of corona block asymmetry seems to destabilize the Frank-Kasper phases. Based

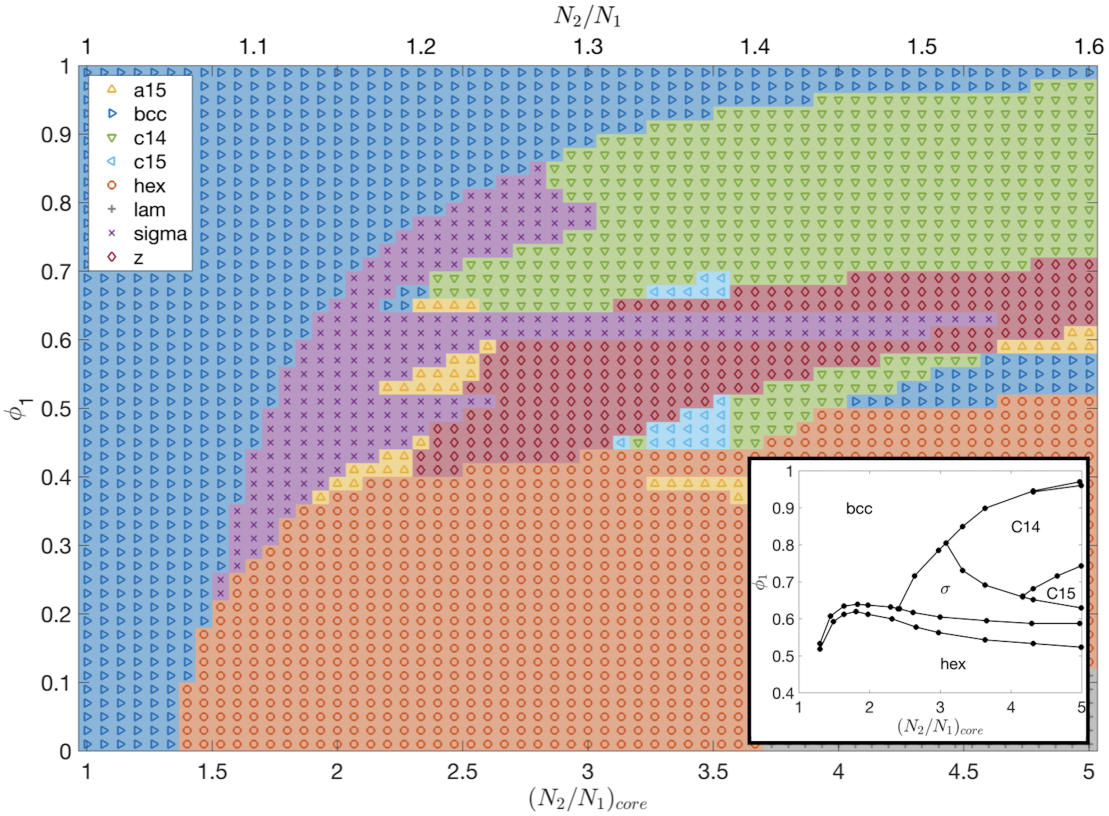

Figure 6.9: Stable phase predicted in binary diblock blends with bidisperse core blocks and monodisperse corona blocks with conformational asymmetry $\epsilon = 1.3$ and segregation strength $\chi N = 40$ based on the "competitiveness" metric using SCFT Helmholtz free energy for each phase and only considering, at each point, phases which converged in the SCFT calculation. Data from Kim et al.[49] for conformationally symmetric AB/A′B′ blends in the same phase plane are depicted in the inset. To show greater detail, the inset uses a narrower range in ϕ_1 than the main figure.

on our current understanding of the mechanisms for FK formation in bidisperse diblock copolymer blends, and our working hypothesis for the impacts of core and corona bidispersity, we would expect that at any fixed core block asymmetry there would be an upper limit to the corona block asymmetry which would still allow FK phases to form. Similar to Fig. 6.9, Fig. 6.10 depicts the predicted stable phase according to our competitiveness metric with varying $(N_2/N_1)_{\text{corona}}$ at a constant $(N_2/N_1)_{\text{core}} = 3$.* Examining these data, we see that not only does the FK window remain open, but above

*Fig. 6.7b represents the sigma convergence over the same range as shown in Fig. 6.10

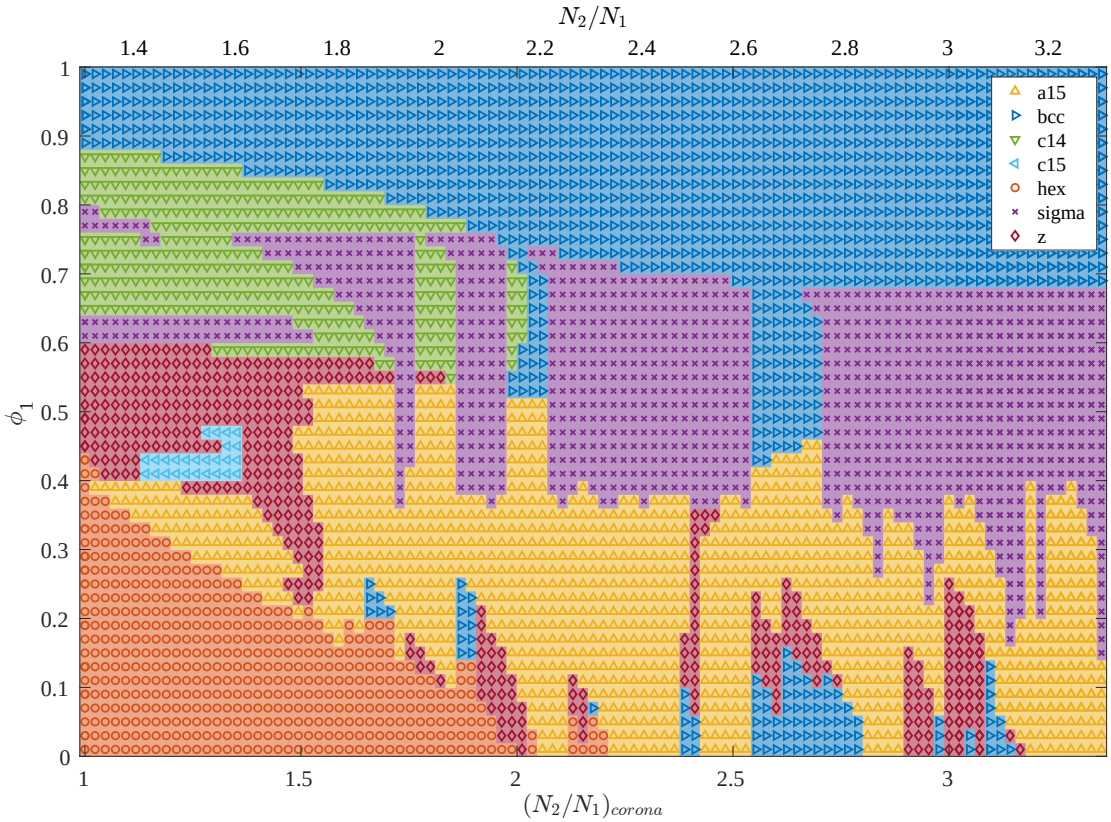

Figure 6.10: Stable phase predicted in binary diblock blends with $(N_2/N_1)_{\text{core}}$ and variable $(N_2/N_1)_{\text{corona}}$ with conformational asymmetry $\epsilon = 1.3$ and segregation strength $\chi N = 40$ based on the "competitiveness" metric using SCFT Helmholtz free energy for each phase and only considering, at each point, phases which converged in the SCFT calculation.

$(N_2/N_1)_{\text{corona}} \approx 2.5$ it does not even seem to change in any appreciable way. This result runs counter to our expectations and lies in sharp contrast with the results presented by Liu et al. across a comparable phase space.[44] We suspect that, to some extent, our omission of macrophase separation likely resulted in some of this perplexing behavior. Unfortunately, the problems with spatial resolution and convergence complicate a detailed analysis of these issues, and we are unable to draw definitive conclusions from it. Ultimately, we decided that the work presented in Chapter 5 (which was the final project in chronological order) was both more interesting and more feasible, and chose to devote our efforts to that project rather than resolve the technical issues required to address the questions posed in this chapter.

6.4 Conclusion

In this work, we have attempted to delve more deeply into the role and limits of corona block asymmetry in the formation of FK phases in AB/A′B′ blends. Unfortunately, several complexities of the blends we studied were improperly accounted for, leading to unreliable results. At the outset of our study, we failed to account for changes in effective segregation strength that would result from increasing the degree of polymerization of the A′B′ chain; this oversight caused us to select an insufficient spatial resolution for many of the phases to be able to properly resolve the micelle interfaces. This failure to appropriately resolve the potential fields led to unreliable free energy data and brought many of our results into question. The low grid size chosen for the calculations also likely increased the difficulty in converging SCFT calculations, which created large gaps in our data, thus potentially obscuring many effects or phase transitions. Finally, our methodology for determining potential FK phase emergence seems to have been over-simplified by ignoring the very real risk of macrophase separation. The other underlying problems with the calculations, however, made it impossible to properly confirm if this was truly the cause of several puzzling results from our work. Most significantly, we hope that the oversights in this work may serve as a lesson on the importance of carefully considering the set-up of a research project and complicating factors which may impact the data.

Chapter 7

Conclusion and Future Directions

Throughout this thesis, we have discussed multiple projects on a variety of topics in the block polymer space. To conclude, we take this final chapter to summarize the work, and bring the discussion back to the broader context of block polymer research by identifying remaining open questions and offering suggestions for further work in light of our findings.

Chapter 3 detailed a software tool to streamline the process of generating initial guess fields for SCFT calculations. This program generalized the methods described by prior researchers[61,72,74,75] to handle (through a single program with uniform interface) a wide variety of morphologies. Although the software represents an advancement in the generation of SCFT guess fields, it still has limitations. Restriction of each guess to a single core monomer imposes substantial limitations on the variety of morphologies that can be considered. As researchers begin to probe more exotic nanostructures, the methods will need to be further generalized. The form-factor method is a particularly good candidate for this extension. Enabling core monomer specification for individual particles would grant access to structures such as the alloys explored in Chapter 5. Adding a wider variety of particle form-factors would open the possibility of still more morphologies. Combining these two improvements would allow a creative user to approximate more complex structures (even non-particle structures) with careful placement of available particles.

The guess generation software served a secondary purpose as a component of the inverse design software detailed in Chapter 4. This software was designed to automate

the computational search of large design spaces for regions of phase space that most stabilize a target morphology. In this work, SCFT was used to solve the forward problem of phase stability at each point in phase space, while particle swarm optimization drove solution of the inverse problem by guiding the search through phase space. Performance and robustness of the software was demonstrated with three searches in the neat diblock phase space. Despite being a valuable addition to the block polymer software space, improvements could be made to the software. On one end, performance of the software could be improved. Acceleration of the underlying SCFT calculations via GPU would substantially boost performance. Additionally, the seed field methodology could be expanded to combine the generation and library methodologies to accelerate convergence during PSO steps. Functionality of the software could also be improved by addressing the complexities imposed by macrophase separation in blends.

The alloy system investigated in Chapter 5 offered further insight into the role of conformational asymmetry in the formation of Frank-Kasper phases. In particular, we demonstrated more subtly the contribution of conformational asymmetry and how more targeted control of the parameter could be a powerful driver of specialty material design. This study did, however, only focus on the Frank-Kasper Laves phases. It remains an open question how widely this approach can be applied, and what other phases may be accessible through targeted property control. It also remains to be seen whether such alloy systems are experimentally accessible.

Finally, in Chapter 6 we presented an ultimately unsuccessful attempt to probe the relationship between core and corona block asymmetry in Frank-Kasper phase formation in AB/A′B′ blends. This work suffered from oversights and methodological over-simplifications which greatly impacted both the reliability and the research utility of the generated data. Although unsuccessful in furthering research interests on the topic of block polymer self-assembly, the work does serve as a case study on the importance of careful and deliberate study design including a full consideration of potential complicating factors. If a future study were to correct the problems encountered in this work, it would have the potential to offer valuable insights into the limitations of FK phase emergence in bidisperse diblock blends.

References

[1] Bates, F. S.; Hillmyer, M. A.; Lodge, T. P.; Bates, C. M.; Delaney, K. T.; Fredrickson, G. H. Multiblock polymers: Panacea or Pandora's box? *Science* **2012**, *336*, 434–440.

[2] Bates, F. S.; Fredrickson, G. H. Block Copolymers—Designer Soft Materials. *Phys. Today* **1999**, *52*, 32–38.

[3] Bates, C. M.; Bates, F. S. 50th anniversary perspective: Block polymers-pure potential. *Macromolecules* **2017**, *50*, 3–22.

[4] P. Stoykovich, M.; Kang, H.; Ch. Daoulas, K.; Liu, G.; Liu, C.-C.; J. de Pablo, J.; Müller, M.; F. Nealey, P. Directed Self-Assembly of Block Copolymers for Nanolithography: Fabrication of Isolated Features and Essential Integrated Circuit Geometries. *ACS Nano* **2007**, *1*, 168–175.

[5] Hu, H.; Gopinadhan, M.; Osuji, C. O. Directed self-assembly of block copolymers: a tutorial review of strategies for enabling nanotechnology with soft matter. *Soft Matter* **2014**, *10*, 3867.

[6] Liu, C.-C.; Franke, E.; Mignot, Y.; Xie, R.; Yeung, C. W.; Zhang, J.; Chi, C.; Zhang, C.; Farrell, R.; Lai, K.; Tsai, H.; Felix, N.; Corliss, D. Directed self-assembly of block copolymers for 7 nanometre FinFET technology and beyond. *Nat. Electron.* **2018**, *1*, 562–569.

[7] Sveinbjörnsson, B. R.; Weitekamp, R. A.; Miyake, G. M.; Xia, Y.; Atwater, H. A.; Grubbs, R. H. Rapid self-assembly of brush block copolymers to photonic crystals. *Proc. Natl. Acad. Sci. USA* **2012**, *109*, 14332–14336.

[8] J. Macfarlane, R.; Kim, B.; Lee, B.; A. Weitekamp, R.; M. Bates, C.; Fung Lee, S.; B. Chang, A.; T. Delaney, K.; H. Fredrickson, G.; A. Atwater, H.; H. Grubbs, R. Improving Brush Polymer Infrared One-Dimensional Photonic Crystals via Linear Polymer Additives. *J. Am. Chem. Soc.* **2014**, *136*, 17374–17377.

[9] Jackson, E. A.; Hillmyer, M. A. Nanoporous Membranes Derived from Block Copolymers: From Drug Delivery to Water Filtration. *ACS Nano* **2010**, *4*, 3548–3553.

[10] Phillip, W. A.; O'Neill, B.; Rodwogin, M.; Hillmyer, M. A.; Cussler, E. L. Self-Assembled Block Copolymer Thin Films as Water Filtration Membranes. *ACS Appl. Mater. Interfaces* **2010**, *2*, 847–853.

[11] Pereira Nunes, S. Block Copolymer Membranes for Aqueous Solution Applications. *Macromolecules* **2016**, *49*, 2905–2916.

[12] Matsen, M. W. Field theoretic approach for block polymer melts: SCFT and FTS. *J. Chem. Phys.* **2020**, *152*, 110901.

[13] Matsen, M. W.; Schick, M. Stable and unstable phases of a diblock copolymer melt. *Phys. Rev. Lett.* **1994**, *72*, 2660–2663.

[14] Matsen, M. W.; Bates, F. S. Unifying Weak- and Strong-Segregation Block Copolymer Theories. *Macromolecules* **1996**, *29*, 1091–1098.

[15] Semenov, A. N. Microphase separation in diblock-copolymer melts: ordering of micelles. *Macromolecules* **1989**, *22*, 2849–2851.

[16] Huang, Y.-Y.; Hsu, J.-Y.; Chen, H.-L.; Hashimoto, T. Existence of fcc-Packed Spherical Micelles in Diblock Copolymer Melt. *Macromolecules* **2007**, *40*, 406–409.

[17] Hsu, N.-W.; Nouri, B.; Chen, L.-T.; Chen, H.-L. Hexagonal Close-Packed Sphere Phase of Conformationally Symmetric Block Copolymer. *Macromolecules* **2020**, *53*, 9665–9675.

[18] Leibler, L. Theory of Microphase Separation in Block Copolymers. *Macromolecules* **1980**, *13*, 1602–1617.

[19] Bates, F. S.; Cohen, R. E.; Berney, C. V. Small-angle neutron scattering determination of macrolattice structure in a polystyrene-polybutadiene diblock copolymer. *Macromolecules* **1982**, *15*, 589–592.

[20] Thomas, E. L.; Kinning, D. J.; Alward, D. B.; Henkee, C. S. Ordered packing arrangements of spherical micelles of diblock copolymers in two and three dimensions. *Macromolecules* **1987**, *20*, 2934–2939.

[21] Hajduk, D. A.; Harper, P. E.; Gruner, S. M.; Honeker, C. C.; Kim, G.; Thomas, E. L.; Fetters, L. J. The Gyroid: A New Equilibrium Morphology in Weakly Segregated Diblock Copolymers. *Macromolecules* **1994**, *27*, 4063–4075.

[22] Tyler, C. A.; Morse, D. C. Orthorhombic Fddd network in triblock and diblock copolymer melts. *Phys. Rev. Lett.* **2005**, *94*, 208302.

[23] Takenaka, M.; Wakada, T.; Akasaka, S.; Nishitsuji, S.; Saijo, K.; Shimizu, H.; Kim, M. I.; Hasegawa, H. Orthorhombic Fddd network in diblock copolymer melts. *Macromolecules* **2007**, *40*, 4399–4402.

[24] Bates, F. S.; Schulz, M. F.; Rosedale, J. H.; Almdal, K. Correlation of binary polyolefin phase behavior with statistical segment length asymmetry. *Macromolecules* **1992**, *25*, 5547–5550.

[25] Vavasour, J. D.; Whitmore, M. D. Self-consistent field theory of block copolymers with conformational asymmetry. *Macromolecules* **1993**, *26*, 7070–7075.

[26] Milner, S. T. Chain Architecture and Asymmetry in Copolymer Microphases. *Macromolecules* **1994**, *27*, 2333–2335.

[27] Matsen, M. W.; Schick, M. Microphases of a Diblock Copolymer with Conformational Asymmetry. *Macromolecules* **1994**, *27*, 4014–4015.

[28] Lee, S.; Bluemle, M. J.; Bates, F. S. Discovery of a Frank-Kasper σ Phase in Sphere-Forming Block Copolymer Melts. *Science* **2010**, *330*, 349–353.

[29] Xie, N.; Li, W.; Qiu, F.; Shi, A.-C. σ phase formed in conformationally asymmetric AB-type block copolymers. *ACS Macro Lett.* **2014**, *3*, 906–910.

[30] Bates, M. W.; Lequieu, J.; Barbon, S. M.; Lewis III, R. M.; Delaney, K. T.; Anastasaki, A.; Hawker, C. J.; Fredrickson, G. H.; Bates, C. M. Stability of the A15 phase in diblock copolymer melts. *Proc. Natl. Acad. Sci. USA* **2019**, *116*, 13194–13199.

[31] Grason, G. M.; DiDonna, B. A.; Kamien, R. D. Geometric Theory of Diblock Copolymer Phases. *Phys. Rev. Lett.* **2003**, *91*, 1–4.

[32] Grason, G. M. The packing of soft materials: Molecular asymmetry, geometric frustration and optimal lattices in block copolymer melts. *Phys. Rep.* **2006**, *433*, 1–64.

[33] Kim, K.; Schulze, M. W.; Arora, A.; Lewis III, R. M.; Hillmyer, M. A.; Dorfman, K. D.; Bates, F. S. Thermal processing of diblock copolymer melts mimics metallurgy. *Science* **2017**, *356*, 520–523.

[34] Frank, F. C.; Kasper, J. S. Complex alloy structures regarded as sphere packings. I. Definitions and basic principles. *Acta Crystallogr.* **1958**, *11*, 184–190.

[35] Frank, F. C.; Kasper, J. S. Complex alloy structures regarded as sphere packings. II. Analysis and classification of representative structures. *Acta Crystallogr.* **1959**, *12*, 483–499.

[36] de Graef, M.; McHenry, M. E. *Structure of Materials*, 2nd ed.; Cambridge University Press, 2012.

[37] Lee, S.; Leighton, C.; Bates, F. S. Sphericity and symmetry breaking in the formation of Frank–Kasper phases from one component materials. *Proc. Natl. Acad. Sci. USA* **2014**, *111*, 17723–17731.

[38] Gillard, T. M.; Lee, S.; Bates, F. S. Dodecagonal quasicrystalline order in a diblock copolymer melt. *Proc. Natl. Acad. Sci. USA* **2016**, *113*, 5167–5172.

[39] Schulze, M. W.; Lewis III, R. M.; Lettow, J. H.; Hickey, R. J.; Gillard, T. M.; Hillmyer, M. A.; Bates, F. S. Conformational Asymmetry and Quasicrystal Approximants in Linear Diblock Copolymers. *Phys. Rev. Lett.* **2017**, *118*, 207801.

[40] Jeon, S.; Jun, T.; Jo, S.; Ahn, H.; Lee, S.; Lee, B.; Ryu, D. Y. Frank–Kasper Phases Identified in PDMS-b-PTFEA Copolymers with High Conformational Asymmetry. *Macromol. Rapid Commun.* **2019**, *40*, 1900259.

[41] Barbon, S. M.; Song, J.-A.; Chen, D.; Zhang, C.; Lequieu, J.; Delaney, K. T.; Anastasaki, A.; Rolland, M.; Fredrickson, G. H.; Bates, M. W.; Hawker, C. J.; Bates, C. M. Architecture Effects in Complex Spherical Assemblies of $(AB)_n$-Type Block Copolymers. *ACS Macro Lett.* **2020**, *9*, 1745–1752.

[42] Mueller, A. J.; Lindsay, A. P.; Jayaraman, A.; Lodge, T. P.; Mahanthappa, M. K.; Bates, F. S. Emergence of a C15 Laves Phase in Diblock Polymer/Homopolymer Blends. *ACS Macro Lett.* **2020**, *9*, 576–582.

[43] Lindsay, A. P.; Cheong, G. K.; Peterson, A. J.; Weigand, S.; Dorfman, K. D.; Lodge, T. P.; Bates, F. S. Complex Phase Behavior in Particle-Forming AB/AB′ Diblock Copolymer Blends with Variable Core Block Lengths. *Macromolecules* **2021**, *54*, 7088–7101.

[44] Liu, M.; Qiang, Y.; Li, W.; Qiu, F.; Shi, A.-C. Stabilizing the Frank-Kasper Phases via Binary Blends of AB Diblock Copolymers. *ACS Macro Lett.* **2016**, *5*, 1167–1171.

[45] Bates, M. W.; Barbon, S. M.; Levi, A. E.; Lewis III, R. M.; Beech, H. K.; Vonk, K. M.; Zhang, C.; Fredrickson, G. H.; Hawker, C. J.; Bates, C. M. Synthesis and Self-Assembly of AB n Miktoarm Star Polymers. *ACS Macro Lett.* **2020**, *9*, 396–403.

[46] Cheong, G. K.; Bates, F. S.; Dorfman, K. D. Symmetry breaking in particle-forming diblock polymer/homopolymer blends. *Proc. Natl. Acad. Sci. USA* **2020**, *117*, 16764–16769.

[47] Xie, J.; Shi, A.-C. Formation of complex spherical packing phases in diblock copolymer/homopolymer blends. *Giant* **2021**, *5*, 100043.

[48] Xie, S.; Lindsay, A. P.; Bates, F. S.; Lodge, T. P. Formation of a C15 Laves Phase with a Giant Unit Cell in Salt-Doped A/B/AB Ternary Polymer Blends. *ACS Nano* **2020**, *14*, 13754–13764.

[49] Kim, K.; Arora, A.; Lewis III, R. M.; Liu, M.; Li, W.; Shi, A.-C.; Dorfman, K. D.; Bates, F. S. Origins of low-symmetry phases in asymmetric diblock copolymer melts. *Proc. Natl. Acad. Sci. USA* **2018**, *115*, 847–854.

[50] Dorfman, K. D. Frank–Kasper Phases in Block Polymers. *Macromolecules* **2021**, *54*, 10251–10270.

[51] Binder, K. *Monte Carlo and Molecular Dynamics Simulations in Polymer Science*; Oxford University Press, 1995.

[52] Binder, K.; Müller, M. Monte Carlo simulation of block copolymers. *Curr. Opin. Colloid Interface Sci.* **2000**, *5*, 314–322.

[53] Kremer, K.; Grest, G. S. Dynamics of entangled linear polymer melts: A molecular-dynamics simulation. *J. Chem. Phys.* **1990**, *92*, 5057–5086.

[54] Fredrickson, G. H.; Ganesan, V.; Drolet, F. Field-theoretic computer simulation methods for polymers and complex fluids. *Macromolecules* **2002**, *35*, 16–39.

[55] Fredrickson, G. H. *The Equilibrium Theory of Inhomogeneous Polymers*; Oxford University Press: Oxford, United Kingdom, 2006.

[56] Beardsley, T. M.; Spencer, R. K. W.; Matsen, M. W. Computationally Efficient Field-Theoretic Simulations for Block Copolymer Melts. *Macromolecules* **2019**, *52*, 8840–8848.

[57] Matsen, M. W. The standard Gaussian model for block copolymer melts. *J. Phys. Condens. Mat.* **2002**, *14*, R21–R47.

[58] Shi, A. In *Variational Methods in Molecular Modeling*; Wu, J., Ed.; Molecular Modeling and Simulation; Springer Singapore: Singapore, 2017; pp 155–180.

[59] `https://pscf.readthedocs.io/en/latest/index.html`, (accessed September 2022).

[60] Sinturel, C.; Bates, F. S.; Hillmyer, M. A. High χ–Low N Block Polymers: How Far Can We Go? *ACS Macro Lett.* **2015**, *4*, 1044–1050.

[61] Arora, A.; Qin, J.; Morse, D. C.; Delaney, K. T.; Fredrickson, G. H.; Bates, F. S.; Dorfman, K. D. Broadly Accessible Self-Consistent Field Theory for Block Polymer Materials Discovery. *Macromolecules* **2016**, *49*, 4675–4690.

[62] McQuarrie, D. A. *Statistical thermodynamics*; Harper & Row, 1973.

[63] Anderson, D. G. Iterative Procedures for Nonlinear Integral Equations. *J. Assoc. Comp. Mach.* **1965**, *12*, 547–560.

[64] Thompson, R. B.; Rasmussen, K.; Lookman, T. Improved convergence in block copolymer self-consistent field theory by Anderson mixing. *J. Chem. Phys.* **2004**, *120*, 31–34.

[65] Matsen, M. W. Fast and accurate SCFT calculations for periodic block-copolymer morphologies using the spectral method with Anderson mixing. *Eur. Phys. J. E* **2009**, *30*, 361.

[66] Arora, A.; Morse, D. C.; Bates, F. S.; Dorfman, K. D. Accelerating self-consistent field theory of block polymers in a variable unit cell. *J. Chem. Phys.* **2017**, *146*.

[67] Tyler, C. A.; Morse, D. C. Stress in Self-Consistent-Field Theory. *Macromolecules* **2003**, *36*, 8184–8188.

[68] Cheong, G. K.; Chawla, A.; Morse, D. C.; Dorfman, K. D. Open-source code for self-consistent field theory calculations of block polymer phase behavior on graphics processing units. *Eur. Phys. J. E* **2020**, *43*, 15.

[69] `https://github.com/dmorse/pscfpp`, (accessed May 2022).

[70] Delaney, K. T.; Fredrickson, G. H. Polymer field-theory simulations on graphics processing units. *Comp. Phys. Comm.* **2013**, *184*, 2102–2110.

[71] Case, L. J.; Delaney, K. T.; Fredrickson, G. H.; Bates, F. S.; Dorfman, K. D. Open-source platform for block polymer formulation design using particle swarm optimization. *Eur. Phys. J. E* **2021**, *44*, 115.

[72] Xu, W.; Jiang, K.; Zhang, P.; Shi, A.-C. A Strategy to Explore Stable and Metastable Ordered Phases of Block Copolymers. *J. Phys. Chem. B* **2013**, *117*, 5296–5305.

[73] Helfand, E.; Tagami, Y. Theory of the interface between immiscible polymers. II. *J. Chem. Phys.* **1972**, *56*, 3592–3601.

[74] Cochran, E. W. Thermodynamics, Simulation, and Modeling of Ordered Linear ABC Triblock Copolymers. Ph.D. thesis, University of Minnesota, 2004.

[75] Wohlgemuth, M.; Yufa, N.; Hoffman, J.; Thomas, E. L. Triply Periodic Bicontinuous Cubic Microdomain Morphologies by Symmetries. *Macromolecules* **2001**, *34*, 6083–6089.

[76] Qin, J. Studies of block copolymer melts by field theory and molecular simulation. Ph.D. thesis, University of Minnesota, 2009.

[77] Xie, Q.; Qiang, Y.; Zhang, G.; Li, W. Emergence and Stability of Janus-Like Superstructures in an ABCA Linear Tetrablock Copolymer. *Macromolecules* **2020**, *53*, 7380–7388.

[78] Xie, N.; Liu, M.; Deng, H.; Li, W.; Qiu, F.; Shi, A.-C. Macromolecular metallurgy of binary mesocrystals via designed multiblock terpolymers. *J. Am. Chem. Soc.* **2014**, *136*, 2974–2977.

[79] Chanpuriya, S.; Kim, K.; Zhang, J.; Lee, S.; Arora, A.; Dorfman, K. D.; Delaney, K. T.; Fredrickson, G. H.; Bates, F. S. Cornucopia of Nanoscale Ordered Phases in Sphere-Forming Tetrablock Terpolymers. *ACS Nano* **2016**, *10*, 4961–4972.

[80] Miyamori, Y.; Suzuki, J.; Takano, A.; Matsushita, Y. Periodic and Aperiodic Tiling Patterns from a Tetrablock Terpolymer System of the A1BA2C Type. *ACS Macro Lett.* **2020**, *9*, 32–37.

[81] Kaga, M.; Ohta, T. Dynamical approach to microphase separation in ABCA-type tetrablock terpolymers. *J. Phys. Soc. Japan* **2006**, *75*, 043002.

[82] Liu, D.; Wang, Y.-Y.; Sun, Y.-C.; Han, Y.-Y.; Cui, J.; Jiang, W. Self-assembly behavior of symmetrical linear ABCA tetrablock copolymer: A self-consistent field theory study. *Chin. J. Polym. Sci.* **2018**, *36*, 888–896.

[83] Takano, A.; Soga, K.; Suzuki, J.; Matsushita, Y. Noncentrosymmetric structure from a tetrablock quaterpolymer of the ABCA type. *Macromolecules* **2003**, *36*, 9288–9291.

[84] Polymeropoulos, G.; Zapsas, G.; Ntetsikas, K.; Bilalis, P.; Gnanou, Y.; Hadjichristidis, N. 50th Anniversary Perspective : Polymers with Complex Architectures. *Macromolecules* **2017**, *50*, 1253–1290.

[85] Gao, Y.; Deng, H.; Li, W.; Qiu, F.; Shi, A.-C. Formation of Nonclassical Ordered Phases of AB-Type Multiarm Block Copolymers. *Phys. Rev. Lett.* **2016**, *116*, 068304.

[86] Orfanou, K.; Iatrou, H.; Lohse, D. J.; Hadjichristidis, N. Synthesis of Well-Defined Second (G-2) and Third (G-3) Generation Dendritic Polybutadienes. *Macromolecules* **2006**, *39*, 4361–4365.

[87] Xu, Y.; Li, W.; Qiu, F.; Lin, Z. Self-assembly of 21-arm star-like diblock copolymer in bulk and under cylindrical confinement. *Nanoscale* **2014**, *6*, 6844.

[88] Zhao, M.; Li, W. Laves Phases Formed in the Binary Blend of AB 4 Miktoarm Star Copolymer and A-Homopolymer. *Macromolecules* **2019**, *52*, 1832–1842.

[89] Zhao, B.; Jiang, W.; Chen, L.; Li, W.; Qiu, F.; Shi, A.-C. Emergence and Stability of a Hybrid Lamella–Sphere Structure from Linear ABAB Tetrablock Copolymers. *ACS Macro Lett.* **2018**, *7*, 95–99.

[90] Chang, A. B.; Bates, C. M.; Lee, B.; Garland, C. M.; Jones, S. C.; Spencer, R. K. W.; Matsen, M. W.; Grubbs, R. H. Manipulating the ABCs of self-assembly via low-χ block polymer design. *Proc. Natl. Acad. Sci. USA* **2017**, *114*, 6462–6467.

[91] Lindsay, A. P.; Lewis III, R. M.; Lee, B.; Peterson, A. J.; Lodge, T. P.; Bates, F. S. A15, σ, and a Quasicrystal: Access to Complex Particle Packings via Bidisperse Diblock Copolymer Blends. *ACS Macro Lett.* **2020**, *9*, 197–203.

[92] Sherman, Z. M.; Howard, M. P.; Lindquist, B. A.; Jadrich, R. B.; Truskett, T. M. Inverse methods for design of soft materials. *J. Phys. Chem.* **2020**, *152*, 140902.

[93] Gadelrab, K. R.; Hannon, A. F.; Ross, C. A.; Alexander-Katz, A. Inverting the design path for self-assembled block copolymers. *Mol. Syst. Des. Eng.* **2017**, *2*, 539–548.

[94] Miskin, M. Z.; Khaira, G.; de Pablo, J. J.; Jaeger, H. M. Turning statistical physics models into materials design engines. *Proc. Natl. Acad. Sci. USA* **2016**, *113*, 34–39.

[95] Xu, D.; Liu, H.; Zhu, Y.-L.; Lu, Z.-Y. Three-dimensional inverse design of nanopatterns with block copolymers and homopolymers. *Nanoscale* **2016**, *8*, 5235–5244.

[96] Zhang, R.; Zhang, L.; Lin, J.; Lin, S. Customizing topographical templates for aperiodic nanostructures of block copolymers via inverse design. *Phys. Chem. Chem. Phys.* **2019**, *21*, 7781–7788.

[97] Hannon, A. F.; Gotrik, K. W.; Ross, C. A.; Alexander-Katz, A. Inverse Design of Topographical Templates for Directed Self-Assembly of Block Copolymers. *ACS Macro Lett.* **2013**, *2*, 251–255.

[98] Hannon, A. F.; Ding, Y.; Bai, W.; Ross, C. A.; Alexander-Katz, A. Optimizing Topographical Templates for Directed Self-Assembly of Block Copolymers via Inverse Design Simulations. *Nano Lett.* **2014**, *14*, 318–325.

[99] Qin, J.; Khaira, G. S.; Su, Y.; Garner, G. P.; Miskin, M.; Jaeger, H. M.; de Pablo, J. J. Evolutionary pattern design for copolymer directed self-assembly. *Soft Matter* **2013**, *9*, 11467.

[100] Khaira, G. S.; Qin, J.; Garner, G. P.; Xiong, S.; Wan, L.; Ruiz, R.; Jaeger, H. M.; Nealey, P. F.; de Pablo, J. J. Evolutionary Optimization of Directed Self-Assembly of Triblock Copolymers on Chemically Patterned Substrates. *ACS Macro Lett.* **2014**, *3*, 747–752.

[101] Jaeger, H. M.; de Pablo, J. J. Perspective: Evolutionary design of granular media and block copolymer patterns. *APL Mater.* **2016**, *4*, 053209.

[102] Kennedy, J.; Eberhart, R. Particle swarm optimization. Proceedings of ICNN'95 - International Conference on Neural Networks. 1995; pp 1942–1948.

[103] Eberhart, R.; James Kennedy, A New Optimizer Using Particle Swarm Theory. Proceedings of the Sixth International Symposium on Micro Machine and Human Science. Nagoya, Japan, 1995; pp 39–43.

[104] Wang, Y.; Lv, J.; Zhu, L.; Ma, Y. Crystal structure prediction via particle-swarm optimization. *Phys. Rev. B* **2010**, *82*, 094116.

[105] Fernández-Cabán, P. L.; Masters, F. J. Hybridizing particle swarm and big bang-big crunch optimization methods to explore then exploit the design domain of large planar frame structures. *Comput. Struct.* **2018**, *202*, 1–14.

[106] Li, L.; Huang, Z.; Liu, F.; Wu, Q. A heuristic particle swarm optimizer for optimization of pin connected structures. *Comput. Struct.* **2007**, *85*, 340–349.

[107] Pandey, S.; Wu, L.; Guru, S. M.; Buyya, R. A Particle Swarm Optimization-Based Heuristic for Scheduling Workflow Applications in Cloud Computing Environments. 2010 24th IEEE International Conference on Advanced Information Networking and Applications. 2010; pp 400–407.

[108] Pugh, J.; Martinoli, A. Inspiring and Modeling Multi-Robot Search with Particle Swarm Optimization. 2007 IEEE Swarm Intelligence Symposium. 2007; pp 332–339.

[109] Paradiso, S. P.; Delaney, K. T.; Fredrickson, G. H. Swarm Intelligence Platform for Multiblock Polymer Inverse Formulation Design. *ACS Macro Letters* **2016**, *5*, 972–976.

[110] Khadilkar, M. R.; Paradiso, S. P.; Delaney, K. T.; Fredrickson, G. H. Inverse Design of Bulk Morphologies in Multiblock Polymers Using Particle Swarm Optimization. *Macromolecules* **2017**, *50*, 6702–6709.

[111] `https://pscf.cems.umn.edu`.

[112] Bratton, D.; Kennedy, J. Defining a standard for particle swarm optimization. Proceedings of the 2007 IEEE Swarm Intelligence Symposium, SIS 2007. 2007; pp 120–127.

[113] Clerc, M.; Kennedy, J. The particle swarm - explosion, stability, and convergence in a multidimensional complex space. *IEEE Trans. Evol. Comput.* **2002**, *6*, 58–73.

[114] Tyler, C. A.; Qin, J.; Bates, F. S.; Morse, D. C. SCFT Study of Nonfrustrated ABC Triblock Copolymer Melts. *Macromolecules* **2007**, *40*, 4654–4668.

[115] Drolet, F.; Fredrickson, G. H. Combinatorial Screening of Complex Block Copolymer Assembly with Self-Consistent Field Theory. *Phys. Rev. Lett.* **1999**, *83*, 4317–4320.

[116] Bohbot-Raviv, Y.; Wang, Z.-G. Discovering New Ordered Phases of Block Copolymers. *Phys. Rev. Lett.* **2000**, *85*, 3428–3431.

[117] Guo, Z.; Zhang, G.; Qiu, F.; Zhang, H.; Yang, Y.; Shi, A.-C. Discovering Ordered Phases of Block Copolymers: New Results from a Generic Fourier-Space Approach. *Phys. Rev. Lett.* **2008**, *101*, 028301.

[118] Tsai, C. L.; Delaney, K. T.; Fredrickson, G. H. Genetic Algorithm for Discovery of Globally Stable Phases in Block Copolymers. *Macromolecules* **2016**, *49*, 6558–6567.

[119] Stasiak, P.; Matsen, M. W. Efficiency of pseudo-spectral algorithms with Anderson mixing for the SCFT of periodic block-copolymer phases. *Eur. Phys. J. E* **2011**, *34*, 110.

[120] Case, L. J.; Bates, F. S.; Dorfman, K. D. Tuning conformational asymmetry in particle-forming diblock copolymer alloys. *Soft Matter* **2023**, *19*, 90–97.

[121] Matsen, M. W. Effect of architecture on the phase behavior of AB-type block copolymer melts. *Macromolecules* **2012**, *45*, 2161–2165.

[122] Whitmore, M. D.; Vavasour, J. D. Self-consistent mean field theory of the microphase diagram of block copolymer/neutral solvent blends. *Macromolecules* **1992**, *25*, 2041–2045.

[123] Bates, F. S.; Fredrickson, G. H. Conformational Asymmetry and Polymer-Polymer Thermodynamics. *Macromolecules* **1994**, *27*, 1065–1067.

[124] Bates, F. S.; Schulz, M. F.; Khandpur, A. K.; Förster, S.; Rosedale, J. H.; Almdal, K.; Mortensen, K. Fluctuations, conformational asymmetry and block copolymer phase behaviour. *Faraday Discuss.* **1994**, *98*, 7–18.

[125] Xie, N.; Li, W.; Qiu, F.; Shi, A.-C. σ Phase Formed in Conformationally Asymmetric AB-Type Block Copolymers. *ACS Macro Lett.* **2014**, *3*, 906–910.

[126] Lindsay, A. P.; Mueller, A. J.; Mahanthappa, M. K.; Lodge, T. P.; Bates, F. S. Wigner-Seitz Cell generation and calculations in MATLAB. 2021; Retrieved from the Data Repository for the University of Minnesota.

[127] Olmsted, P. D.; Milner, S. T. Strong-segregation theory of bicontinuous phases in block copolymers. *Phys. Rev. Lett.* **1994**, *72*, 936–939.

[128] Reddy, A.; Buckley, M. B.; Arora, A.; Bates, F. S.; Dorfman, K. D.; Grason, G. M. Stable Frank–Kasper phases of self-assembled, soft matter spheres. *Proc. Natl. Acad. Sci. USA* **2018**, *115*, 10233–10238.

[129] Magruder, B. R.; Park, S. J.; Collanton, R. P.; Bates, F. S.; Dorfman, K. D. Laves Phase Field in a Diblock Copolymer Alloy. *Macromolecules* **2022**, *55*, 2991–2998.

[130] Stein, F.; Leineweber, A. Laves phases: a review of their functional and structural applications and an improved fundamental understanding of stability and properties. *J. Mater. Sci.* **2021**, *56*, 5321–5427.

[131] Nouri, B.; Chen, C.-Y.; Huang, Y.-S.; Mansel, B. W.; Chen, H.-L. Emergence of a Metastable Laves C14 Phase of Block Copolymer Micelle Bearing a Glassy Core. *Macromolecules* **2021**, *54*, 9195–9203.

[132] Lindsay, A. P.; Cheong, G. K.; Peterson, A. J.; Weigand, S.; Dorfman, K. D.; Lodge, T. P.; Bates, F. S. Complex Phase Behavior in Particle-Forming AB/AB′ Diblock Copolymer Blends with Variable Core Block Lengths. *Macromolecules* **2021**, *54*, 7088–7101.

[133] Magruder, B. R.; Dorfman, K. D. The C36 Laves phase in diblock polymer melts. *Soft Matter* **2021**, *17*, 8950–8959.

[134] Uddin, M. H.; Rodriguez, C.; López-Quintela, A.; Leisner, D.; Solans, C.; Esquena, J.; Kunieda, H. Phase Behavior and Microstructure of Poly(oxyethylene)-Poly(dimethylsiloxane) Copolymer Melt. *Macromolecules* **2003**, *36*, 1261–1271.

[135] Helfand, E. Theory of inhomogeneous polymers: Fundamentals of the Gaussian random-walk model. *J. Chem. Phys.* **1975**, *62*, 999–1005.

[136] Helfand, E. Block Copolymer Theory. III. Statistical Mechanics of the Microdomain Structure. *Macromolecules* **1975**, *8*, 552–556.

[137] Matsen, M. W. Stabilizing New Morphologies by Blending Homopolymer with Block Copolymer. *Phys. Rev. Lett.* **1995**, *74*, 4225–4228.

[138] Whitmore, M. D.; Noolandi, J. Theory of phase equilibria in block copolymer-homopolymer blends. *Macromolecules* **1985**, *18*, 2486–2497.

[139] Matsen, M. W.; Bates, F. S. Conformationally asymmetric block copolymers. *J. Polym. Sci. B: Polym. Phys.* **1997**, *35*, 945–952.

[140] Olmsted, P. D.; Milner, S. T. Strong Segregation Theory of Bicontinuous Phases in Block Copolymers. *Macromolecules* **1998**, *31*, 4011–4022.

[141] Collanton, R. P.; Dorfman, K. D. Interfacial geometry in particle-forming phases of diblock copolymers. *Phys. Rev. Mater.* **2022**, *6*, 015602.

[142] Li, W.; Liu, Y.-X. Simplicity in mean-field phase behavior of two-component miktoarm star copolymers. *J. Chem. Phys.* **2021**, *154*, 014903.

[143] Yamamoto, K.; Takagi, H. Frank-Kasper σ and A15 Phases Formed in Symmetry and Asymmetry Block Copolymer Blend System. *Mater. Trans.* **2020**, *62*, 325–328.

[144] Lindsay, A. P. Structure and Dynamics of Compositionally Asymmetric Block Polymers and Their Blends. Ph.D. thesis, University of Minnesota, 2021.

[145] Lewis III, R. M.; Arora, A.; Beech, H. K.; Lee, B.; Lindsay, A. P.; Lodge, T. P.; Dorfman, K. D.; Bates, F. S. Role of Chain Length in the Formation of Frank-Kasper Phases in Diblock Copolymers. *Phys. Rev. Lett.* **2018**, *121*, 208002.

[146] `https://docs.scipy.org/doc/scipy/reference/generated/scipy.interpolate.UnivariateSpline.html`, (accessed September 2022).

[147] `https://docs.scipy.org/doc/scipy/reference/generated/scipy.optimize.root.html`, (accessed September 2022).

[148] More, J. J.; Garbow, B. S.; Hillstrom, K. E. *User guide for MINPACK-1*; Report ANL-80-70, 1980.

Appendix A

Supporting Information for Chapter 5: Conformational asymmetry in sphere-forming AB/B′C diblock polymer alloys[†]

A.1 Phase Coexistence

For two or more phases to be in equilibrium, they must have equal pressure and temperature, and the chemical potential of each species in the system must be the same in all phases. In the SCFT calculations employed here, the temperature of the system is set by the Flory-Huggins parameter χ_{ij}; therefore, the equal temperature condition for equilibrium is met as long as calculations are done at fixed χ_{ij}, regardless of the ensemble in which calculations are performed. Establishing the equal-pressure and equal-chemical potential conditions differs by the ensemble selected. The remainder of this section describes the methods for equilibrium determination in the canonical and grand canonical ensembles.

[†]This appendix is adapted from the supporting information of Logan J. Case, Frank S. Bates, and Kevin D. Dorfman, *Soft Matter* **2023**, *19*(1), 115. (Ref. 120)

A.1.1 Canonical Ensemble: Common Tangent

The SCFT calculations performed here assume incompressibility of the polymers. Due to this assumption in the canonical ensemble, the addition of a constant pressure to the system will not change the Helmholtz free energy.[58] This means that the pressure in the canonical ensemble is arbitrary, and the requirement of constant pressure can always be met. The requirement of equal chemical potential in all phases for each species is established via the common tangent construction.[138]

To numerically determine a common tangent between phases I and II, the Helmholtz free energy data for each phase, collected at intervals of $\Delta\phi_{\mathrm{AB}} = 0.005$, is first fit to a cubic spline, giving the energy of each phase as a function of ϕ_{AB}, $F^{\mathrm{I}}(\phi_{\mathrm{AB}})$ and $F^{\mathrm{II}}(\phi_{\mathrm{AB}})$. To ensure fidelity to the underlying data, this spline was computed with a zero smoothing factor, which forces the curve to pass exactly through all data points.[146] The compositions of the two coexisting phases, $\phi^{\mathrm{I}}_{\mathrm{AB}}$ and $\phi^{\mathrm{II}}_{\mathrm{AB}}$, were then calculated numerically by seeking the root of

$$\mathbf{f}(\phi^{\mathrm{I}}_{\mathrm{AB}}, \phi^{\mathrm{II}}_{\mathrm{AB}}) = \begin{bmatrix} f_1(\phi^{\mathrm{I}}_{\mathrm{AB}}, \phi^{\mathrm{II}}_{\mathrm{AB}}) \\ f_2(\phi^{\mathrm{I}}_{\mathrm{AB}}, \phi^{\mathrm{II}}_{\mathrm{AB}}) \end{bmatrix} \tag{A.1}$$

where f_1 and f_2 are given by

$$f_1(\phi^{\mathrm{I}}_{\mathrm{AB}}, \phi^{\mathrm{II}}_{\mathrm{AB}}) = \frac{dF^{\mathrm{I}}}{d\phi_{\mathrm{AB}}}(\phi^{\mathrm{I}}_{\mathrm{AB}}) - \frac{F^{\mathrm{I}}(\phi^{\mathrm{I}}_{\mathrm{AB}}) - F^{\mathrm{II}}(\phi^{\mathrm{II}}_{\mathrm{AB}})}{\phi^{\mathrm{I}}_{\mathrm{AB}} - \phi^{\mathrm{II}}_{\mathrm{AB}}} \tag{A.2}$$

$$f_2(\phi^{\mathrm{I}}_{\mathrm{AB}}, \phi^{\mathrm{II}}_{\mathrm{AB}}) = \frac{dF^{\mathrm{II}}}{d\phi_{\mathrm{AB}}}(\phi^{\mathrm{I}}_{\mathrm{AB}}) - \frac{F^{\mathrm{I}}(\phi^{\mathrm{I}}_{\mathrm{AB}}) - F^{\mathrm{II}}(\phi^{\mathrm{II}}_{\mathrm{AB}})}{\phi^{\mathrm{I}}_{\mathrm{AB}} - \phi^{\mathrm{II}}_{\mathrm{AB}}} \tag{A.3}$$

The root of $\mathbf{f}(\phi^{\mathrm{I}}_{\mathrm{AB}}, \phi^{\mathrm{II}}_{\mathrm{AB}})$ occurs when the slope of the tangent to each energy curve, $dF^i/d\phi_{\mathrm{AB}}$, equals the slope of the line connecting the tangent points, $\left(\phi^{\mathrm{I}}_{\mathrm{AB}}, F^{\mathrm{I}}(\phi^{\mathrm{I}}_{\mathrm{AB}})\right)$ and $\left(\phi^{\mathrm{II}}_{\mathrm{AB}}, F^{\mathrm{II}}(\phi^{\mathrm{II}}_{\mathrm{AB}})\right)$, which guarantees that the points are co-linear along the common tangent. This construction is depicted in Fig. A.1.

Optimization was done with the SciPy root-finding method `scipy.optimize.root` using the `'hybr'` method option, which uses a modified Powell method as implemented in MINPACK.[147,148] In general, we find this method to be very robust for common

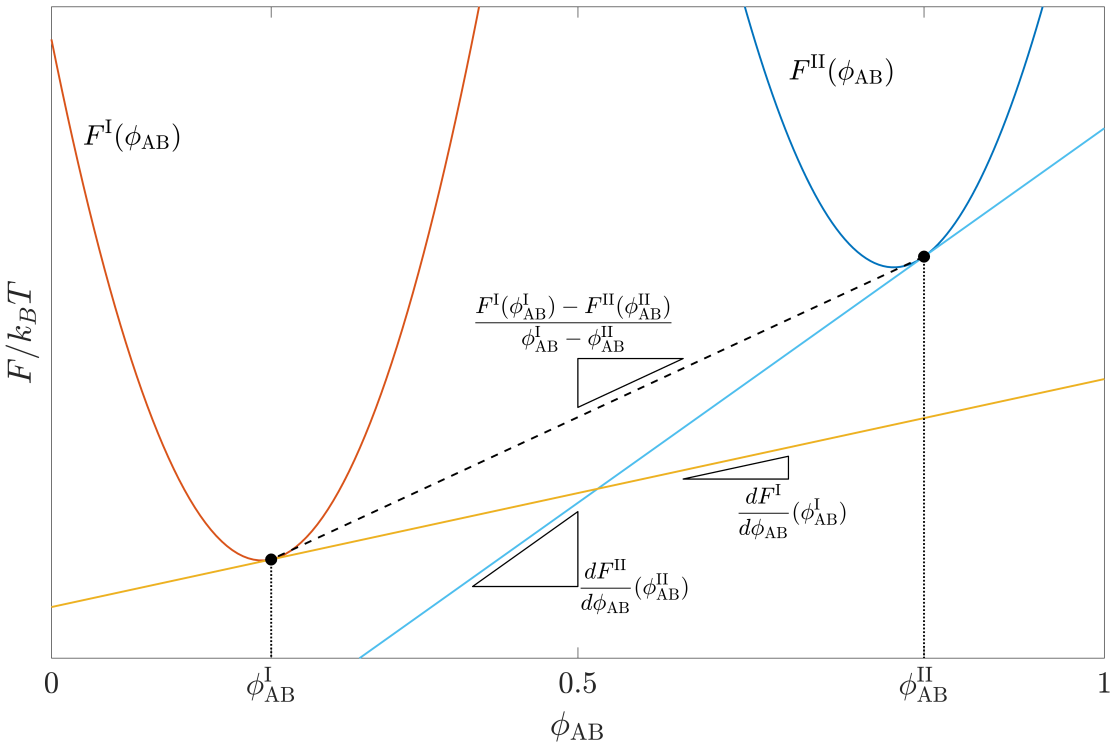

Figure A.1: Representative illustration of the common tangent calculation method for arbitrary phases I and II, using hypothetical quadratic Helmholtz free energy curves for these phases, $F^{\mathrm{I}}(\phi_{\mathrm{AB}})$ and $F^{\mathrm{II}}(\phi_{\mathrm{AB}})$ respectively. The method iterates to find the coexistence compositions, $\phi^{\mathrm{I}}_{\mathrm{AB}}$ and $\phi^{\mathrm{II}}_{\mathrm{AB}}$, at the root of Eq. A.1. The solid lines are the tangents to $F^{\mathrm{I}}(\phi_{\mathrm{AB}})$ and $F^{\mathrm{II}}(\phi_{\mathrm{AB}})$ at the points $\left(\phi^{\mathrm{I}}_{\mathrm{AB}}, F^{\mathrm{I}}(\phi^{\mathrm{I}}_{\mathrm{AB}})\right)$ and $\left(\phi^{\mathrm{II}}_{\mathrm{AB}}, F^{\mathrm{II}}(\phi^{\mathrm{II}}_{\mathrm{AB}})\right)$, respectively. These tangent points are marked with black dots. The dashed line connects the two tangent points. The slopes of the tangent lines and the connector line are indicated on the graph algebraically as they are listed in Eqs. A.2 and A.3. When all three slopes are equal, at the root of Eq. A.1, the tangent points $\left(\phi^{\mathrm{I}}_{\mathrm{AB}}, F^{\mathrm{I}}(\phi^{\mathrm{I}}_{\mathrm{AB}})\right)$ and $\left(\phi^{\mathrm{II}}_{\mathrm{AB}}, F^{\mathrm{II}}(\phi^{\mathrm{II}}_{\mathrm{AB}})\right)$ will be co-linear along the common tangent. Figure reproduced from Ref. 120.

tangent calculations, with most tangent calculations converging when the ϕ_{AB} midpoint of each energy curve is used as the initial guess for the respective ϕ^{i}_{AB}, which was the default initial guess for our calculations.

When this methodology was used to choose a macrophase separation pairing for comparison to the Laves phase, as done in Figs. 5.3 and 5.4, phases I and II represent the AB-rich and B′C-rich bcc or fcc phases. When used in construction of the phase diagram to determine phase boundaries along the Laves phase field, phases I and II would represent a Laves phase and one of the AB-rich or B′C-rich phases.

A.1.2 Grand Canonical Ensemble

Our approach to phase coexistence in the grand canonical ensemble follows the method described by Matsen[137] and that used by Magruder et al.[129] in their work on conformationally symmetric diblock alloys. Due to the incompressibility of the system, the chemical potentials of the AB and B′C chains are not independent, allowing us to choose $\mu_{\mathrm{AB}}/k_BT = 0$ for all calculations. This trivially satisfies the chemical potential criteria for the AB chain. The chemical potential value input to PSCF for the B′C chain, $\mu_{\mathrm{B'C}}/k_BT$, is then controlled as an independent variable and phases are compared across $\mu_{\mathrm{B'C}}/k_BT$ values (similarly to ϕ_{AB} in the canonical ensemble). By controlling the value of $\mu_{\mathrm{B'C}}/k_BT$, we thus also meet the chemical potential criterion for B′C. The pressure of each phase as calculated with Eqn. 2.13 is output by PSCF following convergence of the SCFT calculation. The final equilibrium criterion, equal pressure, is met when the Pv/k_BT vs $\mu_{\mathrm{B'C}}/k_BT$ curves of the phases intersect. In general, SCFT calculations were run at increments of 0.0005 in $\mu_{\mathrm{B'C}}/k_BT$. In some cases, however, larger sampling increments were required when large ranges of $\mu_{\mathrm{B'C}}/k_BT$ needed to be sampled to find an intercept. These larger sampling increments were most often needed while resolving the high-temperature regions near the ODT, where the $P(\mu_{\mathrm{B'C}})$ curves of disorder and the AB-rich or B′C-rich fcc phases were nearly parallel. In these cases, $\mu_{\mathrm{B'C}}/k_BT$ needed to be sampled over ranges up to two orders of magnitude larger than was typically required. Regardless of sampling increment, interpolation was used to determine the chemical potential and composition of the phases at equilibrium.

A.2 Candidate Phases

In order to generate the phase diagrams reported in the main text, we needed to consider a variety of competitor phases in addition to the Laves phases and macrophase separation candidates. Table A.1 lists the phases considered during construction of phase diagrams. The table contains crystallographic information, SCFT spatial discretization, and information on the number of particles and assignment of particles as AB or B′C micelles. As stated in the main text, the phases considered in this work are inspired by the work of Xie et al.[125] and match the candidate set employed by Magruder et al.[129]

Several of the candidate phases listed here (specifically ReO_3, TiO_2, CaF_2, and α-Al_2O_3) proved particularly difficult to converge in many regions of the phase diagram, as noted previously by Magruder et al.[129], and are therefore missing from many of the canonical ensemble calculation sets. Among these phases, ReO_3 proved the most problematic, as we were unable to achieve convergence of an initial field at the desired conformational asymmetry for either of the phase diagrams reported in this work (Figures 4 and 5 of the main text). In the case of $\epsilon_{BC} = 1.5$, we were unable to converge an initial field for α-Al_2O_3. Finally, we were unable to obtain initial fields for either TiO_2 or CaF_2 for $\epsilon_{AB} = \epsilon_{BC} = 1.5$. In all cases, if we were unable to obtain an initial field at the desired conformational asymmetry, we assume the phase is highly unfavorable at the conditions being considered, and omit it from the analysis.

Table A.1: Complete list of phases considered during generation of the phase diagrams. Table includes the name of the phase (Phase name); the label used to identify the phase in figures (Label Name); The space group of the phase; the spatial discretization used in SCFT calculations for the phase (SCFT grid size); the number of nominally spherical particles in a unit cell of the phase (Particles per unit cell); the ratio of the number of particles composed of AB chains to the number of particles composed of B′C chains (AB/B′C particle ratio).

Phase name	**Label name**	**Space group**	**SCFT grid size**	**Particles per unit cell**	**AB/B′C particle ratio**
$MgZn_2$	C14	$P6_3/mmc$	64x64x104	12	2:1
$MgCu_2$	C15	$Fd\bar{3}m$	96x96x96	24	2:1
W	bcc	$Im\bar{3}m$	48x48x48	2	0 or 1*
CsCl	alt-bcc	$Pm\bar{3}m$	64x64x64	2	1:1
Cu	fcc	$Fm\bar{3}m$	48x48x48	4	0 or 1*
Hexagonally packed cylinders	hex	p6mm	48x48	N/A	0 or 1*
Alternating hex	alt-hex	p6mm	48x48	N/A	2:1
Inverted alt-hex	$(\text{alt-hex})_i$	p6mm	48x48	N/A	1:2
Nb_3Sn	A15	$Pm\bar{3}n$	64x64x64	8	1:3
AlB_2	AlB_2	P6/mmm	64x64x64	3	2:1
sapphire (α-BN)	α-Al_2O_3	$R\bar{3}c$	64x64x64	10	3:2
α-BN	α-BN	$P6_3/mmc$	48x48x64	4	1:1
CaF_2	CaF_2	$Fm\bar{3}m$	64x64x64	12	2:1
Li_3Bi	Li_3Bi	$Fm\bar{3}m$	64x64x64	16	3:1
Inverted Li_3Bi	$(Li_3Bi)_i$	$Fm\bar{3}m$	64x64x64	16	3:1
rocksalt	NaCl	$Fm\bar{3}m$	64x64x64	8	1:1
ReO_3	ReO_3	$Pm\bar{3}m$	64x64x64	4	3:1
σ-FeCr	σ	$P4_2/mnm$	128x128x64	30	1:2†
TiO_2	TiO_2	$P4_2/mnm$	64x64x42	6	1:2
ZnS	ZnS	$F\bar{4}3m$	64x64x64	8	1:1

*These structures represent the AB-rich and B′C-rich morphologies considered for macrophase separation. All particles are composed of the majority species, with the minority located in interstitial sites.

†Particle assignment for σ is not trivial given the complexity of the structure. Here, B′C is placed in particles with volume above the number-averaged particle volume for the phase (Wyckoff positions 4f, 8i′, and 8j) while AB is placed in particles with volumes below this average (Wyckoff Positions 2b, and 8i), according to the volumes computed by Reddy et al. using the diblock foam model.[128] This "above average" vs "below average" criteria was chosen for consistency with the Laves phases, in which B′C was assigned to the larger particles.

A.3 Phase Diagram

Construction of the phase diagram reported in Fig. 5.6 for an alloy with $N_{\mathrm{B'C}}/N_{\mathrm{AB}} = 1.0$ and $\epsilon_{\mathrm{BC}} = 1.5$ started with initial sets of canonical ensemble SCFT calculations followed by common tangent constructions at $\chi N = 23.5$ (the lowest value at which the Laves phases converged) and integer values of χN from 24.0 to 40.0 to obtain a coarse map of the phase boundaries. Subsequent canonical ensemble, common-tangent calculations were then performed at increments of 0.5 in χN around the AB-rich and B′C-rich coexistence transitions points (such as where the AB-rich phase in coexistence with the Laves phase field changes from fcc to bcc, or from bcc to hex). These first two rounds of calculation considered only the Laves phases and the macrophase separation competitors. A third round of canonical ensemble calculations added the remaining competitors at a selection of segregation strengths. Below the transition to Laves-$\mathrm{hex_{AB}}$ coexistence, competing phases were run at all sampled segregation strengths. Above this transition, we noticed that the AB-rich hex phase quickly out-competes the Laves phases and suspected that it would similarly outcompete the other sphere-forming morphologies. We chose to run the remaining competitors only at $\chi N = 30$, $\chi N = 40$, and at odd values of χN from 31 to 39 finding that, indeed, all competitors are similarly outcompeted by AB-rich hex with increasing χN. On the basis of this result, we chose not to run the competing phases at the remaining χN values. Finally, grand canonical ensemble calculations were used to refine the position of invariant points and map the region near the ODT.

Here, Fig. A.2 reports the same phase diagram as Fig. 5.6, but includes the particular points used to generate the diagram. Each dot in Fig. A.2 represents a point at which we have collected SCFT data. Data were collected at the highest density near invariant points where grand canonical ensemble was used to resolve the three-phase coexistence conditions. The reported data show that the splines used to draw the phase boundaries introduce no anomalous shapes and broadly reflect the collected data.

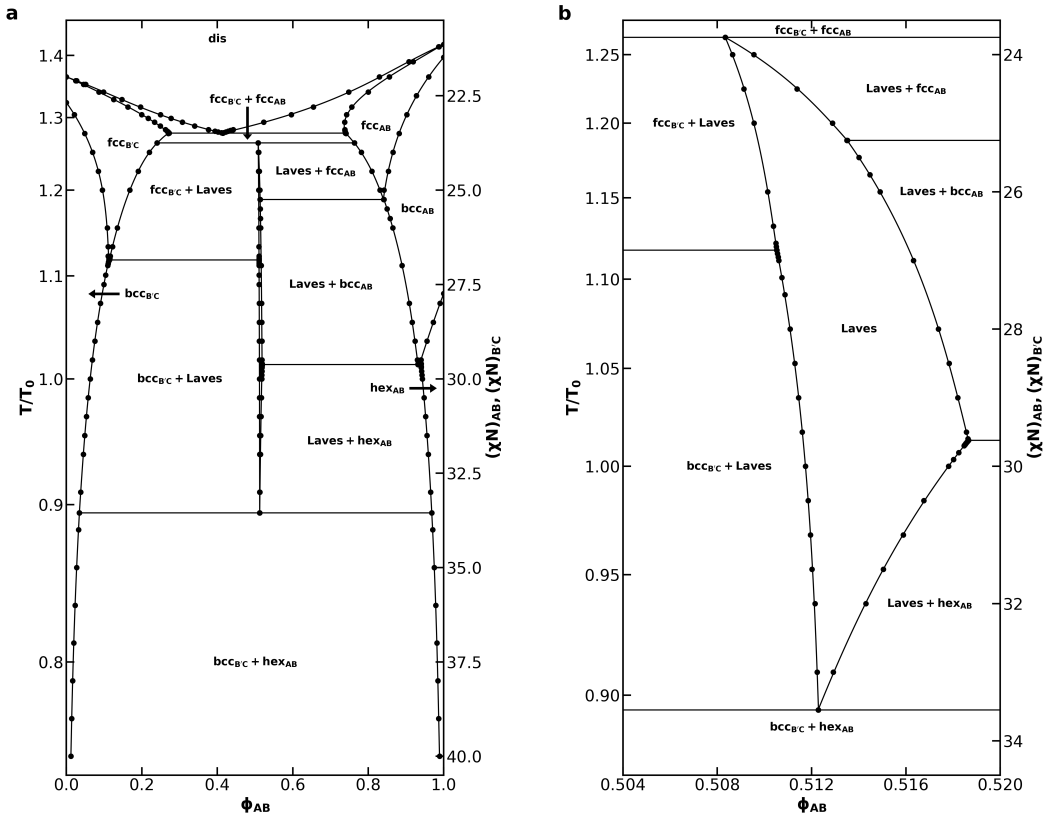

Figure A.2: (a) Phase diagram for an AB/B′C alloy with $N_{\mathrm{B'C}}/N_{\mathrm{AB}} = 1.0$, $f_{\mathrm{A}} = f_{\mathrm{C}} = 0.20$, $\epsilon_{\mathrm{AB}} = 1.0$, $\epsilon_{\mathrm{BC}} = 1.5$, and assuming purely enthalpic χ values such that $\chi_{\mathrm{AC}} N_{\mathrm{AB}} = 2\,(\chi N)$ at all T and (b) a detailed view of the Laves phase field within that phase diagram. Points indicate conditions at which we collected SCFT data. The reference temperature, T_0, was chosen to correspond to $\chi N = 30$. Non-linear segments of the phase diagram are drawn using cubic splines fit to the sampled data. Figure reproduced from Ref. 120.